

**MODELLING THERMO-HYDRO-MECHANICAL
THM INTERACTIONS AFFECTING EVOLUTION
OF INJECTION-INDUCED SEISMICITY
IN FRACTURED GEOTHERMAL RESERVOIRS**



**POLITECNICO
DI TORINO**

Kareem Ramzy Aboayanah
MSc Thesis - 2019



**Department of Environment, Land and Infrastructure Engineering
(DIATI)
Petroleum Engineering Master of Science Program
Politecnico di Torino**

***MODELLING THERMO-HYDRO-MECHANICAL THM INTERACTIONS
AFFECTING EVOLUTION OF INJECTION-INDUCED SEISMICITY IN
FRACTURED GEOTHERMAL RESERVOIRS***

Student:

Kareem Ramzy Aboayanah (S239590)

Supervisors:

Prof. Claudio Oggeri – Principal Supervisor - Politecnico di Torino

Prof. Luigi Sambuelli – Co-Supervisor - Politecnico di Torino

Prof. Luca Martinelli – Co-Supervisor - Politecnico di Milano

*Submitted in partial fulfillment of the Master of Science degree from Politecnico di Torino
and the double degree from Politecnico of Milano - 2019*

Intentionally Blank

Acknowledgement

I would like to express my sincere thanks to Professor Claudio Oggeri for accepting to supervise this thesis of my own choice, and his encouragement and valuable guidance at every stage in developing this thesis. I have learnt a lot from him during applied geomechanics course and during my thesis work. Also, I would like to sincerely thank Professor Luigi Sambuelli and Professor Luca Martinelli for their time dedicated for reviewing my work and for their valuable comments that helped in improving it.

My thanks also go to the Alta Scuola Politecnica ASP for funding my master studies at Politecnico di Torino and for the enriching experience I acquired during the ASP program.

Last but not least, I would like to express my gratefulness and thankfulness to my parents for their support and encouragement during these extensive 2 years at Politecnico di Torino.

Yours Sincerely

Kareem

Dedication

I'm honored to dedicate this work to my parents, my siblings: Ahmed, Weaam, Amr & Ayah, and to my little nephew Adam.

Abstract

Injection-induced seismicity has been one of the major obstacles in front of developing geothermal resources and a source of disturbance in populated locations. Many efforts have been made to understand underground processes leading to induced seismicity in order to control and mitigate it during thermal energy extraction. My thesis aims to investigate different factors, related to both the operating and geologic conditions, leading to the occurrence of seismic events, and to derive optimum operating procedures to mitigate induced seismicity based on the proposed conceptual model.

During my thesis work, I developed two conceptual models using the finite volume code Itasca FLAC3D to model thermo-hydro-mechanical processes in the reservoir. The models are verified by solving pressure transient and displacement equations analytically using the built-in FISH programming language and comparing solutions with numerical results. Heat transfer by both convection and conduction are considered, and anisotropic state of stress and uniaxial strain conditions are applied as the initial and boundary conditions. First model is of a fault-free fractured reservoir to study the evolution of seismic events or what is called "triggering front". I used FISH language to introduce a set of fracture planes with different random orientation distributions, and used Mohr-Coulomb criterion to evaluate stability at each time step, where slip along a single fracture is taken as a potential microseismic event. Simulated time ranges from tens of hours to model pressure transient and poroelastic stresses changes around the injection well, up to months to model thermoelastic effects and temperature depletion.

Results show that thermal stresses might contribute to seismic events in the long-term operation (months to years) because of the low thermal diffusivity and low permeability of reservoir rocks. Furthermore, elastic moduli play a critical role in determining the poroelastic behavior of rock and fractures as they control the poroelastic stress path; for example, simulations reveal that specific ranges of Poisson's ratio could stabilize fractures during injection, while initiate slip during production. This reflects the importance of precise rock characterization in modeling specific reservoirs. Furthermore, I found that there is a relation between seismicity triggering front and the hydraulic diffusivity of the reservoir, and the lag between the pressure transient front and the triggering front is affected by the onset of seismicity. Mitigating induced seismicity can be achieved by establishing constraints on the down-hole injection pressure given that a robust model of underground faults and joints for a specific reservoir is available. Cyclic, step rate, and continuous injection scenarios are considered; cyclic and step rate injection were not noticed to reduce seismicity rate compared with continuous injection for the same injected volume for pre-existing fractures. Furthermore, slip events are noticed after shut-in during cyclic injection simulations, in agreement with field observations.

The second model is a 3D normal fault model. I built a coupled fluid-flow and geomechanical model to evaluate the behavior of a nearby fault in response to stress state perturbations due to cold water injection. Friction coefficient is allowed to evolve according to rate and state dependent friction laws. Different scenarios of frictional behavior including velocity-neutral, velocity-weakening and velocity-strengthening behavior, are investigated. Also, parametric analyses are performed on the injection operation parameters and the associated poroelastic and thermoelastic effects.

Under the considered state of stress, the largest slip and slip-rate magnitude always accompany the first rupture zone on the fault plane, and velocity-weakening behavior is found to produce larger rupture areas and results in larger magnitude seismic events. Moreover, slip rate is found to increase with increasing injection rate.

Intentionally Blank

Contents

| | |
|--|-----------|
| Acknowledgement..... | iv |
| Dedication | v |
| Abstract | vi |
| List of Figures..... | 10 |
| List of Tables..... | 13 |
| CHAPTER 1: Literature Review | 15 |
| 1.1-Introduction | 15 |
| 1.2 Brief of Induced Seismic Events..... | 16 |
| 1.2.1 Seismic Events Caused by Wastewater Disposal..... | 16 |
| 1.2.2 Seismic Events Caused by Hydraulic Fracturing..... | 18 |
| 1.2.3 Seismic Events During Heat Extraction from Geothermal Reservoirs | 18 |
| 1.2.4 Geological Features Affecting Triggering Seismicity..... | 19 |
| 1.2.5 Which Activity Has Higher Potential of Inducing Seismicity? | 20 |
| 1.3. Mechanism of Induced Seismicity | 21 |
| 1.3.1 Subsurface Stress Field | 22 |
| 1.3.2 Fractures and Faults Structure..... | 23 |
| 1.3.3 Rock Failure Physics..... | 24 |
| 1.3.4 Fluid-driven Stress Perturbation | 25 |
| 1.4 Forecasting Induced Seismicity..... | 27 |
| 1.4.1 Statistical Forecasting Approach | 28 |
| 1.4.2 Physics-Based Models | 29 |
| 1.4.3 Hybrid Models..... | 30 |
| CHAPTER 2: Geothermal Energy: Overview | 31 |
| 2.1 Introduction | 31 |
| 2.2 Applications of Geothermal Energy | 31 |
| 2.2.1 Direct Heating | 32 |
| 2.2.2 Ground Source Heating | 32 |
| 2.3 Overview of the global Market: (GEA 2016) | 32 |
| 2.4 Current Technology | 34 |
| 2.5 EGS Systems..... | 36 |
| CHAPTER 3: Thermoelasticity | 38 |
| 3.1 Introduction | 38 |
| 3.2 Thermoelasticity and Fracture Attributes | 39 |
| 3.2 Thermoelasticity at Reservoir Scale:..... | 40 |

| | |
|--|----|
| CHAPTER 4: Model Set-up | 43 |
| 4.1 Description | 43 |
| 4.2 Model Equations | 45 |
| 4.2.1 Transient Fluid Flow | 45 |
| 4.2.2 Permeability evolution: | 46 |
| 4.2.2 Constitutive Mechanical Model | 47 |
| 4.2.3 Thermal Model | 48 |
| 4.2.4 Thermal-Hydraulic-Mechanical Coupling | 48 |
| 4.3 Model Initialization and Verification | 48 |
| 4.3.1 Initialization | 48 |
| 4.3.2 Verification of Model | 49 |
| CHAPTER 5: Results | 53 |
| 5.1 Introduction | 53 |
| 5.2 Fractures Orientation: | 54 |
| 5.3 Thermal Stresses | 56 |
| 5.4 Permeability Evolution | 59 |
| 5.5 Elastic Moduli | 60 |
| 5.6 Effect of Injection Rate, Cyclic & Continuous Injection | 62 |
| 5.6 Role of Intermediate Stress | 68 |
| 5.7 Differential Stress | 69 |
| CHAPTER 6: Fault Frictional Behavior | 70 |
| 6.1 Introduction | 70 |
| 6.2 Model Description: | 71 |
| 6.3 Results | 73 |
| 6.3.1 Flow Rate | 74 |
| 6.3.2 Velocity-neutral simulations | 76 |
| 6.3.3 Velocity-strengthening simulations | 77 |
| 6.3.4 Velocity-weakening simulations | 77 |
| 6.3.5 Characteristic Slip Distance | 81 |
| CHAPTER 7: Conclusions and Discussion | 83 |
| References | 86 |

List of Figures

- Figure-1.1:** Locations of induced seismic events. Events displayed for the United States and Canada happened between January 2008 and June 2017. Events displayed for Europe happened between January 2006 and June 2017 (Keranen & Weingarten 2018). 17
- Figure-1.2:** Number of $M \geq 3$ events (gray bars) in the central United States from January 2000 to November 2017, along with summed seismic moment release during each year (white dots) (Keranen & Weingarten 2018). 17
- Figure-1.3:** Injected volume vs. induced moment for events: north-east British Columbia NE BC, Horn River Basin HRB for both stage averaged fracking and total pad and for geothermal reservoirs such as (Basel, Soultz, Cooper Basin) and other reported hydraulic fracture events. (Courtesy of Maxwell 2013) 21
- Figure-1.4:** Schematic illustration of pore pressure perturbations and poroelastic changes effects on fault stability. (a) Increasing pore pressure reduces normal effective stress, shifting the fault closer to the Mohr-Coulomb failure envelope, (b) Increasing poroelastic stress increases differential stress (Keranen & Weingarten 2018). 22
- Figure-1.5:** Earthquake Scaling (Courtesy of M. Zoback) 23
- Figure-1.6:** Effect of fracture density and distribution on pressure diffusion (Courtesy of Izadi 2012). 24
- Figure-1.7:** Maximum seismic moment as a function of injected volume, dots represent different cases from different activities; HF Hydraulic Fracturing, EGS Enhanced Geothermal Systems, WD Water Disposal, solid line represents upper moment magnitudes (data from McGarr 2013). 26
- Figure-1.8:** Schematic illustration of Advanced Traffic Light ATL system (Bruhn et al. 2015) 29
- Figure-2.1:** 2015 Geothermal power generation capacity (GEA 2016) 32
- Figure-2.2:** Geothermal Potential and the planned future installation (GEA 2016). 33
- Figure-2.3:** Planned additional geothermal power generation capacity installment (GEA 2016) 33
- Figure-2.4:** Schematic illustration of dry steam power plant (Courtesy of Encyclopedia Britannica 2012) 34
- Figure-2.5:** Schematic illustration of flash steam power plant (Courtesy of Encyclopedia Britannica 2012) 35
- Figure-2.6:** Schematic illustration of a binary geothermal power plant (Courtesy of Ormat Technologies). 35
- Figure-2.7:** Shares of the different geothermal power plants technologies. 36
- Figure-3.1:** Thermal stress profile after one month of injection. Fracture permeability $k_{fr} = 10-10m^2$: (a): higher matrix permeability $k_m = (10)^{-16} m^2$; (b): lower matrix permeability $k_m = (10)^{-18} m^2$ (Jansen & Miller 2017). 40
- Figure-4.1:** Model of a unit thickness reservoir layer. 43
- Figure-4.2:** Figure-4. 2: Dip and dip directions for a set of favorably oriented fractures introduced into the model representing a worst case scenario (set A in section 5.2). 44

- Figure-4.3:** Coupling scheme used in HM calculations (top), and THM calculations (bottom). 45
- Figure-4.4:** Gutenberg-Richter law for different b-values. 47
- Figure-4.5:** Pressure profile in the reservoir. Data shows exact match between analytic solution and numerical results (Parameters in table-3.1 are used in this simulation with injection rate of 0.16 l/m/s). 50
- Figure-4.6:** Analytical and numerical results of the vertical displacement (Parameters in table-3.1 are used in this simulation with injection rate of 0.16 l/m/s). 51
- Figure-4.7:** 45° joint reactivation conditions from MohrPlotter (software by Allmendinger 2014). 52
- Figure-5. 1:** Different initial orientations of fractures (left), and their stress status after 60 hours of injection with injection rate 0.04 l/m/ (right). 55
- Figure-5.2:** Temperature distribution in the reservoir after (a) one month, (b) two months, and (c) three months 56
- Figure-5.3:** (a),(c), & (e): isothermal (HM) evolution of the fractures status after 1,2 & 3 months, respectively, (b),(d), & (f): non-isothermal (THM) evolution of the fractures status after 1,2 & 3 months, respectively 57
- Figure-5. 4:** Pressure vs. time at three different locations in the reservoir. 58
- Figure-5.5:** Tensile change of fracture aperture after (a) 10 hour, (b) 20 hours, (c) 30 hours & (d) 40 hours 59
- Figure-5.6:** Shear stimulation of fracture aperture after (a) 10 hour, (b) 20 hours, (c) 30 hours & (d) 40 hours 59
- Figure-5.7:** Permeability evolution after (a) 10 hour, (b) 20 hours, (c) 30 hours & (d) 40 hours. 60
- Figure-5.8:** Poroelastic stress path for different Poisson's ratio ν after 40 hours of injection with injection rate of 0.025 l/s/m: (a) $\nu=0.49$ (b) $\nu=0.38$ (c) $\nu=0.25$ & (d) $\nu=0.115$ (Equation-5.4 used to calculate ν in terms of K & G) 61
- Figure-5.9:** Poroelastic stress path for $\nu=0.115$ after 40 hours of production with production rate of 0.025 l/m/s. 61
- Figure-5.10:** Effect of stress path coefficient on the behavior of faults and fracture during fluid production/injection. 62
- Figure-5 11:** Effect of injection rate on the induced seismic cloud: (a) 0.01 l/s/m, (b) 0.015 l/s/m, (c) 0.02 l/s/m, & (d) 0.03 l/m/s 63
- Figure-5.12:** Continuous injection with 0.02 l/m/s.: (Top) Seismic events evolution, (Bottom) Injection rate and pressure. 64
- Figure-5.13:** Cyclic injection with 0.04 l/m/s; (Top) Seismic events evolution, (Bottom) Injection rate and pressure. 65
- Figure-5.14:** Step rate scenario: (Top) Seismic events evolution, (Bottom) Injection rate and pressure. 66
- Figure-5.15:** Continuous rate equivalent to the simulated step-rate scenario (0.018 l/s/m): (Top) Seismic events evolution, (Bottom) Injection rate and pressure. 67
- Figure-5.16:** Evolution of slip and seismic events during 60 MPa injection pressure-higher than the seismicity onset (top), and 46 MPa injection pressure-lower than seismicity onset (bottom). 68

- Figure-5.17:** Seismic events evolution when (a) $\sigma_y = \sigma_x$ (b) $\sigma_y = \sigma_z$ (injection rate is 0.03 l/m/s) 69
- Figure-5.18:** Effect of differential stress on fractures status after 40 hours of continuous injection: (A) 30 MPa differential stress (B) 38 MPa differential stress. (Constant injection rate of 0.03 l/m/s is used in producing these results). 69
- Figure-6.1:** Fault model used in the simulations. 71
- Figure-6.2:** Interface structure in FLAC3D (Itasca FLAC3D Documentations). 72
- Figure-6.3:** (Top) Pore pressure at the injection point (bottom) pore pressure at the top of the fault. 75
- Figure-6.4:** Pore pressure contours at the end of the run with injection rate of 0.06 l/m/s (Other parameters found in Table-6.1) 76
- Figure-6.5:** Illustration of how the friction coefficient evolves with slip in a slip-weakening relation. 76
- Figure-6.6:** Friction coefficient vs. time at two points along the fault (top and middle) for different (a-b) values (a) $a-b=0$, (b) $a-b=+0.005$, (c) $a-b=+0.01$, (d) $a-b=-0.005$, & (e) $a-b=-0.01$. 78
- Figure-6.7:** Slip magnitude vs. time at two points along the fault (top and middle) for different (a-b) values (a) $a-b=0$, (b) $a-b=+0.005$, (c) $a-b=+0.01$, (d) $a-b=-0.005$, & (e) $a-b=-0.01$. 79
- Figure-6.8:** Slip rate vs. time at two points along the fault (top and middle) for different (a-b) values (a) $a-b=0$, (b) $a-b=+0.005$, (c) $a-b=+0.01$, (d) $a-b=-0.005$, & (e) $a-b=-0.01$. 80
- Figure-6.9:** Shear stress vs. time at two points along the fault (top and middle) for different (a-b) values (a) $a-b=0$, (b) $a-b=+0.005$, (c) $a-b=+0.01$, (d) $a-b=-0.005$, & (e) $a-b=-0.01$. 81
- Figure-6.10:** Shear slip magnitudes vs different values of L_c (Each dot represents a simulation run). 82
- Figure-6.11:** Slip rate magnitudes vs different values of L_c (Each dot represents a simulation run). 82

List of Tables

Table-4.1: Parameters used in the simulation study 49

Table-5.1: Parameters used in simulation runs in Figure-5.2 & 5.3. 54

Table-6.1: Parameters used in simulations. 72

Table-6.2: Simulation results for different injection rates using slip-weakening scenario for frictional strength. 74

Table-6.3: Results for different (a-b) values for different fictional evolution scenarios. 77

Table-6.4: Sensitivity analysis of different characteristic slip distances L_c 81

Intentionally Blank

CHAPTER 1: Literature Review

1.1-Introduction

Earthquake is an elastic strain energy release process accompanying a fault slip. Induced seismicity, also known as anthropogenic seismicity, is an earthquake caused by underground stress field perturbation resulting from human activities such as mining, fluid injection and/or production. McGarr et al. (2002) divides anthropogenic seismicity into induced and triggered. They suggest that "induced" should be used for stress perturbation of similar magnitude of the in-situ stress field, while "triggered" should be used for a fractional stress perturbation that causes a fault to slip. Freed (2005) suggests additional definition to the triggered seismicity; seismic events caused by older events are triggered by the previous ones. To avoid confusion, the term "induced" will be used in this thesis to indicate all anthropogenic seismicity.

Concern about induced seismicity dates back to 1894 earthquakes in Johannesburg, where Witwatersrand gold mining started in 1886 and was discovered to cause these events (McGarr 2002). Also, seismic events due to mining operations were observed in Europe approximately in the same era. In 1908 in Germany, the first seismicity recording station was installed in Bochum in the Ruhr coal basin, and the first seismicity recording network was established in the Upper Silesia coal basin, Poland, in the late 1920s.

Since then, several activities have been recognized or, at least hypothesized to cause anthropogenic seismicity. First observed seismic events accompanying oil production were in 1920s, while for reservoir impoundment were in 1930s. Injection induced seismicity was first observed in 1960s when Denver series of earthquakes occurred. These earthquakes occurred after waste water injected into a disposal well in Rocky Mountain, Denver, Colorado.

In few cases, induced seismicity can result in losses, such as the abandonment of \$ 60 million Basel geothermal project in Switzerland after a series of seismic events in 2006 (Gaucher et al. 2015), and the structural damages caused by Denver, Colorado, M* 5.3 earthquake in 1967 which triggered by wastewater disposal (Davies et al. 2013).

It has been noticed that injection-related activities result in seismic events lower than that resulted from other activities like mining or depleting hydrocarbon reservoir. Davies et al. (2013) listed and reviewed a group of seismic events with magnitude $M \geq 1$ that were caused by human activities since 1929. For example, mining operations have resulted in M 1.6-5.6 events; water injection for maintaining pressure of hydrocarbon reservoirs: M 1.9-5.1, wastewater disposal: M 2.0-5.3, geothermal operations: M 1.0-4.6, and hydraulic fracturing of hydrocarbon reservoirs: M 1.0-3.8. Details on individual events can be found in Davies et al. 2013.

*M denotes magnitude which is a number that characterizes the relative size of an earthquake. Magnitude is based on measurement of the maximum motion recorded by a seismograph (USGS Earthquake glossary).

Fluid injection activities recognized to induce seismicity include waste water disposal, hydrocarbon reservoir pressure maintenance by water injection, hydraulic fracturing of oil and gas reservoirs, geothermal reservoirs exploitation, and underground gas storage.

Hydraulic fracturing is the process of increasing rock surface connected directly to the wellbore. It is done by injecting chemically treated fluids under high pressure to overcome the rock strength and initiate fractures. Hydraulic fracturing may include multiple stages from a horizontal well (e.g. in shale gas). Proppant is injected with the fluid to keep the fractures open once the injection is stopped. Although hydraulic fracturing has been applied since 1940s, the commercial exploitation of this technology with horizontal wells and multi-stage fracking started in 1990s.

Thermal energy of the earth is exploited by circulating cool water into a high-temperature geothermal reservoir to be used in electrical generation and heating purposes. Current technology targets reservoirs with temperatures up to 300 °C. In magmatic regions, deeper reservoirs are characterized by temperature between 400-700°C, which would increase the share of geothermal energy in current world energy consumption. In some geothermal reservoirs the permeability of the rock is too low for a commercial heat extraction, therefore, hydraulic stimulation job is carried out to increase rock permeability (similar to hydraulic fracturing in oil and gas reservoirs). In this case it is called Enhanced Geothermal System EGS. Induced seismicity due to water injection remains the main obstacle in front of wide use of this huge energy source.

1.2 Brief of Induced Seismic Events

Statistically, the vast majority of injection operations around the world do not lead to seismicity felt by population in location. In USA, for example, there are around 35,000 active disposal wells, 80,000 active pressure maintenance wells for hydrocarbon reservoirs, and tens of thousands of hydraulic fracturing jobs are done every year, only few tens of these wells have been recognized to cause felt seismicity (Rubinstein & Mahani 2015). In fact, in order to induce a large, felt seismic event, there must be a combination of geological and operating settings in terms of the fault size and orientation, in-situ stress field, communication between wells and the fault, and pore pressure change.

1.2.1 Seismic Events Caused by Wastewater Disposal

One of the major and early seismic events that raised the awareness of the fluid injection as a trigger of seismicity was the above mentioned Colorado seismic events caused by waste water disposal well at Rocky Mountain Arsenal, Denver, Colorado (Davies et al 2013, Healy et al. 1968), and it was the largest event prior to the recent rise in seismicity in the last 10 years. Additionally, Ashtabula seismic events in Ohio, which started in 1987 and caused by wastewater disposal wells (Seeber et al. 2004).

A dramatic increase in injection-induced seismicity rate to has been observed during the last decade, including large number of felt and moderate magnitude seismic events (**Figure-1.1 & 1.2**). Wastewater injection rates and seismic events intensity have increased since 2008 in Texas, Arkansas, and Oklahoma (e.g., Ellsworth 2013). Ten felt earthquakes in late 2008 close to Dallas-Fort Worth airport in Texas due to wastewater disposal, although, there is ongoing debate on the reason behind these events (Janska & Eisner 2012).

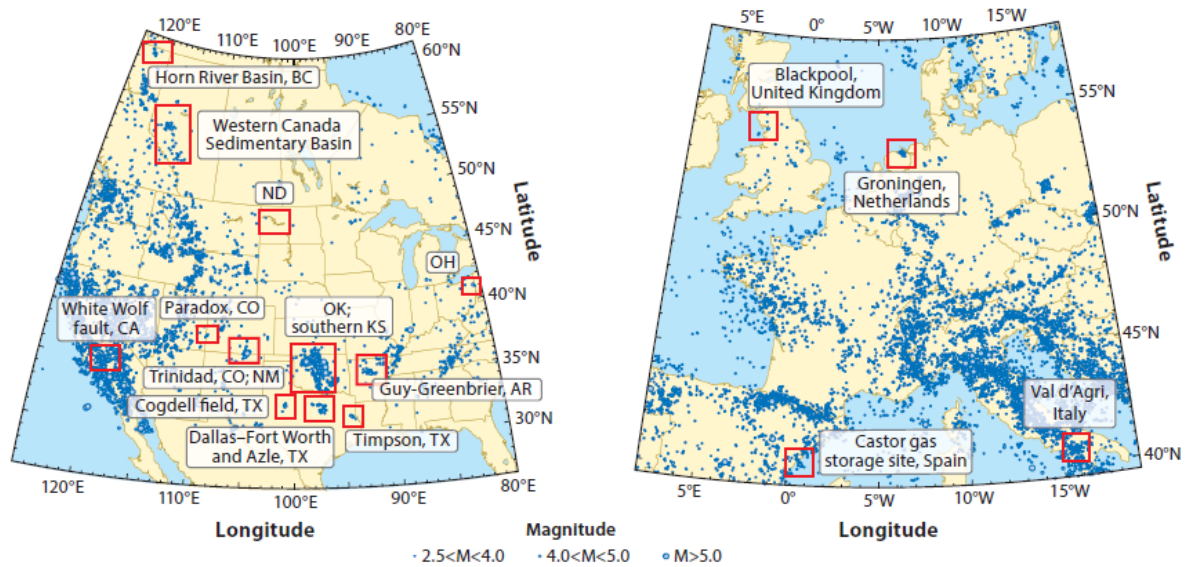


Figure-1.1: Locations of induced seismic events. Events displayed for the United States and Canada happened between January 2008 and June 2017. Events displayed for Europe happened between January 2006 and June 2017 (Keranen & Weingarten 2018).

During the period from 2009 to 2011, numerous events, with maximum of M 4.7, were observed near Guy-Greenbrier, Arkansas, and, during the same period, more than 200 events with $M \leq 3.9$ were recorded close to Oklahoma City (Keranen et al. 2014).

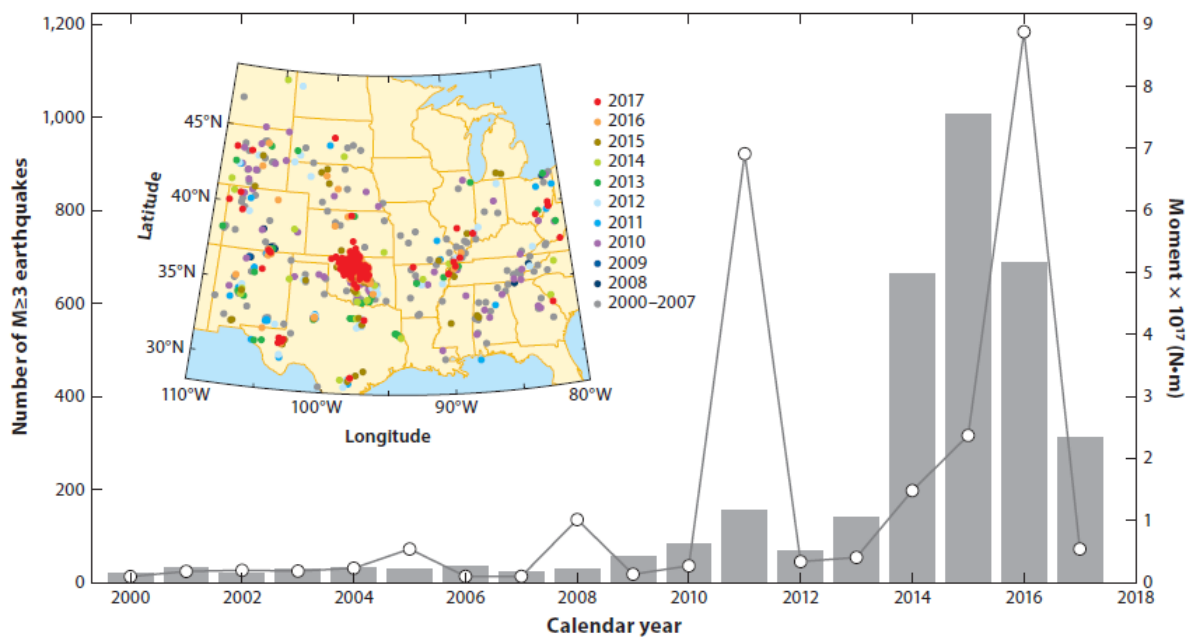


Figure-1.2: Number of $M \geq 3$ events (gray bars) in the central United States from January 2000 to November 2017, along with summed seismic moment release during each year (white dots) (Keranen & Weingarten 2018).

Earlier in Italy, a series of $M < 2.2$ events started in 2006 after disposing wastewater in the Val d'Agri field (Valoroso et al. 2009). One of the major shale plays in the United States—the Marcellus Shale of the Appalachian Basin in Pennsylvania, West Virginia, Ohio, and New York—lies within a region of low levels of natural seismicity. The regional seismographic network operated by Lamont Doherty Earth Observatory (LDEO) records all earthquakes with $M \geq 2$ in the region. Although thousands of hydraulic fracturing operations were conducted in Pennsylvania since the development of the field began in 2005, only six earthquakes with $M \geq$

2 were recorded by the LDEO network within the extent of the Marcellus Shale, the largest of which was just M 4.0, which recorded across the Ohio border in Youngstown, where it was caused by injection, much of the fluid apparently coming from wells in Pennsylvania (Kim 2013).

Several of these induced earthquakes surpassed M 5.0. In August 2011, a seismic event with M 5.3 hit the region of Trinidad, Colorado, followed by another earthquake with M 5.7 and two M 5.0 earthquakes due to wastewater injection in depleted oil reservoir near Prague, Oklahoma in November 2011 (Keranen et al. 2013), which caused structural damages to local buildings and were felt as far as 1000 km away in Chicago, Illinois. In September 2016, a M 5.8 seismic event near Pawnee, Oklahoma, altered local groundwater formations (Manga et al. 2016). Furthermore, fluid injection under gravity effect with zero wellhead injection pressure could also induce seismic events as the initial pore pressure of the reservoir is increased by the injected fluid. Examples of these events are in the Raton Basin in southern Colorado, USA, where induced seismicity is occurring since 2001 including two major events with M 5.3 & M 5.0 (Rubinstein et al. 2014). Such increase in induced events rate urged a modification in water disposal regulations in USA (Stewart & Ingelson 2017), and has driven focused research on hazard quantification and risk analysis prior to injection-related activities (e.g., Petersen et al. 2016).

1.2.2 Seismic Events Caused by Hydraulic Fracturing

Most hydraulic fracturing jobs normally doesn't cause large seismic events, only microseismic events resulting from fractures creation and growth are recorded. These microseismic events usually have negative magnitudes. However lately, few large-magnitude events have been reported and raised the awareness about the hydraulic fracturing operations as a potential source of seismicity. Unusual seismic activity has been noted in the Barnett Shale plays north Texas, where shale gas is being multi-stage fracked in which nine seismic events with $M \geq 3$ happened since the start of field development in late 1998, a large number in a region known to have none in the preceding 25 years (Frohlich 2012). Furthermore, seismic events with maximum magnitude around M 3.0 were recorded during hydraulic fracturing operation south Oklahoma, and they are suspected to be resulted from the hydraulic fracturing (Holland 2013a).

Starting from 2009 and till 2011, unprecedented pattern of 21 earthquakes with maximum magnitude M 3.8, was recorded in the Horn River Basin of British Columbia, Canada. BC Oil and Gas Commission investigated the incident and derived a conclusion that those events “were caused by fluid injection during hydraulic fracturing in proximity of pre-existing faults.” (BC Oil and Gas Commission 2012), moreover, these events are considered the largest induced by hydraulic fracturing. Similar happened near Blackpool, UK, in April 2011, where a M 2.3 seismic event accompanied hydraulic fracturing operation in a shale play (Clarke et al. 2014).

1.2.3 Seismic Events During Heat Extraction from Geothermal Reservoirs

During hydraulic stimulations of Groß Schönebeck geothermal field in Germany in 2007, very few seismic events with magnitudes ranging between M -1.8 to M-1.0 were recorded by down-hole detection networks. Most of these earthquakes were recorded during the stimulation of the volcanic portion of the reservoir, compared to the sandstone portion (Kwiatek et al. 2010). In 2000, thousands of micro-earthquakes were recorded during the eight major hydraulic stimulation jobs performed in Soultz-sous-Forêts geothermal field, Alsace, France, with maximum magnitude earthquake was M 2.9. Seismic events with magnitudes up to M 2.9 occurred after six days of the main hydraulic stimulation of the Basel geothermal field in Switzerland, followed by several events with magnitude $M > 3.0$ even after the injection-well shut-in. These earthquakes were felt by people. A total 3500 seismic event were recorded in the region in 2006, which had led to the abandonment of \$60 million geothermal project (e.g.,

g., Häring et al., 2008). More than 45,000 seismic events were recorded, with maximum magnitude of M 3.7, during the hydraulic stimulations of Cooper Basin geothermal reservoir in Australia which started in 2003.

Moreover, several seismic events have resulted from other fluid injection and/or extraction activities; ground subsidence caused by oil production of the Goose Creek oil field, Baytown, Texas, was thought to be the trigger of 1920s' seismic events (Pratt & Johnson 1926), and the series of events that have occurred due to production in the Groningen gas field in the Netherlands starting from 1991 to the present. Similar occurred in Wilmington oil field, California where six microseismic events occurred between 1947 and 1955. Another major seismic event was induced intentionally for scientific purposes during the water flooding of the Rangely oil field in Colorado in the 1960s (Raleigh et al. 1976), where high permeable path from the well to the fault caused the fault to slip and triggered seismic events only hours after the injection start. Another concern about induced seismicity in gas storage reservoirs is that even small seismicity can adversely affect the integrity of the sealing faults in the reservoir. Lately, in 2013, a series of seismic events with maximum M 4.2 hit Castor gas storage reservoir near the Spanish coasts (Gaite et al. 2016).

1.2.4 Geological Features Affecting Triggering Seismicity

No clear proportionality between the seismicity intensity and the fluid volume injected is established (e.g., Frohlich et al. 2015, Gobel 2015). For example, EarthScope Transportable Array recorded only nine events of nearly $M > 1.5$ were during the course of 2.5 years in the Bakken Shale of North Dakota, with maximum event of M 2.6. Also, only two seismic events were recorded since 2008 in ComCat, North Dakota; the larger one was with M 3.3 in 2012. Furthermore, there were induced seismic events in Texas, Colorado and California, but with local effect limited to a number of wells (Hornbach et al. 2016). Additionally, the GeneSys geothermal field in Hannover, Germany, is characterized by low seismogenicity, where 20000 m^3 was injected in two wells to stimulate the formation, and almost no seismic events were recorded (e.g., Orzol et al. 2005), even though the recording networks were able to observe events $M \geq -0.5$. On the other side, Oklahoma state has witnessed over 2,500 M 3.0 earthquakes and over 9,000 M 1.5 earthquakes between 2008 and 2017, most of them were likely induced, including five $M \geq 5.0$ earthquakes to date. Although high injection rate was used in all these cases, seismic severity differs from site to another (Keranen et al. 2014, Hornbach et al. 2016). Another example of the complexity of relating seismicity rate and the fluid injected volume is the Salton Sea Geothermal field, where the seismicity rate increases with the net volume of fluid produced, not injected. Unexpected relation that contradicts what have been observed in other sites (Brodsky & Lajoie 2013).

From the above examples it is agreed that induced seismicity varies in distribution from a region to other according to the underground geological settings as well as injection operating parameters. If the injection well(s) is connected to nearby faults through direct pathways, the induced seismicity will likely to be local and limited to the surrounding fault planes (e.g., Raleigh et al. 1976). But, on the other hand, if the pressure diffusion process takes long pathways to reach faults, seismic events will occur in a distant location from the injection well or set of wells after a period of time. Additionally, permeability barrier such as large sealing faults or stratigraphic transitions can limit pressure perturbation propagation (Lambert 2017). Examples of the latter are seismicity concentration within Cogdell field carbonate reefs near Snyder, Texas (Davis & Pennington 1989), and reefs edges in Alberta, Canada (Schultz et al. 2016). Furthermore, pore pressure perturbation may result in aseismic movement of favorably oriented faults.

1.2.5 Which Activity Has Higher Potential of Inducing Seismicity?

The duration and the injection volume determine the extent of pore pressure perturbation, and hence, affects the rate and magnitude of the induced earthquakes. Longer injection period gives sufficient time for earthquakes to nucleate, while large injection volumes allows the pressure perturbation to propagate further into the reservoir and more likely to cause failure of larger faults. These factors may explain why the observed seismic events induced by longer-duration injection activities (water disposal, water flooding, and geothermal heat extraction) have higher rate and/or magnitude than those resulted from short-durations operations like hydraulic fracturing. This explanation is in agreement with the events reviewed by (e.g.; Davies et al. 2013, Rubinstein et al. 2014, and Keranen et al. 2014). For example, US Department of Energy stated that seismic events occurred near unconventional oil and gas plays in Oklahoma were caused by water disposal in deep wells and not by hydraulic fracturing operations (US Department of Energy 2016). Downhole microseismic surveys have been conducted in many reservoirs during hydraulic fracturing operations, and results show that most events have magnitude less than -1, with few earthquakes reach 0 or slightly higher. Actually, the above mentioned cases are the only large events reported to be caused by hydraulic fracturing (Maxwell 2013).

Rubinstein & Mahani (2015) suggest that, for the same duration and volume of injection, the probability of inducing seismic event due wastewater disposal into undisturbed reservoirs is probably higher than water injection in hydrocarbon or geothermal reservoir. They contribute this observation to the fact that stresses in hydrocarbon and geothermal reservoirs are already perturbed due to fluid extraction and re-injection (production and water re-injection in hydrocarbon reservoir or water cycling in geothermal reservoirs) and pore pressure is not expected to rise above the pre-perturbation value, while injecting into virgin reservoir will raise the pore pressure above its initial value.

Crossplots of seismic moment versus activity size introduced by McGarr (1976) to study the effect of activity scale on stress field perturbation. Also, crossplots of maximum seismic moment versus injection volume for a group of earthquakes from various activities including hydraulic fracturing, geothermal, and water disposal have been constructed by (Maxwell 2013 and McGarr 2013). As noticed from (**Figure-1.3**), for approximately the same volume injected, hydraulic fracturing produces lower moment event than water disposal and geothermal applications.

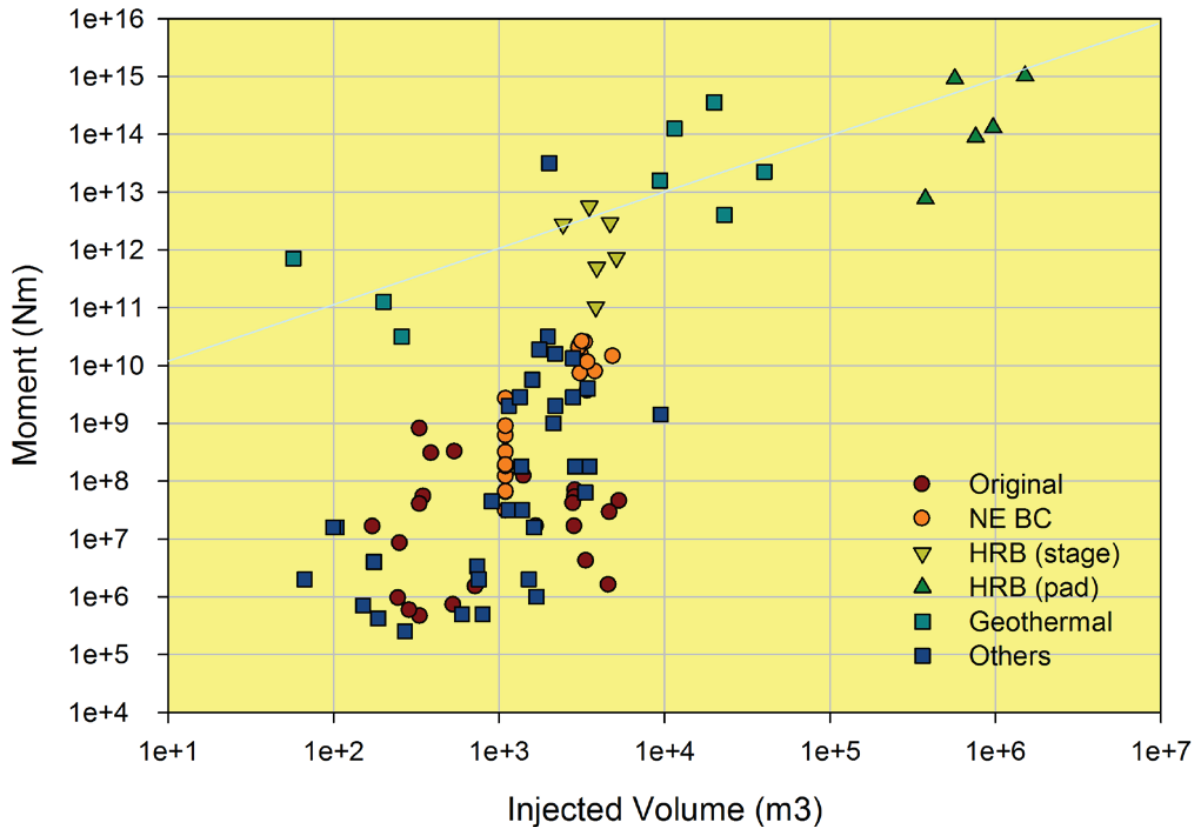


Figure-1.3: Injected volume vs. induced moment for events: north-east British Columbia NE BC, Horn River Basin HRB for both stage averaged fracking and total pad and for geothermal reservoirs such as (Basel, Soutz, Cooper Basin) and other reported hydraulic fracture events. (Courtesy of Maxwell 2013)

1.2.5.1 Seismogenic Index

Shapiro et al. (2010) introduced the seismogenic index Σ to provide a quantitative tool to describe and evaluate the seismotectonic conditions of the reservoir of interest; $\Sigma = a - \log F_t \cdot S$, where a is a constant from Gutenberg-Richter law, S is the poroelastic compliance, and F_t is the tectonic potential of the site; $F_t = \frac{C_{max}}{K_f}$, where C_{max} is the maximum critical pressure of pre-existing fractures, and K_f is the fracture concentration (derivation of the relation can be found in Dinske & Shapiro 2013). Seismogenic index represents how the reservoir area responds to an injected unit volume of the fluid. It can be employed, together with the Gutenberg-Richter law's b -value, to predict number of seismic event with a magnitude larger than M induced by injection in a given reservoir.

Dinske & Shapiro (2013) calculated the seismogenic index for a group of reservoirs including geothermal and petroleum reservoirs. Their results show higher seismogenic indices for geothermal reservoirs than hydrocarbon reservoir, additionally, geothermal reservoirs have lower b -values than those of petroleum reservoirs, both features make the geothermal reservoirs capable of producing higher magnitude earthquakes.

1.3. Mechanism of Induced Seismicity

Stresses underground develop as a result of different processes that differs spatially and temporally. Topographical, gravitational, paleo-tectonic and tectonic processes results in stationary large scale stresses, while processes like erosion, sedimentation, regional seismic cycle, aseismic creep results in transient stresses. Human activities that perturb underground

stress field such as mining, tunneling, drilling, impoundment, fluid injection and/or production are considered to develop local stresses (Nicholson & Wesson 1990, McGarr et al. 2002) that disturb the existing state of stress and might result in fault slip and seismicity. However, current seismological technologies are not able to discriminate human-made activities from natural tectonic ones.

All anthropogenic activities can perturb the state of stress around the fault, and hence ease failure and slip, in four different ways: (1) Pore pressure increase, hence reducing normal effective stress on the fault and increasing shear-to-normal stresses ratio which can overcome frictional resistance of the fault surface, (2) Fluid compression inside the rock matrix inducing deformations described by the poroelasticity theory, (3) Thermal stresses due to colder fluid injection in higher temperatures reservoirs (this factor could not be neglected in high temperature and geothermal reservoirs where subsurface temperature might reach 400 °C or higher), and (4) Mass increase, and hence stresses, in the reservoir. Failure process is described by Mohr-Coulomb failure criteria (Figure-1.4).

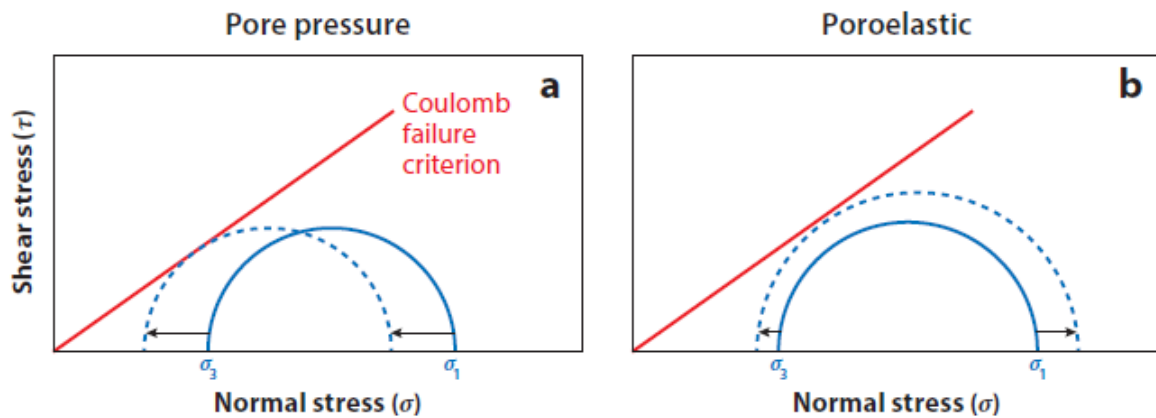


Figure-1.4: Schematic illustration of pore pressure perturbations and poroelastic changes effects on fault stability. (a) Increasing pore pressure reduces normal effective stress, shifting the fault closer to the Mohr-Coulomb failure envelope, (b) Increasing poroelastic stress increases differential stress (Keranen & Weingarten 2018).

For deeper understanding of the mechanism of injection-induced seismicity, different parameters are discussed; These parameters are (1) Subsurface stress field (2) Fractures and Faults Structure (3) Failure criterion and Failure dynamics (4) Fluid-related stress perturbation.

1.3.1 Subsurface Stress Field

The stress acting on a rock element is represented by a stress tensor, defined by three principal orthogonal independent stress components $\sigma_1, \sigma_2, \sigma_3$. Generally, principal stresses correspond to vertical stress, minimum and maximum horizontal stresses. Regarding geothermal reservoirs, most EGS projects are executed in a strike-slip ($\sigma_H > \sigma_V > \sigma_h$) or normal faults ($\sigma_V > \sigma_H > \sigma_h$) (Cloetingh et al. 2010).

Vertical principal stress magnitude can be acquired from density well logging, from which the overburden weight is estimated. Minimum and maximum horizontal stress orientations can be inferred from well breakouts, hydraulic fracturing, or well tests. Mini-fracturing is used to determine magnitude of minimum horizontal principal stress σ_h . However, the estimation of the maximum horizontal stress σ_H magnitude is possible with certain assumptions and relations (e.g., Vernik & Zobak 1992).

In hydraulic fracturing operations of geothermal or oil and gas reservoirs, the amount of energy release during seismic event will be higher with increasing the stresses acting on the reservoir

of interest (Izadi 2012). Dieterich et al. 2015 suggest in their model that the cumulative number of events, the largest event magnitude, and the distance at which the events occur will increase with increasing shear stress applied on the fault surface. They show mathematically that increasing the contribution of the shear stress to the occurrence of an earthquake will decrease the required pore-pressure change to induce the earthquake (Gaucher et al. 2015).

1.3.2 Fractures and Faults Structure

Fracture heterogeneity plays a crucial role in determining max magnitude of an induced seismicity, as it governs the pressure diffusion process within the reservoir. Bruhn et al. 2015 compared a 3D multi fracture system and a single fault block under a given stress state, and found that different configurations will behave differently, hence, they recommend geophysical survey of potentially slipping faults hundreds of meters from injection wells prior to start of the injection process.

Figure-1.5 shows the established relations between seismic magnitude of an earthquake and the dimension of the slipping fault. A fault with 10 to 40 m in length if slipped 0.01 to 0.1 mm will produce -1.0 to 0.5 earthquake, while for magnitudes $M \geq 6.0$ a fault with several km is required. Fault dimension plotted on the x-axis refers to the length of the fault slipping, therefore it represents a lower bound of the actual fault dimension as in real world part of the fault only slips in a single earthquake. Moreover, observations show that the stress drops during fault slipping ranges from 0.1 MPa to 100 MPa (**Figure-1.5**).

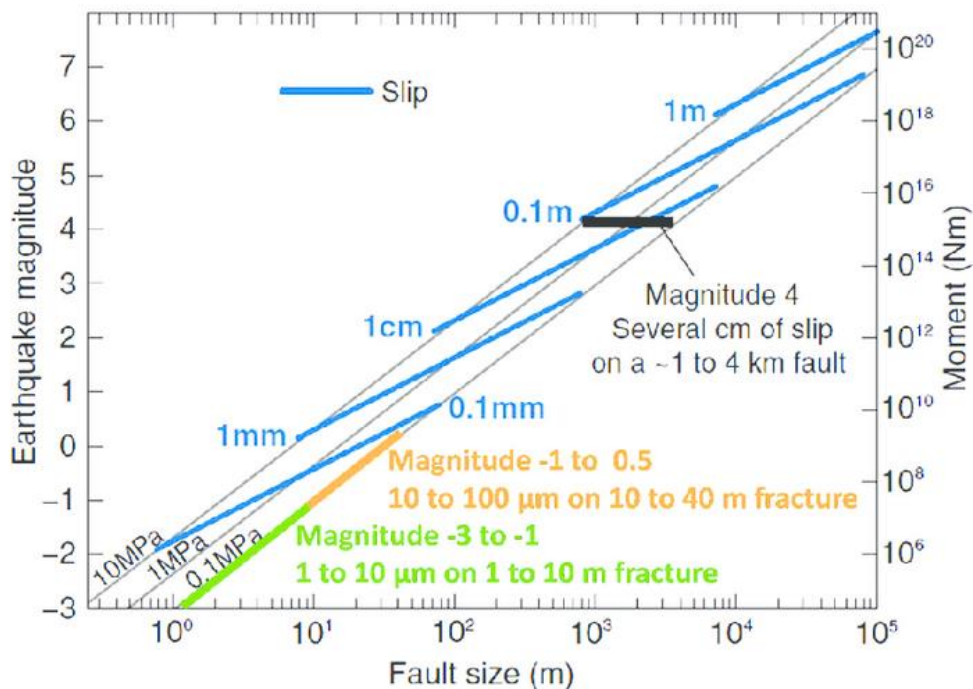


Figure-1.5: Earthquake Scaling (Courtesy of M. Zoback)

Izadi (2012) studied the role of fracture density and distribution within the reservoir inducing seismic events. She used 2 configurations with different fracture densities: $0.1 m^{-1}$ and $0.2 m^{-1}$, and two different fractures distributions (A and B) for each configuration. It is found that fracture density will have a significant effect on the propagation of pressure wave, while fractures distribution has a little effect on the pressure diffusion (**Figure-1.6**).

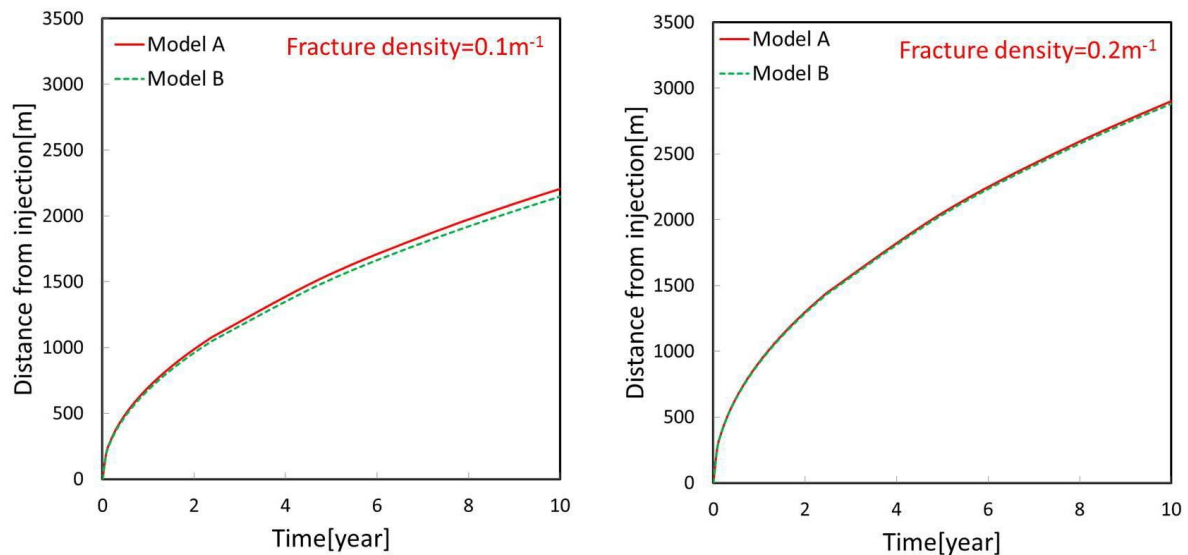


Figure-1.6: Effect of fracture density and distribution on pressure diffusion (Courtesy of Izadi 2012).

1.3.3 Rock Failure Physics

The condition at which the rock fails with respect to its strength characteristics are described by rock failure criterion employed. At the critical state, existing faults are reactivated or the rock ruptures making new faults. Several failure criteria have been developed (Haimson & Bobet 2012). The most applied one is Mohr-Coulomb failure criterion (**Figure-1.4**). This criterion describes the conditions at failure with; $\tau = c + \mu\sigma_n$, where τ , c , μ , and σ_n are the shear stress, cohesion, coefficient of friction, and the effective normal stress, respectively. The effective normal stress is defined as the difference between overburden stress and the rock pore pressure (i.e. stress acting on rock grains). The cohesion usually is assumed negligible, especially when dealing with the pre-existing faults and fractures. Byerlee (1978) found that friction coefficient for intact rock ranges between 0.6-0.85 depending on effective normal stress. However, these values are smaller for faulted rock bodies, ranging from 0.3-0.6 depending on the joint or fault surface roughness.

A major drawback of Mohr-Coulomb criterion is that it neglects the intermediate stress and only considers 2D stress state. Furthermore, Mohr-Coulomb is a linear criterion. Other criteria considers 3D state of stress and the effect of intermediate stress on the strength of the rock, such Drucker & Prager criterion (Alejano & Bobet 2012), Lade and modified Lade criteria (da Fontoura 2012). Also, criteria that describe failure in non-linear dependence of stress such as Hoek & Brown criterion in 2D (Eberhardt 2012) or 3D (Priest 2012) and Griffith criterion. Benz and Schwab (2008), in their comparison of different criteria, found that an extended Hoek & Brown criterion is a better model.

After knowing the geometry of the fault and the underground stress field, these parameters are checked against a strength criterion to assess the risks of a seismic event. These parameters can be input to empirical relations to assign maximum event magnitude to a given fault in the reservoir depending on fault dimensions and the resulting shear displacement (Well et al. 1994, Leonard 2010). Downscaling to fractures size remains an obstacle in front of these empirical relations when applied to reservoirs. A number of linear and non-linear downscaling laws have been developed (Douglas & Jousset 2011).

Fractured reservoirs and EGS fields are assumed to be similar to active tectonic environments as they are characterized by reduced friction coefficient compared to intact rock. Hence, in

tectonically active regions, the probability of induced seismic events is higher compared to tectonically inactive regions (Evans et al. 2012).

According to earthquakes mechanical models, slip along the fault face leads to stress drop, which is accompanied by reducing friction through smoothing of asperities. After faulting process, asperities grow again and re-establish friction. Scholz (1998) described this phenomenon using rate and state variable friction law of Dieterich-Ruina (Dieterich 1979 & 1994, Ruina 1983). He showed that the state of stress can be stable, unstable or conditionally stable. The model is in agreement with the observation that natural earthquake generally happens at depths higher than 3-4 km in the crust. Deeper earthquakes have higher stress drops and rupture widths than shallower ones, because vertical stress increases with overburden (Zielke & Arrowsmith 2008). However, no clear confirmation of this behavior (Allmann & Shearer 2007, Jones & Helmberger 1996). Fluid injection in reservoir reduces differential stress due to pore pressure build-up which possibly results in stress drop reduction (Goertz-Allmann et al. 2011).

Norbeck & Horne (2018) developed a faulting criterion that can be used to assess whether the maximum magnitude event will be controlled predominantly by injection operation parameters or by tectonic factors. Their faulting criterion depended primarily on the state of stress, orientation of the fault, and the stress drop during dynamic rupture. The faulting criterion suggests that for faults with low resolved shear stress, if an event is triggered by fluid injection then its maximum magnitude will likely be bounded by the extent of the pressurized zone. On the other hand, the maximum magnitude event triggered on critically-stressed faults will likely be influenced predominantly by tectonic factors such as geometric or stress heterogeneity.

1.3.4 Fluid-driven Stress Perturbation

1.3.4.1 Fluid Flow

Fluid flow in reservoir is governed by mass conservation and continuity equations. Darcy's law describes fluid flow in the porous matrix: ($v = -\frac{k}{\mu} \nabla p$), where v , k , μ , and ∇p refer to the flow velocity, permeability, dynamic viscosity, and the pressure gradient, respectively. Flow in fractures is described by ($Q = v \cdot w = -w \frac{k}{\mu} \nabla p$), which represents an approximation of Poiseuille law, where w refers to fracture aperture. Fracture permeability can be approximated by $= \frac{w^2}{12}$. This relation is called cubic law as the flow rate increases with the cubic of aperture opening. Asperities on the rough inhomogeneous surfaces reduce the effective aperture and thus decreases the flow velocity (Witherspoon et al. 1980).

Forcing fluid into a fracture enlarges aperture opening by a reversible response resulting from rock elasticity (Bagheri & Settari 2008, Jaeger et al. 2007). Hence the permeability of the rock increases considerably, and the pore pressure build-up decreases. However, with continuing injection process pressure rises and critical stress is reached. Reducing effective stress to a negative value results in tensile failure (mode I) and new fracture are formed. Reactivation of the existing favorably oriented fractures and joints occur as the shear to normal effective stress ratio increases. In case there are no favorable oriented fractures, this shear stress increase may initiate new mode II fractures.

Barton et al. (1985) and Willis-Richards et al (1996) models are most commonly used to simulate fracture aperture change with shearing. Pressure increases rapidly in the reservoir upon the start of injection even relatively far from injection well (because low compressibility of injected fluid). With time, an equilibrium is established between fixed injection rate and permeability increase. Finally, further injection increase will only make incremental increase in pressure as the poroelastic behavior of the rock will translate it into permeability increase.

1.3.4.1.1 Effect of Injection Volume

As noticed from the above review of seismic events, the correlations between seismicity rate and the injection volume is an intricate task as it can be affected by other factors such as the stress state underground. However, if the fault is critically stressed, then once the slip initiates, it will propagate over the entire fault surface. In this case fault dimensions will determine the maximum events magnitude. Although, if the stress state is significantly below the critical state, then the fault slip will depend on the portion perturbed by pressure propagation. The larger the volume perturbed, the larger portion of fault slipping, the larger magnitude of events. This volume of pressure perturbation is directly proportional to the volume injected, hence the maximum magnitude is proportional to volume injected. This behavior is observed in different injection applications such as water disposal, and pressure maintenance in oil and gas reservoirs (eg., Dieterich et al. 2015, McGarr 2013).

McGarr (1976 & 2013) proposes, under a number of assumptions, a relation between the volume injected ΔV into a formation and the maximum seismic moment induced by this injection $M_{o,max} = G \cdot \Delta V$, where G is the shear modulus. When this relation is drawn, it yields a straight line representing an upper limit to the event moment, and it shows that maximum possible seismic moment increases with volume injected (**Figure-1.7**). However, most of events have values which are lower than this limit for two reasons: (1) sometimes the faults slip aseismically (one of the assumptions used in deriving this relation that the formation fails seismically), and (2) formations with high permeability experience little pore pressure rise in response to injection in contrast to low-permeability ones.

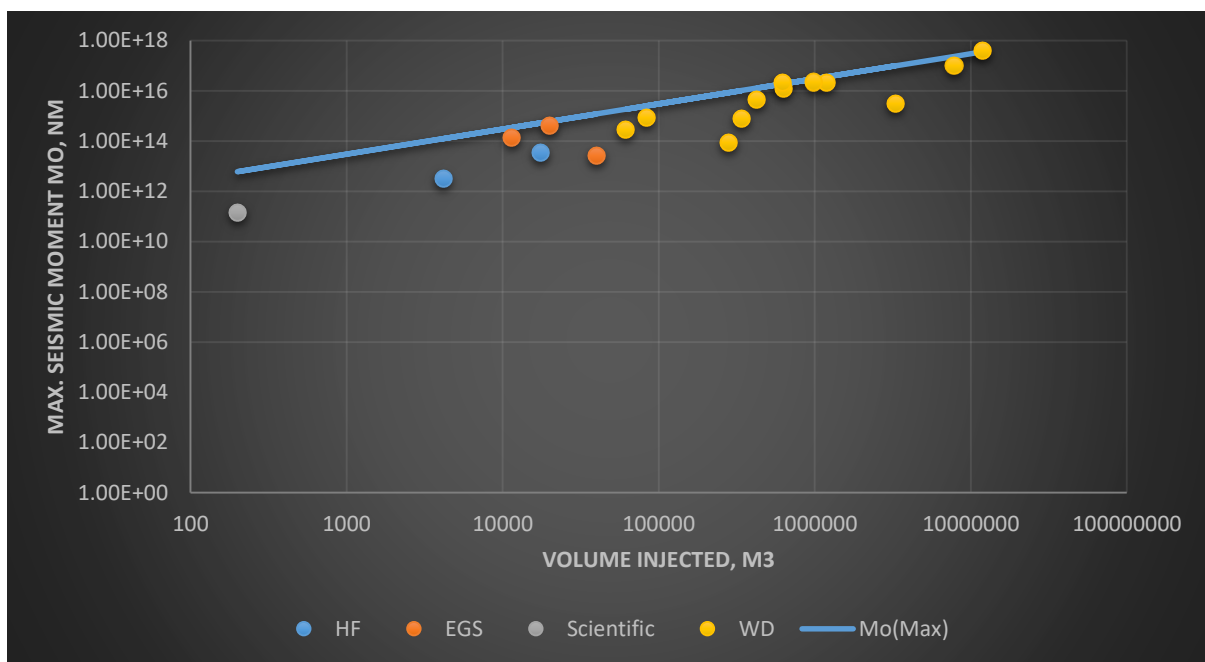


Figure-1.7: Maximum seismic moment as a function of injected volume, dots represent different cases from different activities; HF Hydraulic Fracturing, EGS Enhanced Geothermal Systems, WD Water Disposal, solid line represents upper moment magnitudes (data from McGarr 2013).

Additionally, Dieterich et al. (2015) scale the volume of pressure perturbed V with the event magnitude M for rock matrix-dominated pressure diffusion: $\sim \frac{2}{3} \log_{10} V$, and for fractures-dominated pressure diffusion: $M \sim \log_{10} V$.

1.3.4.2 Heat Transport

Temperature should be taken into account when geothermal reservoirs are considered. Thermal stresses are believed to be a major trigger of induced earthquakes in e.g. The Geysers geothermal field in California, USA (Rutqvist & Oldenburg 2008). Geothermal reservoirs are characterized by high temperatures, therefore, fluid circulation in geothermal reservoir creates thermal gradient in the reservoir. Temperature transfers through advection, conduction, and radiation. Advection and conduction are the responsible to thermal change in reservoir. Advective thermal transfer is associated with fluid mass transfer, and hence is dominant in rock fractures. While conductive thermal transfer is governed by Fourier's law and it is dominant in rock matrix. Temperature affects many reservoir parameters such as volume and viscosity of fluids. Rock volume changes with temperature change according to its thermal expansion coefficient. Since water thermal volumetric coefficient is much higher than that of rock, pores are expected to be affected by thermal changes, and hence, thermal expansion of rock is permeability dependent (Gens et al 2007).

1.3.4.3 Poroelasticity and Thermoelasticity

Geomechanical behavior of reservoir is described by force equilibrium and constitutive equations. These equations describe stress as a function of displacement and strain.

Poroelasticity theory (Wang 2000), which relates pore fluid pressure and stress field, describes how the changes in fluid content of the rock changes the pore pressure, hence changing effective stress acting on the rock and pore and matrix volume. All of which results in additional stress. An analogous coupling, described by thermoelasticity theory (Nowacki 1986), relates temperature and stress. Both theories are merged to develop the thermo-poroelasticity theory. Analytical solutions are derived for a few simplistic cases (Kurashige 1989). For more complicated problems, however, numerical simulation is used to solve the equations either fully coupled differential equations system (Ghassemi et al. 2007) or sequentially coupled e.g. (Rutqvist 2011). Tsang (1991) and Rutqvist & Stephansson (2003) provide a detailed review of coupling schemes used in fractured reservoir simulation.

1.3.4.4 Geochemistry

Little effort has been done on developing geochemical model to simulate chemical interaction in the reservoir. This is due to two main reasons. First, little importance of chemical process in changing the stress field, especially in short time frame. Second reason is the complexity associated with modeling chemical processes in the reservoir. Izadi & Elsworth (2012) presented a coupled thermo, hydro, mechanical and chemical (THMC) model to simulate different processes in EGS reservoirs.

1.4 Forecasting Induced Seismicity

There are numerous models that forecast induced seismicity. They differ according to their input requirement, processing schemes, and computational cost. Models for forecasting injection induced seismicity can be categorized in three categories (Gaucher et al. 2015): statistical, physics-based, and hybrid models. Statistical models aim to reproduce catalogs of recorded seismic events to forecast seismicity in quasi-real time. In contrast, physics-based models are more complex and computationally expensive. These simulate the actual processes taking place in the reservoir and calculate the stress perturbations leading to induced seismicity. The last category of models is the hybrid models which combine both the physical and statistical approaches in forecasting the induced seismicity. In the following section I spot the light on the different forecasting approaches and their advantages and disadvantages, for more detailed review of these approaches please refer to Gaucher et al. (2015).

Forecasting using statistical models requires only catalogs of recorded seismicity pre- and during the field operation. These models are characterized by simplicity, the low computational cost and high uncertainty. However, this category of models does not account for the physical processes leading to seismic events such as permeability changes, co-seismic slip along the faults. Physics-based models, on the other hand, use these catalogs only during history matching phase. They aim at reproducing different thermal, chemical and hydromechanical processes inside the reservoir, therefore, they give better understanding of the subsurface. Physics-based models outperform statistical models especially in case of varying operational parameters, and during shut-in periods, however, they require comprehensive characterization of the reservoir parameters such as the initial conditions of temperature T , pressure P , and stress field σ , and their high computational cost constrain their effectiveness in realtime seismicity processing and forecasting. Hybrid models use physical simulation of reservoir, and implement seismicity catalogs to estimate seismic event attributes following fault slip. The following section discusses some of these models briefly, however, for more details please refer to Gaucher et al. 2015.

1.4.1 Statistical Forecasting Approach

Catalogs of recorded induced seismicity are used to forecast induced seismic events. This is achieved after knowing the natural tectonic seismicity pattern and replicating past seismicity. . Examples of this category of models are Utsu 1961, Hainzl and Ogata, 1999, Wiemer et al. 2009, and Bachmann et al., 2011. Traffic-light system is the most popular statistical approach available. The following section discuss this system.

1.4.1.1 Traffic-Light Control System

Traffic-light system depends on changing injection parameters such as rate or pressure to control and mitigate induced seismicity. This system depends on measuring small and unfelt seismic events by a measuring network and real-time processing of the data, in order to determine the suitable time of intervention and changing injection parameters. Bommer et al. (2006) applied this reactive method to Berlin geothermal field in El Salvador. A number of indicators for the system are set up such as an event with specific magnitude, peak ground velocity, residents reports, or cumulative number of micro-earthquakes. When a predefined threshold of one indicator is overcome, the injection rate is decreased, halted or even the well is bled off. Successful implementation of this system requires proper definition of indicators and their thresholds values, and changing the right injection parameter to mitigate the overcome indicator. Accepted thresholds depends on the human tolerance to seismic events and the structural damage caused by earthquakes. Collecting information about the site is crucial for indicators definition. For example, historical data of seismic events in Basel EGS project are processed to determine threshold event magnitude. In the French Soultz-sous-Forêts geothermal field, seismicity and surface velocity model are used to set a threshold to peak ground velocity.

However, the above described traffic light system is too simplified. Actually, the applied traffic light system in Basel EGS field didn't prevent seismic event even after stopping injection. An earthquake with M 2.6 took place on 8 December 2006 activated the orange level of the traffic-light system and, as a result, injection was reduced and eventually stopped. However, an event with M 2.7 took place four hours later, followed by the maximum one of M 3.4, which triggered the red level of the system and consequently the well was bled off. A sequence of M 2.9, 3.1, 3.2, and 3.3 still happened in that area from January to March 2007. Such traffic-light systems would be inefficient if implemented into the Soultz-sous-Forêts hydraulic stimulations of 2000 and 2003, where M 4.2 events took place days after shut-in (Charley et al. 2007). Thus, it is clearly that the traffic-light system is not able to consider the time-dependence of these events.

Consequently, they can't be relied on to prevent induced seismicity during injection and after shut-in at least at this stage of development, although they are attractive in terms of application.

In GEISER (Geothermal Engineering Integrating Mitigation of Induced Seismicity in Reservoirs) project, a proactive advanced traffic light system ATL has been developed which estimate the probability of seismicity occurrence, and suggests actions. This system is characterized by three features (**Figure-1.8**): (1) Forward looking: ATL is based on rigorous physical model, that forecasts future seismic event and gives preventive warnings. (2) Probabilistic: the system is based on fully probabilistic approach for forecasting that take into consideration both the uncertainties in the physical processes occurring underground, and the randomness of parameters defining these processes themselves. This feature provides quantitative risk and hazard assessment for induced seismicity with different rates and magnitudes. (3) Dynamic: the forecast is updated automatically with any new data available according to an updating algorithm in terms of estimated parameters, time duration and magnitude ranges.

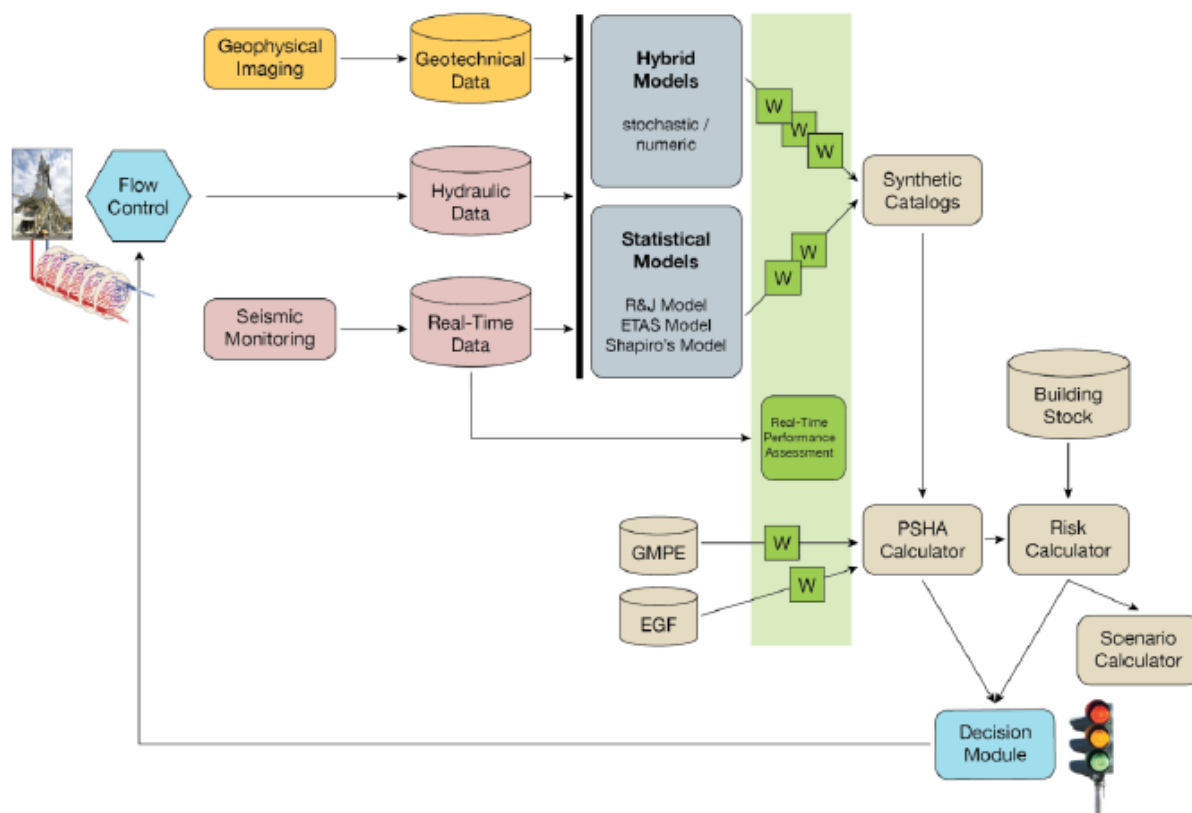


Figure-1.8: Schematic illustration of Advanced Traffic Light ATL system (Bruhn et al. 2015)

1.4.2 Physics-Based Models

The development of computer power and computational capabilities has enabled the solution of geomechanics-related problem in two-dimensions and three-dimensions. The main outcomes of physical models are stresses, displacements, pore-pressure, and temperature. In order to solve a numerical problem, initial and boundary conditions should be defined in terms of formation porosity, permeability, pore pressure, saturations, and in-situ stress field. The applied constitutive laws are used to model the transient stress source due to the anthropogenic stress field perturbations.

The output of stress field of the model is checked against a selected failure criterion. Hence, most of the current physics-based models do not model the co-seismic slip as an implemented

process (Gaucher et al. 2015). As a result, the resulted seismic propensity depends on the given model and many attributes such as, event location, magnitude, amount of energy released, and rupture dynamics) may still unresolved. Nevertheless, Physics-based models theoretically link the induced seismicity with field operating parameters and therefore effects of different operating parameters can be investigated individually.

Examples of physics-based models are Kohl and Megel 2007, Rutqvist & Oldenburg 2008, Baisch et al. 2010, McClure and Horne, 2012, Izadi & Elsworth 2012, Wassing et al. 2014, Jeanne et al. 2015, Urpi et al. 2016, and Safari & Ghassemi 2016. Physics-based models are usually divided into three groups: (1) Matrix-oriented models based on pore pressure transient propagation without any secondary processes modeled, (2) Fractures-oriented models, and (3) Other models that don't belong to the first groups.

1.4.2.1 Matrix-Oriented Models

These models simulate the behavior of reservoir in most simplistic way, eliminating the complexity of modeling fractures. They deal with fluid flow as a pressure diffusion process in two- or three-dimensional medium.

1.4.2.2 Fracture-Oriented Models

These models simulate the pore pressure changes in fractured reservoirs. Fluid flow in EGS reservoirs and hydraulically fractures oil and gas reservoirs depends mainly on the network of fractures, which means that taking fractures into consideration is crucial in understanding pore pressure changes and the associated induced seismicity. Several approaches to model fracture networks can be found in (Willis-Richards et al. 1996, Dershowitz & Einstein 1988).

1.4.3 Hybrid Models

Hybrid approaches combines both physical models and statistical ones. They take advantage of both approaches and mitigate the drawbacks of them. Currently, these approaches use geomechanical numerical models GNMs to calculate stress changes due to injection and to define a failure criterion. Then, this act as the input to the statistical model to assess the probability of seismic event occurrence.

CHAPTER 2: Geothermal Energy: Overview

2.1 Introduction

Earth center has been radiating heat for nearly four billion years. The temperature of the earth center is estimated to be above 5000 C, close to that of the sun, and 42 million megawatts of power are estimated to flow from the earth's center by conduction yearly.

With the demanding shift towards low cost and environmentally low-impact energy resources, the consideration of geothermal resources is usually overlooked among other renewables due to the lack of comprehensive understanding of the processes and interactions within geothermal resources. The Australian Geothermal Reporting Code (2010) defines geothermal resources as “a geothermal play which exists in such a form, quality and quantity that there are reasonable prospects for eventual economic extraction”. It also states that the term geothermal play “is used as an informal qualitative descriptor for an accumulation of heat energy within the Earth’s crust. It can apply to heat contained in rock and/or fluid. It has no connotations as to permeability or the recoverability of the energy.”

Geothermal energy has been used by human for over 10000 years, when Paleo-Indians were first known to use hot springs for heating, cleansing, cooking and meditation. Romans and Ancient Greeks used hot springs as spas. In Pompeii, close to Mount Vesuvius volcano, people used geothermal water for heating. Geothermal water had been used by Romans for healing skin and eye diseases. In Japan, people have been enjoying geothermal spas for centuries (Nersesian 2010).

The first application of geothermal energy in direct heating dates back to 14th century in Chaudes-Aigues, France. Modern applications were in Boise, Idaho in 1892, and Klamath Falls, Oregon in 1900. Commercial application of heat pumps first appeared in Portland, Oregon in 1946. In 1904 in Larderello, Italy, Prince Ginori Conti was the first to exploit geothermal heat in power generation. Larderello power plant is still generating electricity today and it represents 10% of the global geothermal electricity generation.

Geothermal energy has an advantage over other renewable energy sources like wind and solar energy, that it is always available and continuous. It can be employed as a baseload that is available in all seasons.

2.2 Applications of Geothermal Energy

Geothermal resources can be exploited in three ways: power generation, direct heating, and ground source heating. Numerous parameters determine the fitting application of the geothermal resource including: site accessibility, reservoir fluid temperature and pressure, porosity and permeability. Next is a brief about the use of geothermal resources in direct-heating and ground heating and cooling, and the rest of the chapter considers electrical power generation from geothermal resources.

2.2.1 Direct Heating

Geothermal resources can still be used as a source of direct heating in areas where these resources are not sufficient for economic power generation. Direct-heating only require low to moderate temperature resources to supply heat to the residential, industrial and service buildings. Direct-heating using geothermal resources can save up to 80% of the costs of heating using the alternative conventional fossil fuels. A study by U.S. Department of Energy suggests that replacing fossil fuels by geothermal resources in direct-heating would save about 18 million barrels of oil yearly in ten states included in the study (Zoet et al. 2011).

2.2.2 Ground Source Heating

Limited or low-temperature geothermal resources, which can not be employed in power generation or direct heating applications, are exploited using electric heat pumps that transfer heat between the ground and buildings for warming and cooling purposes. Few meters underground, temperature remains fairly constant in the range 10 - 15 C, which makes the ground act as a source for heat during winter and a sink for heat during the summer time (Zoet et al. 2011).

2.3 Overview of the global Market: (GEA 2016)

The amount of global conventional hydrothermal potential is estimated to be 200 GWe depending on the today's available technology. Therefore, only 6-7 % share of geothermal power out of the total global power capacity is based on the current knowledge and technology of the geothermal resources. Figure-2.1 shows the current installed geothermal power generation capacity by country.

Power generation from geothermal resources continuously grows and expands (Figure-2.2 & Figure-2.3). In Central and South America, Elsalvador has plans of increasing its geothermal power generation up to 40 % of its electrical generation stock by 2019. Chile started building its first geothermal power plant and has commenced a 3-year field development plan including wells drilling. Costa Rica put funds for upgrading its the Pailas and Borinquen projects capacities for additional 165 MW. Also, Nicaragua has incentivized renewables to reach a target of 90% of its power needs generated by renewable

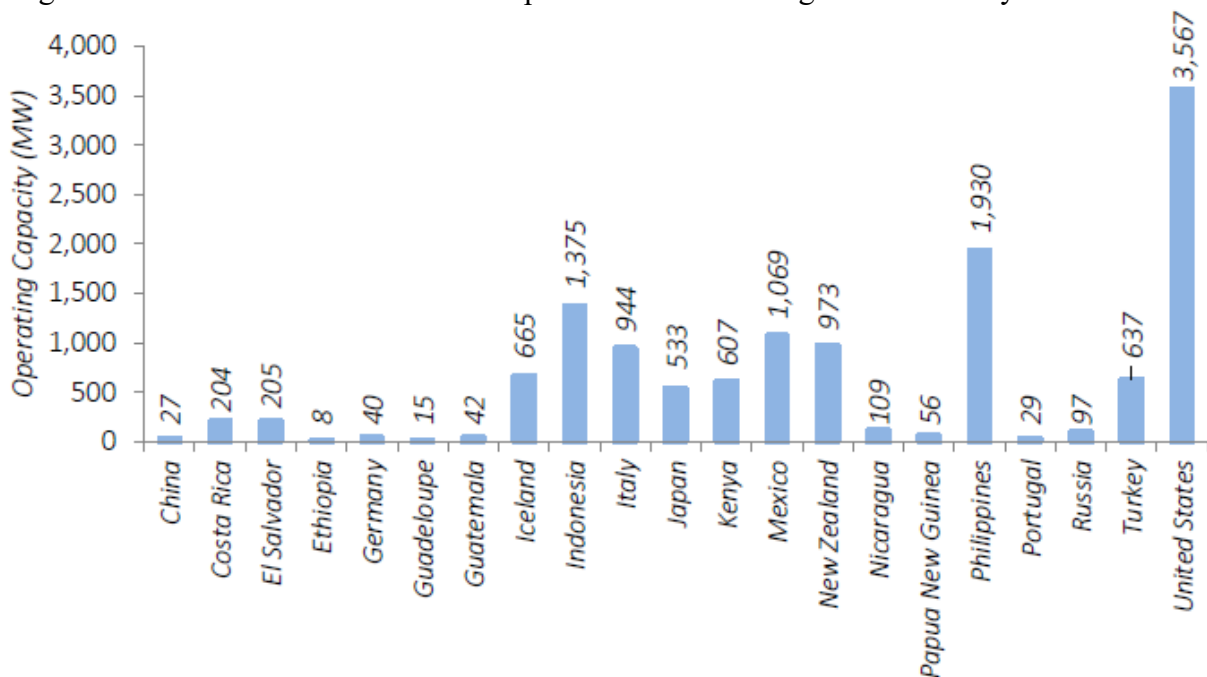


Figure-2. 1: 2015 Geothermal power generation capacity (GEA 2016)

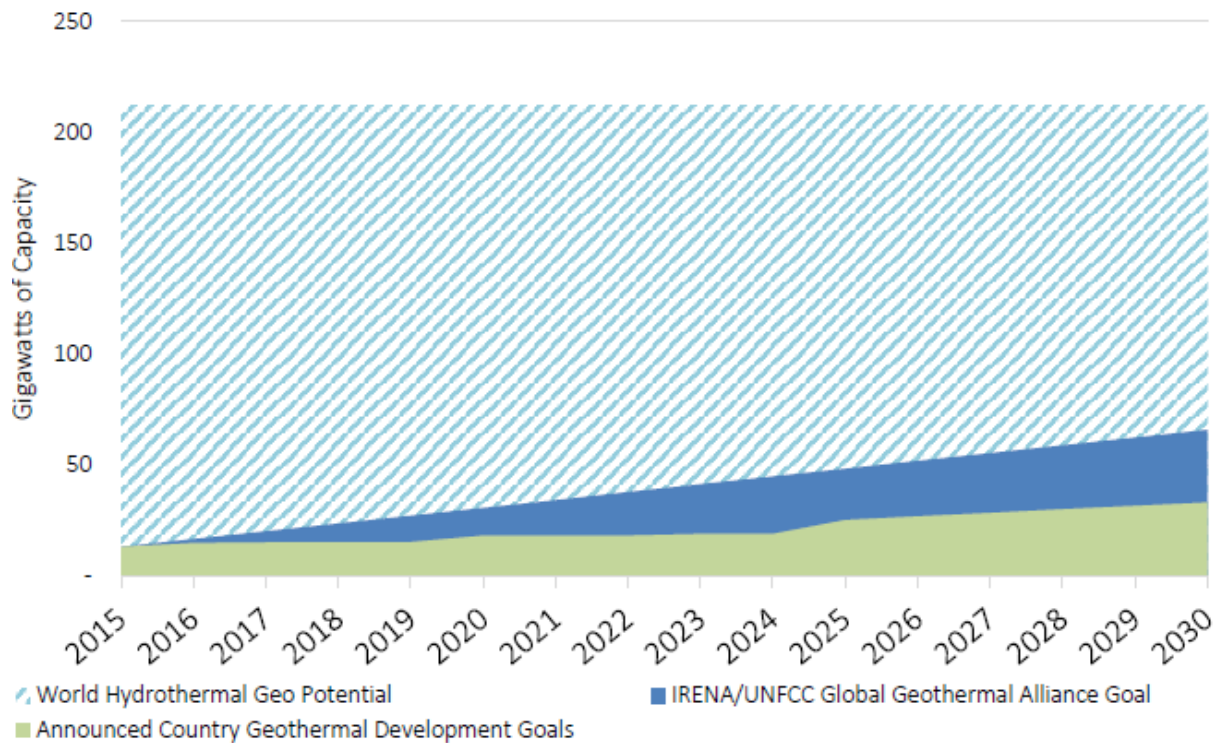


Figure-2.2: Geothermal Potential and the planned future installation (GEA 2016).

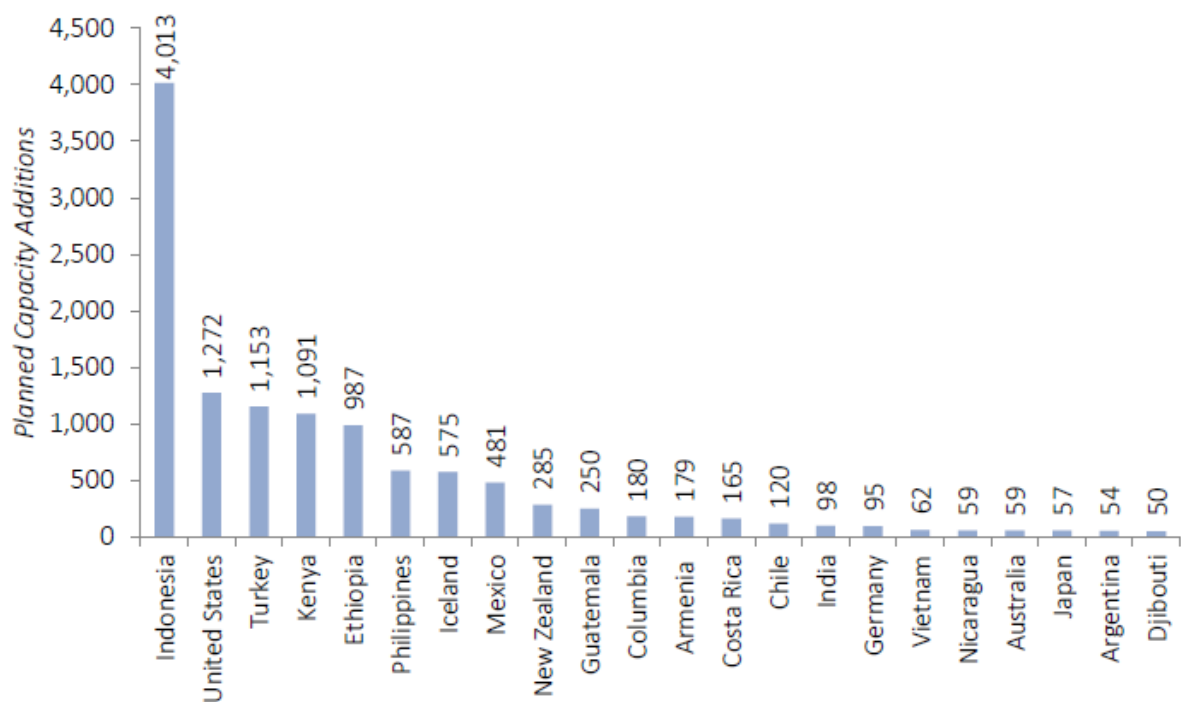


Figure-2.3: Planned additional geothermal power generation capacity installment (GEA 2016)

East Africa has been witnessing a geothermal activity as a number of countries consider entering the market and building their first geothermal power generation plants. In Tanzania, there is a plan of putting 220 MW online from geothermal power generation by 2020. Meanwhile, geothermal power generation corresponds to 50% of Kenya power generation capacity, and it exports its excess geothermal power capacity to Rwanda and Uganda.

In North America, Mexico is building new geothermal power plants projects and upgrading its existent projects. In 2015, Mexico issued new regulations to organize geothermal resources exploitation, as well as leasing and concessions.

Lately, more countries started to explore and develop their geothermal resources. Some of these countries are new entrants which have planned building geothermal power plants in short-run such as Saudi Arabia, Iran and Pakistan. The economics of geothermal resources exploration and exploitation are similar to those of oil and gas resources more than other renewable resources like wind and solar energy. Investors explore for high temperature anomalies.

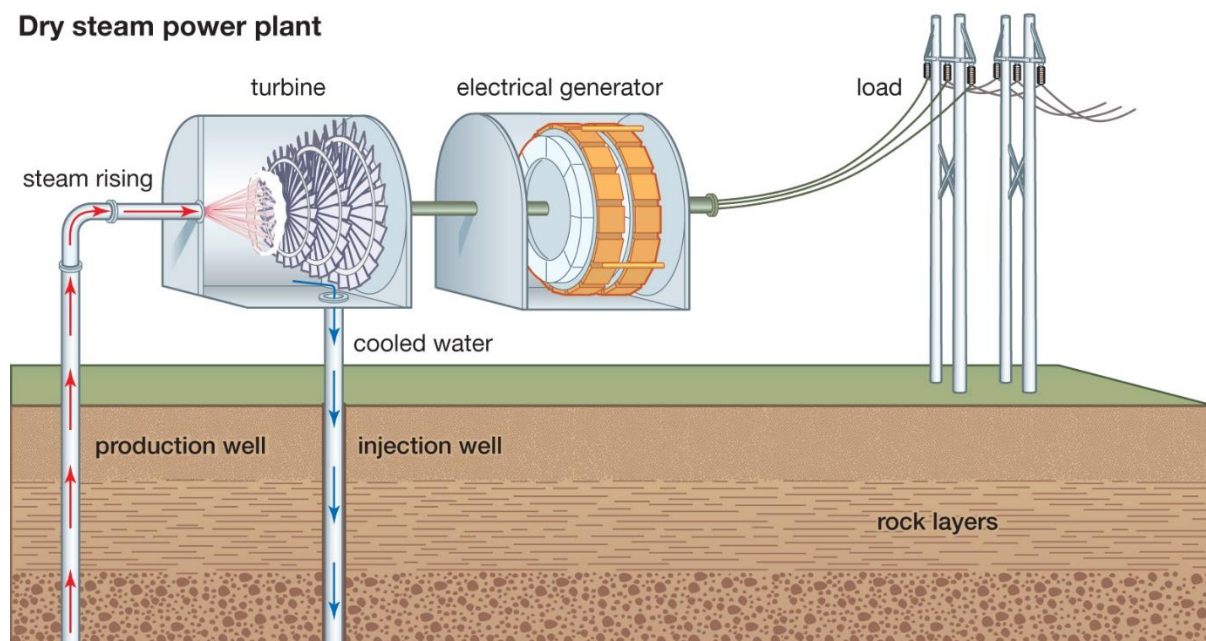
2.4 Current Technology

There are three technologies to operate geothermal power plants: dry, flash and binary steam technologies. Dry steam system is implemented when only high-pressure steam comes from the reservoir and used to operate the turbines feeding the power generators (Figure-2.4). Dry steam power plants are the most efficient technology as they are run by high-temperature steam (230 °C or higher), however, those high-temperature geothermal reservoirs are scarce.

In flash power plants, upstream is composed of high-temperature and high-pressure steam and water where steam is separated to run the turbines. The condensed water from the circulated steam and the separated liquids from the reservoir stream are re-injected back to the reservoir (Figure-2.5) Flash power plants are much more common than dry steam plants and operate in temperature range 150 - 370 °C.

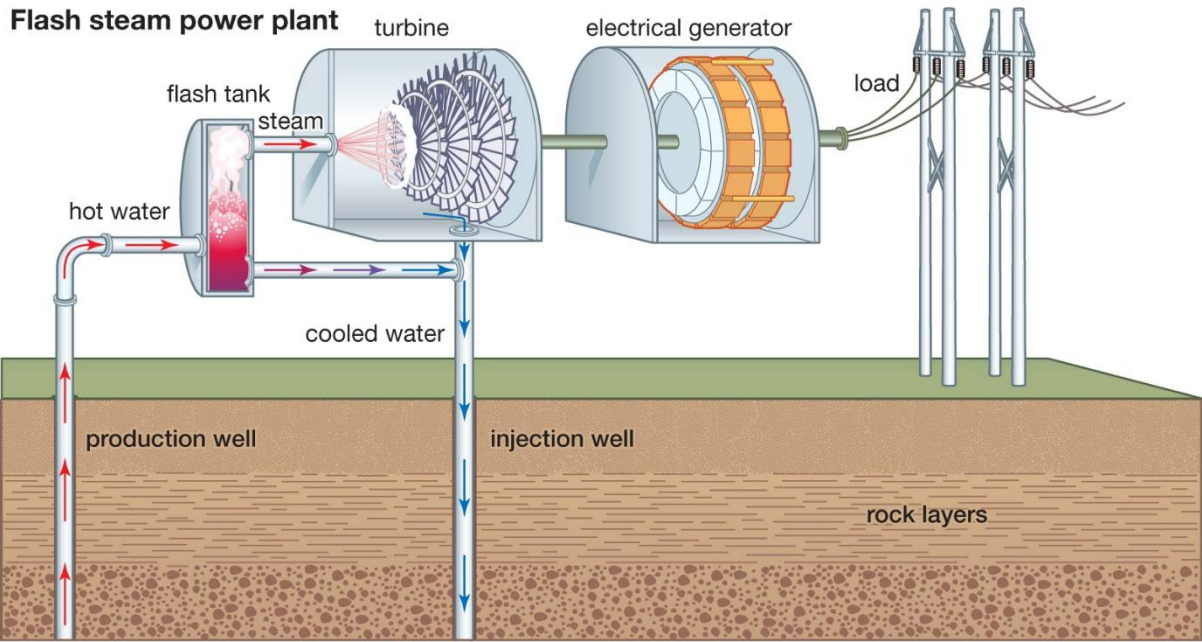
In binary or Organic Rankine Cycle-ORC geothermal power plants, a secondary organic working fluid is vaporized using heat of the reservoir stream. This working fluid is characterized by a boiling point lower than that of water. The vaporized working fluid is used to run the turbine (GEA 2016) (Figure-2.6). Binary power plants can operate at reservoirs temperatures down to 100 °C. Usually the total geothermal stream is reinjected in the reservoir and never allowed to contact with shallow fresh water formations.

Dry steam power plant



© 2012 Encyclopaedia Britannica, Inc.

Figure-2.4: Schematic illustration of dry steam power plant (Courtesy of Encyclopedia Britannica 2012)



© 2012 Encyclopaedia Britannica, Inc.

Figure-2.5: Schematic illustration of flash steam power plant (Courtesy of Encyclopedia Britannica 2012)

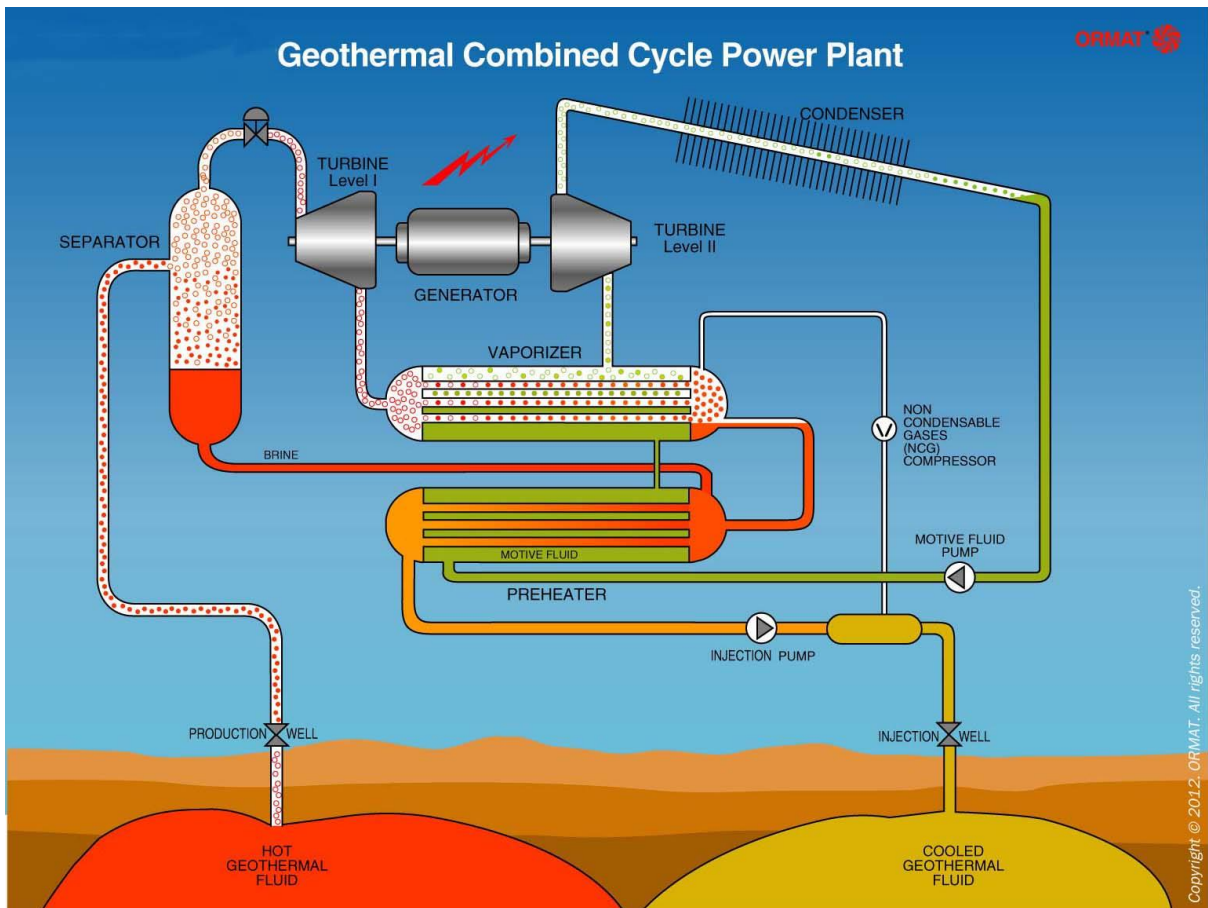


Figure-2.6: Schematic illustration of a binary geothermal power plant (Courtesy of Ormat Technologies).

The choice of the suitable technology for operation depends on the properties of the reservoir. Binary technology fits low-temperature geothermal reservoirs, while dry and flash technologies are suitable for high-temperature fluids, and they are the most widely employed in geothermal power plants around the world. Flash systems, including double and triple flash,

represent up to 58% of the produced megawatts, while dry systems represent 25% and 16% is operated by binary technology. Non-traditional technologies, including back-pressure technology, are used to operate the remaining 1% of the geothermally produced megawatts. Figure-2.7 shows the evolution of the operating technologies of the geothermal power plants. It is noticed that binary technology has been operating since only two decades. This technology could unleash potential lower-temperatures geothermal resources around the world.

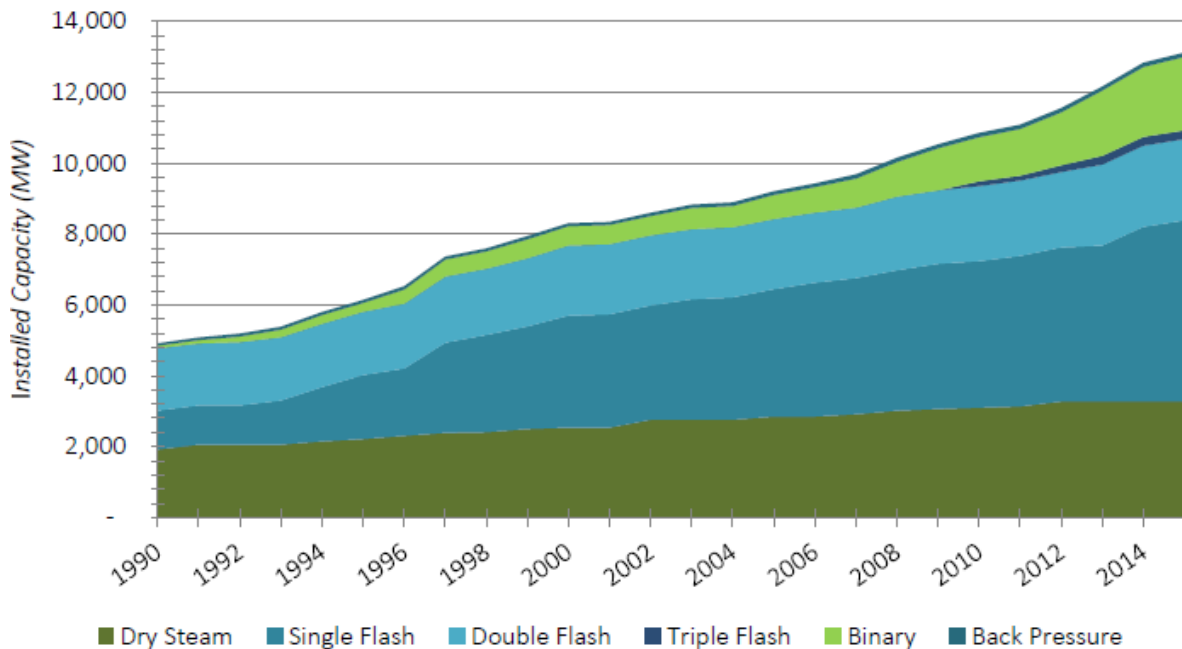


Figure-2.7: Shares of the different geothermal power plants technologies.

Regarding the major technology vendors, Toshiba, Mitsubishi, and Fuji are the major equipment and engineering consultation providers for higher temperature reservoirs. While Ormat Technologies Inc. is the main technology supplier for binary (ORC) power plants in which it has provided turbines for 75% of the binary geothermal power plants, however, many technology vendors like ElectraTherm, Exergy, Turboden are entering the ORC system market. Furthermore, Ormat leads the supply for the whole geothermal turbine market by 26% share, followed by Mitsubishi 18%, Fuji 13% and Toshiba 10% (GEA 2016).

Geothermal Energy Association GEA anticipates substantial growth in binary technology, along with the growth in dry and flash technologies. Binary power plants are the main projects under construction in Europe and the U.S., while countries in East Africa and the South Pacific are building several flash and dry geothermal power plants. In South and Central America countries, where they just started to explore their geothermal resources, GEA expects to have a mix of binary, flash and dry geothermal power plants. Generally, technology advancement will define the temperatures for economic exploitation of the potential geothermal resources in the future (GEA 2016).

2.5 EGS Systems

EGS projects aim to commercially extract heat from less permeable reservoirs by enhancing the permeability and creating a heat exchanging pattern between multiple wells in the reservoir. This technology was first introduced in New Mexico at Fenton Hill location, USA, by Los Alamos National Laboratory. Such reservoirs are referred to as Hot Dry Rock reservoirs HDR where exploration process targets high temperature anomalies. Hot Wet Rock reservoirs also used to describe reservoirs with initial hot water in place. Recently, the term Petrothermal is used for HDR systems to be distinguished from HWR (i.e. hydrothermal or conventional

geothermal) systems. Petrothermal term is also used for EGS projects. There is no agreement on what is denoted by EGS, whether Enhanced or Engineered Geothermal Systems. Hirschberg et al. (2015) suggest to identify the Engineered Geothermal Systems as the Petrothermal systems, as they target to engineer an underground heat exchanger, while they use Enhanced Geothermal Systems for hydraulically stimulated low-permeability geothermal reservoirs. However, for the sake of avoiding confusion, Engineered and Enhanced Geothermal Systems terms are used interchangeably in this thesis to describe any artificial process to increase productivity of the geothermal resource. Details of current EGS projects around the world are found in Hirschberg et al. (2015).

CHAPTER 3: Thermoelasticity

3.1 Introduction

Poroelastic and thermoelastic effects on induced seismicity can be addressed from two related standpoints: (a) their effects on fractures attributes: opening, slip and propagation, and (b) time-scale and impact on the in situ state of stress at reservoir scale. It has been established that thermal stresses could result in critically stresses geothermal reservoirs (Sherburn et al. 2015, Ghassemi et al. 2007, Segall & Fitzgerald 1998). Wang (1993) and Kümpel (1991) reviewed the poroelastic moduli affecting poroelastic induced stresses and their role in solving geophysical problems such as induced seismicity. Segall (1989,1997) and Grasso (1992), among others, studied the poroelastic effects on induced stresses and seismicity during hydrocarbon reservoirs depletion. Germanovich et al. (1998) used semi-analytical approach to the stress changes due to poroelasticity and their effects on fault slip in 2D. Poromechanical effects have been considered in many induced seismicity investigations (Maillot et al. 1999). Segall & Fitzgerald (1998) studied induced stresses due to both poroelasticity and thermoelasticity and the resulting induced seismicity. Mossop & Segall (1997) and Bruel (2002) concluded that thermomechanical processes associated with cool water injection could induce seismicity.

The investigation of thermal stresses and its geomechanical applications has developed through time. Nowacki (1973) reviewed the theoretical and applied thermoelasticity and provided solutions to thermal stresses with many references since early 1900s. Thermal cracking in some igneous rocks has been studied through thermoelasticity theory (Fredrich & Wong 1986), where temperature, and rock properties affecting cracking are investigated. Moreover, experiments have provided evidences of thermal cracking enhancement in presence of water. Findings that lead to investigating the role of thermally induced stresses in hydraulic stimulation of hydrocarbon and geothermal reservoirs (Enayatpour & Patzek 2013, Stephens & Voight 1982).

The thermomechanical process affecting reservoir stress field and fractures propagation during stimulation of hydrocarbon reservoir have been investigated (Perkins & Gonzalez 1985, Hagoort et al. 1980). Also, early studies tried to investigate thermoelastic processes in geothermal systems (Lowell 1990, Bodvarsson 1976, Bodvarsson & Lowell 1972, Lister 1972). Bodvarsson & Lowell (1972), as well as Lister (1972), studied the thermomechanical effect of fluid circulation in the ocean floor. Elsworth (1989) used 1D heat transfer model to investigate the thermoelastic effect on fractures openings. Nygren and Ghassemi (2006, 2005) and Nygren et al. (2005) used a semi-analytical 1D heat and fluid diffusion approach to study the injection-induced thermoelastic and poroelastic effects on fault parameters (e.g., displacement, aperture, and fluid pressure).

Many publications have considered heat extraction through numerical simulations (Ghassemi et al. 2003, Willis-Richards et al. 1996, Kohl et al. 1995). 3D thermal stresses accompanied with cool fluid injection into a planar formation have been developed (Mossop & Segall 1997). Kohl et al. (1995) developed a finite element coupled hydro-thermo-mechanical model. Also,

finite element method, along with discrete fracture networks DFN, have been to study the effects of injection pressure change in fractured reservoirs (Megel et al. 2005, Bruel 2002, Willis-Richards et al. 1996). In those studies, 1D approach for heat transfer and thermal stress was used.

Ghassemi et al. (2007) found that, in addition to the tensile stress developing due to contraction by cooling, compressive stress develops in the portions of the rock outside the fractures and joints. This is also observed by Segall (1989) when he used a poroelastic approach to study the earthquakes occurring on the flanks of hydrocarbon reservoir during production. Segall & Fitzgerald (1998) studied induced stresses due to both poroelasticity and thermoelasticity and concluded that thermoelastic stresses dominate poroelastic stresses in geothermal reservoirs and may be responsible for induced seismic events. It is noticed that rock around the injection well contracts within months of the beginning of injection. This observation is supported by the reduction of pore pressure around the injection well. Poromechanical process is active since the start of the injection process, and its dominance over the thermomechanical processes depends on the time scale and injection parameters. Thermomechanical stresses have important effect in the long-term of the injection process (weeks, months to years).

3.2 Thermoelasticity and Fracture Attributes

Fracture permeability has a critical role in temperature and thermal stress distribution in the reservoir. Higher fracture permeability results in a homogeneous and gradual distribution of temperatures around the injection well, and thermal stress development at further distances from the well. However, this behavior is mainly controlled by matrix permeability; for very low permeability matrix, fracture permeability does not much affect the development of temperature and thermal stress distribution around the well (Jansen & Miller 2017). Additionally, matrix permeability affects the temperature and thermal stress envelope evolution inside the reservoir. For low matrix permeability, heat transfers by diffusion which slows down thermal stress evolution and temperature change to only the region around the injection well, while for highly permeable matrix, heat transfer through advection from fractures to matrix, hence, thermal stresses develop to larger magnitudes at further distances from the reservoir depending on other parameters such as injection rate, temperature contrast between injected fluid and reservoir, etc. However, the first case is more favorable for a sustainable geothermal reservoir to avoid premature cooling down of the reservoir (Jansen & Miller 2017). Moreover, it has been shown that tensile stress developing in the cooled zone results in lateral microcracks orthogonal to the main fracture path (Chun 2013, Gor & Prevost 2013).

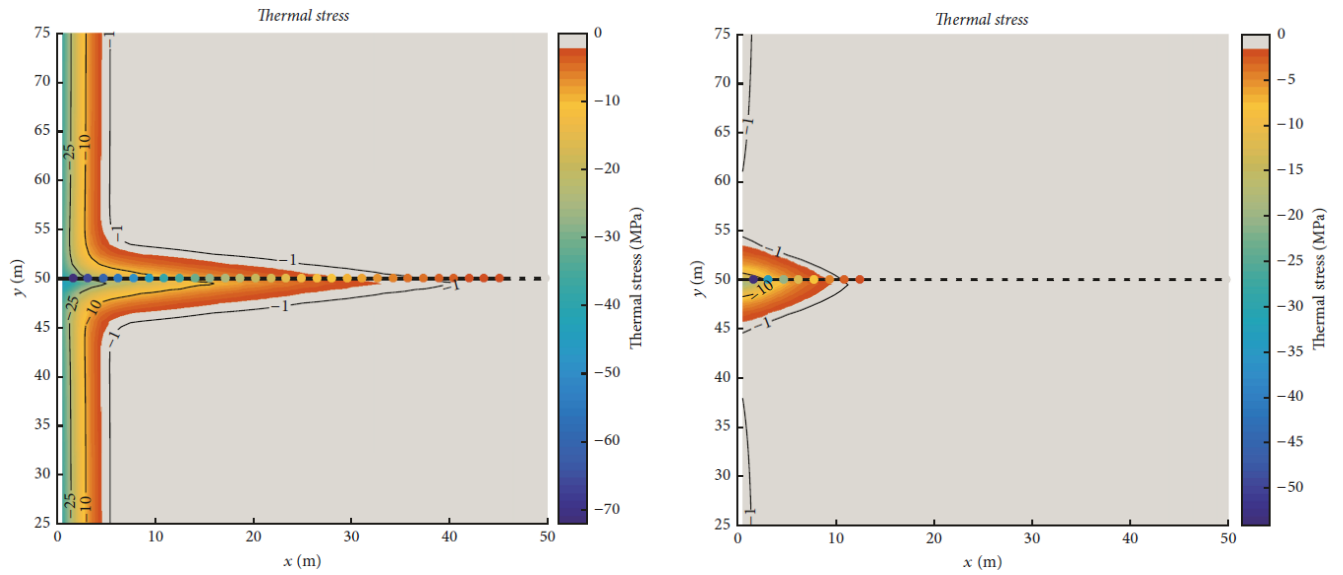


Figure-3. Thermal stress profile after one month of injection. Fracture permeability $k_{fr} = 10^{-10} \text{ m}^2$: (a): higher matrix permeability $k_m = 10^{-16} \text{ m}^2$; (b): lower matrix permeability $k_m = 10^{-18} \text{ m}^2$ (Jansen & Miller 2017).

Moreover, thermal stress induces slip on a wider range of fracture orientations compared to only poromechanical effect. However, taking the advantage of thermal stresses in stimulation operation needs larger time scale which may be beyond the actual hydraulic stimulation period (Jansen & Miller 2017). Although, several numerical simulations studies show that the thermoelastic effects enhances failure and fracture formation and growth during hydraulic stimulation of hydrocarbon reservoirs and geothermal reservoirs (Perkins & Gonzalez 1985, Taron & Elsworth 2011, Enayatpour & Patzek 2013). Taron & Elsworth 2011 suggest that temperature change, along with fluid flow, introduce "disequilibrium" in chemical reactions which may play a role in the different thermo-hydro-mechanical-chemical THMC processes inducing seismicity in geothermal reservoir.

3.2 Thermoelasticity at Reservoir Scale

The time scale for poromechanical and thermal processes differs depending on the reservoir characteristics. Thermal processes usually must be considered during long-term injection periods (months to years) and it takes a period of time to develop a considerable stress change. Thermal diffusivity of reservoir rock is of the order $10^{-6} \text{ m}^2/\text{s}$ (Popov et al. 2012, Eppelbaum et al. 2014), which means that it needs around 277 hours for the thermal front to propagate 1 m into the reservoir. Pore pressure increase can activate the slip on the existing joints through decreasing the effective normal stress acting on them. However, slip along faults is not necessarily an indication of pore pressure increase, especially in many cases where injection pressure during circulation is insufficient to initiate slip on the existing fractures. A fact that spot the light on the role of thermoelastic processes (Bruehl 2002, Mossop & Segall 1997, Stark 1990). Stark (1990) found that half of the seismic events in the Geysers geothermal field in northern California was caused by thermomechanical effects due to cool water injection.

For the sake of simplicity, only poromechanical and thermomechanical stresses are considered here, although, stresses due to slip and chemical processes should be generally taken into account. A simplistic formula is driven to account for the poroelastic and thermoelastic stresses induced in the reservoir during a given operation period by using pressure and temperature depletion data (Segall & Fitzgerald 1998), although, the governing equations of the model response are found in section 3.2. Conditions in reservoir resemble uniaxial strain conditions

in which the lateral strain is negligible, therefore, a relation between horizontal stress, vertical stress and pore pressure can be driven as (Engelder and Fischer 1994):

$$\sigma_h = \frac{v}{1-v} \sigma_v + \alpha \frac{1-2v}{1-v} P \quad (4.1)$$

where α is the Biot-Willis coefficient and it is related to drained bulk modulus K_d and the bulk modulus of the grains K_g , and it is defined as:

$$\alpha = 1 - \frac{K_d}{K_g} \quad (4.2)$$

The vertical stress, which is given by the weight of the overburden, is assumed to be constant and is not affected by injection or production of the reservoir (Engelder & Fischer 1994). Under this assumption and accounting for a pore pressure change, Equation-4.1 reduces to:

$$\Delta\sigma_{hP} = -(\alpha - \gamma_h)\Delta P \quad (4.3)$$

where $\gamma_h = \alpha \left(\frac{1-2v}{1-v}\right)$ is the horizontal stress path coefficient, and v is Poisson's ratio.

Thermoelastic Stress: A body contracts or expands in response to any temperature change ΔT . This change in volume called thermal strain and is described by:

$$\varepsilon_T = \alpha_T \Delta T \quad (4.4)$$

where α_T is the coefficient of thermal expansion (1/K). α_T has a positive value of order of magnitude of 10^{-6} 1/K for most materials. For Isotropic materials, thermal strain acts only on the normal strains with the same magnitude. If this strain is restricted (as the case with rock underground), thermal stresses develop:

$$\sigma_T = C \cdot \varepsilon_T \quad (4.5)$$

where C is the elastic stiffness tensor of the material. For isotropic conditions, the thermal strain has only normal components with equal magnitude in which case we can simplify the previous equation to:

$$\sigma_T = \frac{E}{1-2v} \cdot \alpha_T \Delta T \quad (4.6)$$

where E is Young's modulus and v Poisson's ratio. Equation-4.6 is nonzero for the three normal stresses σ_{Txx} , σ_{Tyy} , σ_{Tzz} . It can be noticed that stresses developed depends on the temperature change. Moreover, thermal stress is positive (compressive) in case of temperature increase, while it is negative (tensile) if temperature decreases (This stress convention is the reverse of what is used in FLAC 3D). Thermal stresses magnitude depends on material properties. Assuming a constant thermal expansion coefficient $\alpha_T=10^{-6}$ 1/K and fixed temperature change of $\Delta T = -20$ °C, granite would undergo tensile stress of 2 MPa while sandstone would undergo only 0.8 MPa stress change.

Assuming that the thermal stresses is independent of the in situ state of stress and the pore pressure, the resulting stress can be calculated using superposition of the thermal stress and the effective stress. Changes of in-situ state of stress is negligible over the hydraulic stimulation time scale. Therefore, total stress changes can be predicted as the superposition of pore and thermal stresses:

$$\Delta\sigma = \Delta\sigma_{hP} + \Delta\sigma_T \quad (4.7)$$

In the long-term exploitation of geothermal reservoirs, the reservoir temperature depletes due to cool water injection, while the pressure undergoes little depletion due to substitution of produced fluids with the injected water. However, some geothermal reservoirs have experienced pressure drop during their life (Oskarsson et al. 2015, Monterrosa & Axelsson 2013). By combining Equation-4.3 and Equation-4.6 we get Equation-4.8 to estimate the thermal and poroelastic stresses ratio for a number of geothermal reservoirs for comparison purposes:

$$\frac{\sigma_T}{\sigma_P} = \frac{K\alpha_T\Delta T}{\alpha\Delta p} \quad (4.8)$$

Where K is the bulk modulus. α is Biot's coefficient ranges from 0 to 1. The thermal expansion coefficient α_T has order of magnitude of 10^{-6} , and it is not much affected by pressure and temperature changes (Wong & Brace 1979). Formation of microcracks by differential expansion of mineral grains can lead to changes in thermal expansion coefficient (Cooper & Simons 1977). However, this change is negligible compared the order of magnitude change of pressure and temperature, therefore, the assumption of constant thermal expansion coefficient is valid.

Temperature differences between reservoir and injected fluids are in order of several tens to hundreds degrees Celsius (Sherburn et al. 2015). This temperature difference, along with injection pressure, induce large perturbation in stress field around the injection wells, however, in order to estimate the induced poroelastic and thermoelastic stresses in a given reservoir reasonably the average pressure and temperature change in the whole reservoir should be estimated first. For example, Segall & Fitzgerlad (1998) estimated 2 MPa thermal stresses induced in the Geysers geothermal field in California due to 6 C drop in reservoir temperature in 20 years. Reykjanes (Iceland) geothermal reservoir temperature dropped approximately 20 °C and its pressure depleted by 3.5 MPa in 10 years of operation (Oskarsson et al. 2015). Wairakei reservoir in New Zealand average temperature depletion < 20 °C, while temperature dropped by 85 °C in the injection zone (Clotworthy 2000) and its pressure remains almost constant. Temperature and pressure of Miravalles field in Costa Rica have dropped by 10 °C and 2.4 MPa, respectively in 16 years (Monterrosa & Axelsson 2013), while they have dropped by 5-10 °C and 1.8 MPa respectively in Berlin geothermal reservoir in El Salvador (Monterrosa & Axelsson 2013).

By considering $K=25$ GPa , $\alpha_T=5*10^{-6}$ 1/°C, and $\alpha =0.9$, one can assess the relative magnitudes of thermal and poroelastic stresses induced in the geothermal reservoir. For Reykjanes reservoir the developed thermal stress is almost twice the poroelastic stresses. In Miravalles and Berlin thermal-to-poroelastic stresses ratio is 1.39, while the thermal stresses developed in Wairakei field is 25 MPa, a value that can cause slips and seismic events in critically stressed and favorably oriented faults (Sherburn et 2015). Therefore, by monitoring geothermal reservoir depletion and accurate characterization of reservoir rock elastic parameters, it is possible to assess thermoelastic and poroelastic stresses induced in the reservoir.

CHAPTER 4: Model Set-up

4.1 Description

The simulated layer is of a rectangular shape with sides 3000 m by 1500 m and of unit thickness along z-direction, the injection and production wells are 750 m apart (**Figure-4.1**).

Normal stress regime is assumed where the vertical stress (overburden) is the maximum principal stress, and the maximum and minimum horizontal stresses are 0.83 and 0.63 times the vertical stress, respectively. Displacement is restricted in the lateral and bottom boundaries of the layer, so, only displacement is expected in the z direction at the top of the layer, and a constant overburden stress is applied at the top of the layer. These conditions resemble the uniaxial-strain problem of an infinite lateral reservoir (Engelder and Fischer 1994). After initialization, the model is set to deform elastically and reach equilibrium, then constant injection rate at the injection well, and constant bottom-hole flowing pressure at the producing well are applied.

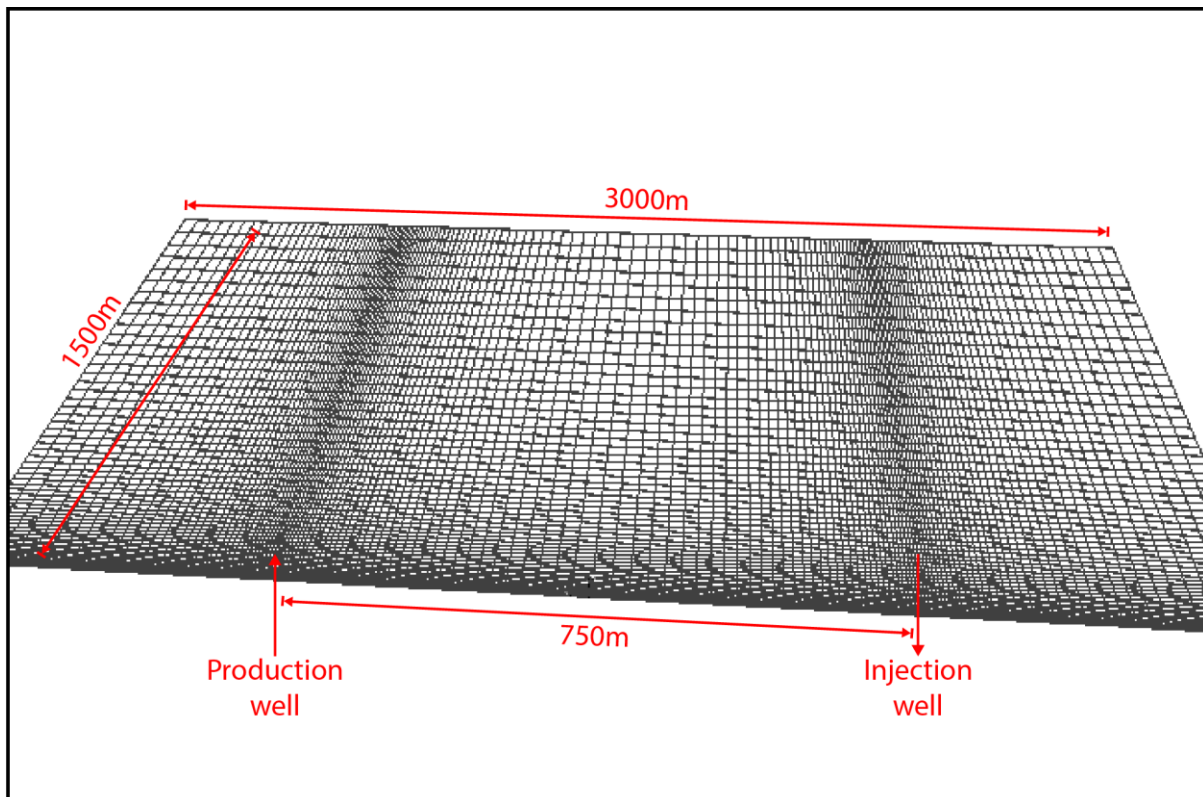


Figure-4.1: 3D view of logarithmically-scaled grid cells of a unit thickness reservoir layer. Each cell represents a fracture orientation at which stability is evaluated each time step, and represents a potential earthquake hypocenter.

The proposed model belongs to hybrid models category where both statistical and physics-based processes are involved. A set of implicit fractures with different adjustable random orientations are embedded in an elastic medium (one fracture plane per each grid cell). Shear and normal effective stress perturbations on the fractures, in response to pore pressure change, are calculated and evaluated against Mohr-Coulomb failure criterion at every time step. Both reversible (tensile) and irreversible (shear dilation) fracture aperture change are considered to account for permeability evolution. Seismic events magnitudes are statistically distributed over grid cells according to Gutenberg-Richter magnitude-frequency distribution with adjustable b-value. Event magnitude for each fracture is used to calculate the magnitude of shear displacement to estimate aperture change. Equivalent continuum permeability is used to describe the permeability evolution for both fractures and matrix.

Simulations are carried out using the geomechanical code Itasca FLAC3D. FLAC3D (Fast Lagrangian Analysis of Continua) is an explicit finite volume method FVM for geotechnical and geomechanical modeling. FVM is a continuum approach that is efficient for fluid flow simulations, so they are suitable for THM coupling at large scale (Jing 2003). Many models are built using FLAC code to investigate induced seismicity by adopting an equivalent continuum approach to model both fractures and rock matrix in fractured reservoirs (e.g., Rutqvist & Oldenburg 2008, Izadi & Elsworth 2012, Wassing et al. 2015, and Nespoli et al. 2015).

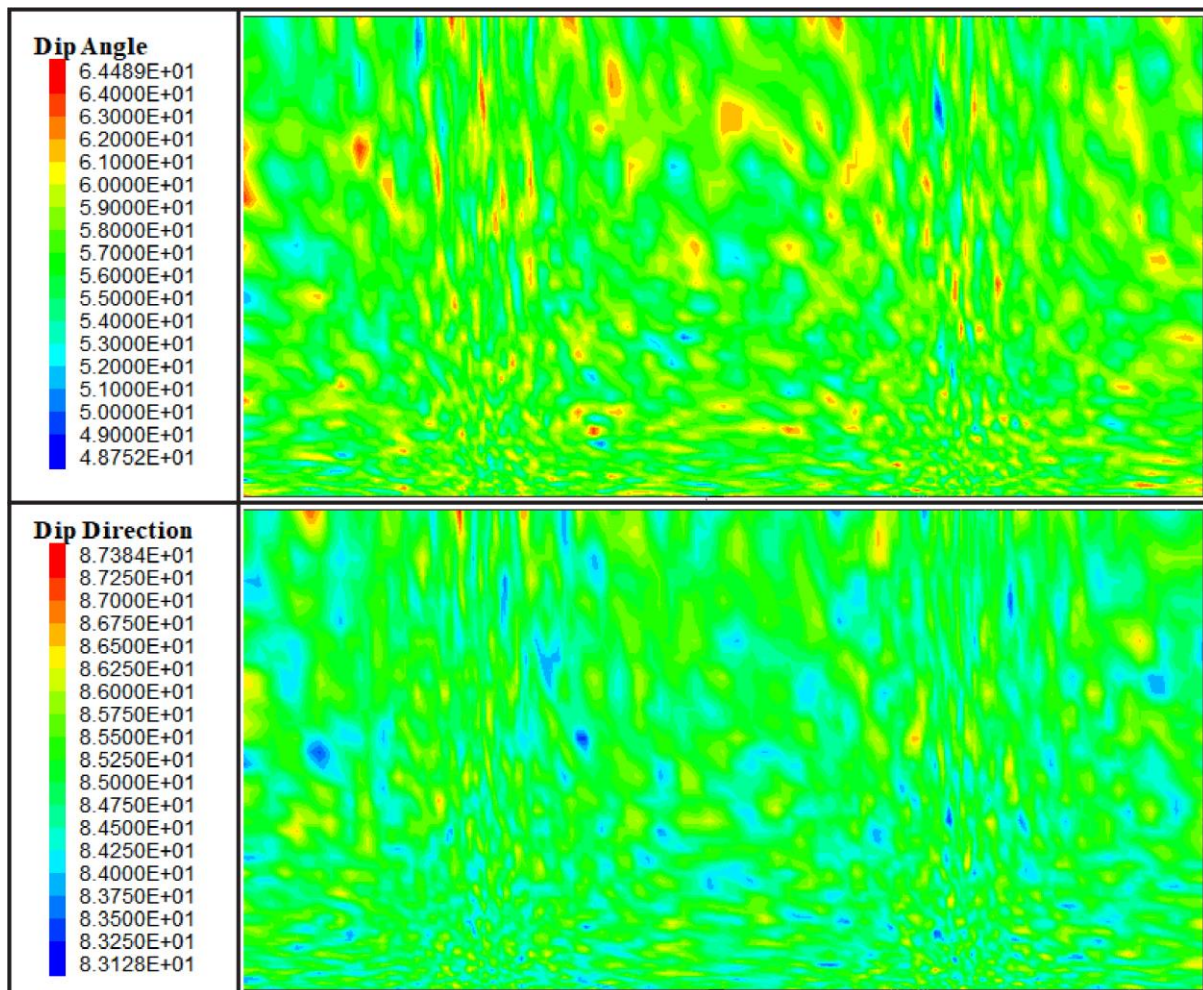


Figure-4.2: Figure-4. 2: Dip and dip directions for a set of favorably oriented fractures introduced into the model representing a worst case scenario (set A in section 5.2).

FLAC3D has a graphical user interface GUI, and a built-in coding language FISH for any user-entered constitutive relations. This language is used to introduce the fracture planes into grid cells (**Figure-4.2**), and to evaluate stability along each fracture using Mohr-Coulomb criterion.

Uncoupled scheme of calculations in FLAC3D is adopted to perform hydraulic, thermal, and mechanical time steps separately, and in the same time, to keep the system in quasi-static equilibrium. **Figure-4.3** shows the algorithm implemented in performing calculations. Cell sizes increases logarithmically with distance from the injection and production sources, with a maximum length of cell 30 m to get a good resolution of pore-pressure propagation, stresses and displacement calculations. Some of the parameters used in setting up the model are taken from (Rutqvist et al. 2013, Safari & Ghassemi 2016).

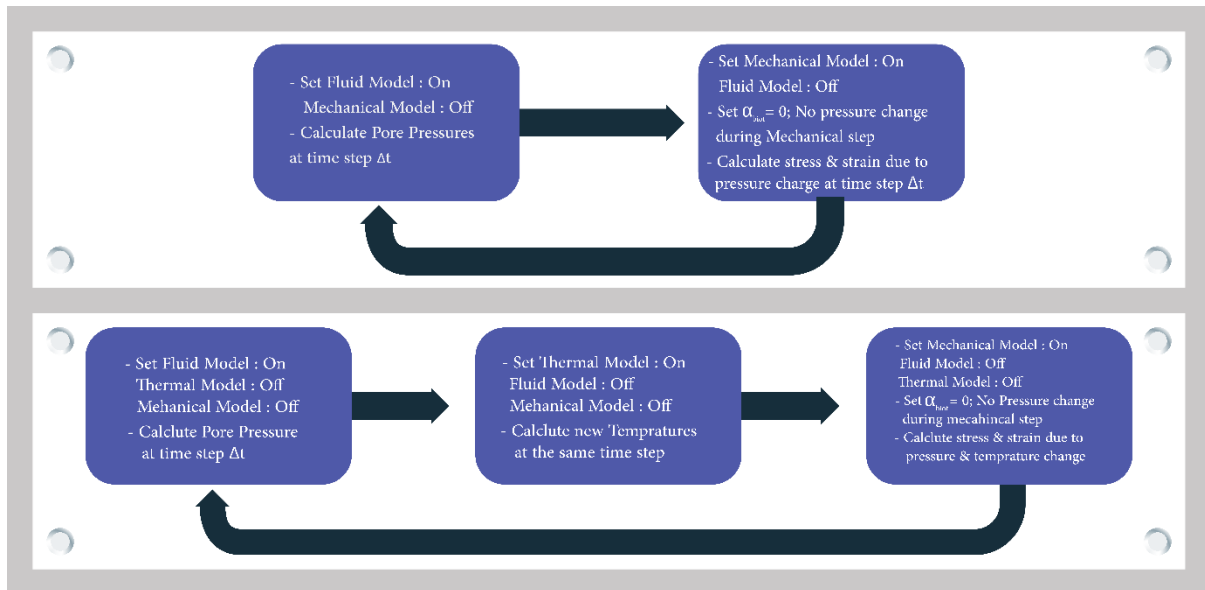


Figure-4. 3: Coupling scheme used in HM calculations (top), and THM calculations (bottom).

4.2 Model Equations

4.2.1 Transient Fluid Flow

Transient flow is assumed around the injection well in which the pressure non-linearly increases with time in response to a constant injection rate (Itasca FLAC3D Documentations).

$$\frac{\partial p}{\partial t} = M(k\nabla^2 p - \alpha \frac{\partial \varepsilon_z}{\partial t}) \quad (4.1)$$

where k is the homogeneous permeability coefficient, M is the Biot modulus, and α is the Biot coefficient. Partial differentiation, with respect to time, of the elastic constitutive relation $\sigma_{zz} - \sigma_{zz}^0 + \alpha(p - p_0) = \alpha_1 \varepsilon_{zz}$ yields, for constant σ_{zz} ,

$$\alpha \frac{\partial p}{\partial t} = \alpha_1 \frac{\partial \varepsilon_{zz}}{\partial t} \quad (4.2)$$

where $\alpha_1 = K + \frac{4}{3}G$, using last equation, and after manipulation, we get:

$$\frac{\partial p}{\partial t} = D\nabla^2 p \quad (4.3)$$

Where D is the diffusivity and is given by $D = \frac{k}{S}$, k is FLAC permeability which equal the intrinsic permeability of the matrix divided by fluid viscosity μ . $S = \frac{1}{M} + \frac{\alpha^2}{\alpha_1}$ is the storage coefficient. As the

problem represents a radial flow in a horizontal unit thickness layer with neglected gravitational effect (i.e. independent of z), pore pressure p can be expressed as:

$$\nabla^2 p = \frac{\partial^2 p}{\partial r^2} + \frac{1}{r} \frac{\partial p}{\partial r} \quad (4.4)$$

By imposing p_0 as initial condition and external boundary pressure and a constant flow rate at the wellbore q:

$$\begin{aligned} p_i &= p_0 \quad \forall r \text{ at } t = t_0 \\ p_e &= p_0 \quad \forall t \text{ at } r = r_e \\ q &= \text{constant} \quad \forall t \text{ at } r = r_w \end{aligned} \quad (4.5)$$

According to Theis (1935), solution has the form:

$$p^* = -\frac{1}{4\pi} E(u) + p_0^* \quad (4.6)$$

Where $p^* = \frac{pk}{q}$, u is a dimensionless variable, and is given by $u = \frac{r^2}{4c(t-t_0)}$, where E is the exponential integral:

$$E(u) = \int_u^\infty \frac{e^{-\xi}}{\xi} d\xi \quad (4.7)$$

After representing σ_{zz} in terms of ε_{zz} by means of the employed mechanical constitutive equations substituting $\frac{\partial \varepsilon_{zz}}{\partial z}$ for ε_{zz} , vertical displacement may be obtained by integrating the equilibrium equation $\frac{\partial \sigma_{zz}}{\partial z} = 0$. After substitution of the boundary condition and using equation 4.6:

$$u_z^* = -\frac{z^*}{4\pi} E(u) \quad (4.8)$$

Where $u_z^* = \frac{uk\alpha_1}{\alpha q H}$ and $z^* = \frac{z}{H}$. The stresses around the wellbore are given from the mechanical constitutive equations and equation 4.6 for p^* .

4.2.2 Permeability evolution:

Continuity equation and Darcy's law describe fluid flow in porous medium. Permeability of fractured reservoirs is controlled by the permeability of fractures which in turn depends on fracture aperture. Single fracture can be described by an aperture between two parallel plates, the permeability parallel to the fracture can be expressed by Poiseuille flow theory (Bear et al. 1993):

$$k_f = \frac{w^2}{12} \quad (4.9)$$

In reality, aperture is not constant and it varies spatially with fracture roughness. Usually statistical average of the aperture is used and constant $C_{kf} = 0.1$ is used to account for fracture roughness. To represent fractures permeability as a continuum equivalent permeability of the simulated layer, the effective up-scaled permeability of fractures is multiplied by the fracture aperture w and divided by fractures spacing L, we get what is called the cubic law:

$$k_{eq} = C_{kf} \frac{w^3}{12L} \quad (4.10)$$

Aperture of the fractures changes with fracture tensile and shear deformation. Aperture change by tensile deformation of the fracture is considered reversible and can be described by Bandis

et al.(1983), where hyperbolic deformation is suggested between the aperture decrease and the increase in normal effective stress acting on the fracture plane:

$$\Delta w_n = \frac{a\Delta\sigma'_n}{1+b\Delta\sigma'_n} \quad (4.11)$$

where a and b are constant; 1/a represents the normal stiffness of the fractures at normal stress equals zero, a/b is the maximum value for fracture closure. Values considered: a=2.5e-8 and b=1.e-4 (Wassing et al. 2014)

Shear deformation of the fractures is irreversible and described using the following relation:

$$\Delta w_s = \Delta u_s * \tan(\psi) \quad (4.12)$$

where Δu_s is the shear displacement, and ψ is the dilation angle of the fractures and is taken 2°.

Shear displacement along fractures are distributed statistically according to the event magnitudes which in turn are distributed according to Gutenberg-Richter law. b-value, a constant represents the seismic activity of a specific site, is used to adjust the range of event magnitudes (Figure-4.x shows Gutenberg-Richter relation for different b values). Once the shear stress along the fracture exceeds the critical shear stress defined by Mohr-Coulomb criterion, the fracture slips and the shear aperture are assigned the distributed value which remains unchanged even after shut-in (i.e., irreversible).

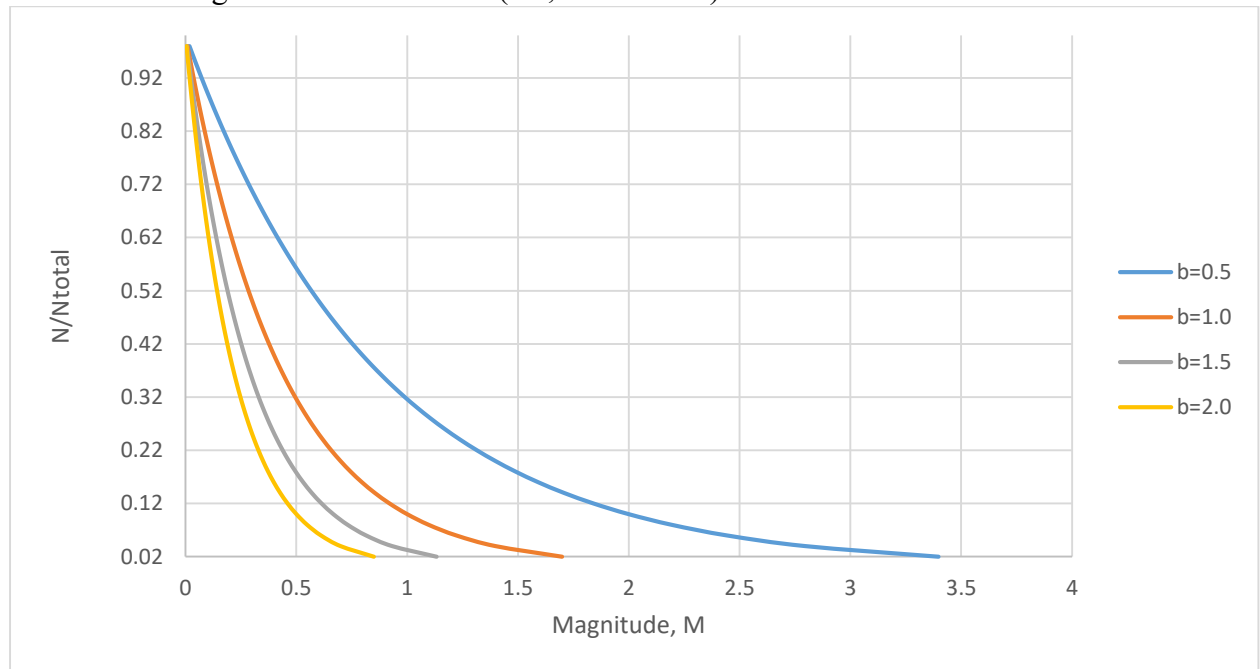


Figure-4. 4:Gutenberg-Richter law for different b-values.

Total change of fracture aperture equals:

$$w_{new} = w_{initial} + \Delta w_n + \Delta w_s \quad (4.13)$$

4.2.2 Constitutive Mechanical Model

Elastic constitutive model is assumed to calculate stresses and strains in the model, while Mohr-Coulomb criterion is used to evaluate the stability along the fractures. This criterion describes the conditions at failure with; $\tau = c + \mu\sigma_n$, where τ , c, μ , and σ_n are the shear stress, cohesion, the friction

coefficient, and the effective normal stress, respectively. The effective stress is the difference between overburden stress and the rock pore pressure (i.e. stress acting on rock grains). The cohesion usually is assumed negligible, along the pre-existing faults and fractures. Parameters used for Mohr-Coulomb criterion are in **Table-4.1**.

4.2.3 Thermal Model

Both heat transfer by convection and conduction are considered in the model to account for heat transfer and temperature changes in fluid and rock matrix. Heat transfer equation:

$$q_T = -k_T \nabla T \quad (4.14)$$

k_T is the thermal conductivity of the medium, and it is expressed for both solid and fluid as: $k_T = k_{TS} + \emptyset S_f k_{TW}$, where k_{TS} and k_{TW} are the thermal conductivities for solid and fluid, respectively, \emptyset is the medium porosity, and S_f is the fluid saturation.

Energy balance equation for convection-conduction:

$$c_T \frac{\partial T}{\partial t} + \nabla \cdot q_T + \rho_w c_w q_w \nabla T - q_{Tv} = 0 \quad (4.15)$$

where q_T is the thermal flux, q_w is the fluid specific discharge, q_{Tv} is the volumetric heat source intensity, ρ_w and c_w are the density and specific heat of the fluid, respectively, and c_T is the effective specific heat of the medium and is given by:

$$c_T = \rho_d c_v + \emptyset S \rho_0 c_w \quad (4.16)$$

Where ρ_d and c_v are the solid matrix bulk density and bulk specific heat, respectively. Thermal model parameters used in this simulation study are in **Table-4.1**.

4.2.4 Thermal-Hydraulic-Mechanical Coupling

Coupling to the mechanical constitutive equations is achieved through effective normal strain rates (total normal strain rate minus thermal normal strain rate components), and pore pressure changes which affect effective stresses. In the model, we coupled the thermo-hydraulic effects to Mohr-Coulomb failure criterion. Furthermore, for an elastic medium, the mechanical constitutive model becomes (Itasca FLAC3D documentation):

$$\frac{\partial \sigma_{ij}}{\partial t} + \alpha \frac{\partial p}{\partial t} \delta_{ij} = 2G \left(\frac{\partial \varepsilon_{ij}}{\partial t} - \alpha_T \frac{\partial T}{\partial t} \delta_{ij} \right) + \left(K - \frac{2}{3} G \right) \cdot \left(\frac{\partial \varepsilon_{kk}}{\partial t} - 3\alpha_t \frac{\partial T}{\partial t} \right) \delta_{ij} \quad (4.17)$$

4.3 Model Initialization and Verification

4.3.1 Initialization

Initial anisotropic state of stress is exerted on the model, with a vertical overburden σ_z acting on the top of the layer, while the displacement is set to zero along bottom and the lateral boundaries of the layer, this is consistent with the uniaxial-strain problem of an infinite lateral reservoir (Engelder and Fischer 1994). **Table-4.1** contains parameters used in initializing the model.

| Parameter | Value | Unit |
|-----------------------------------|-------|------|
| Stress in z-direction, σ_z | 103 | MPa |
| Stress in y-direction, σ_y | 85 | MPa |
| Stress in x-direction, σ_x | 65 | MPa |
| Bulk Modulus, K | 35 | GPa |
| Shear Modulus, G | 2 | GPa |
| Biot's Coefficient, α | 1 | |
| Water Bulk Modulus, K_w | 2 | GPa |

| | | |
|--|------------------------|------------|
| Rock Density, ρ_m | 2700 | kg/m^3 |
| Water Density, ρ_w | 1000 | kg/m^3 |
| Permeability, k | 1e-15 & 5e-15 | m^2 |
| Water Viscosity μ | 0.1 | $c.p$ |
| Initial Pore Pressure, p_0 | 41 | MPa |
| Well Radius, r_w | 0.3 | m |
| Porosity, ϕ | 0.07 | |
| Injection Rate, q | Specified for each run | $l/m/s^*$ |
| Production Pwf | 38 | MPa |
| Matrix friction angle, ϕ_m | 50 | $^\circ$ |
| Joints friction angle, ϕ_f | 30 | $^\circ$ |
| Matrix Cohesion, C_m | 0.5 | MPa |
| Joint Cohesion, C_f | 0 | MPa |
| Joint Shear Stiffness | 20 | MPa/m |
| Joint Normal Stiffness | 20 | MPa/m |
| Thermal Model | | |
| Initial Temperature, T_0 | 250 | $^\circ C$ |
| Matrix Thermal Conductivity | 3 | $W/m.K$ |
| Water Thermal Conductivity | 0.606 | $W/m.K$ |
| Matrix Specific Heat, c_m | 790 | $J/kg.K$ |
| Water Specific Heat, c_w | 4186 | $J/kg.K$ |
| Matrix thermal expansion, α_T | 8.2e-6 | $m/m.K$ |
| Water thermal expansion, α_{Tw} | 0 | $m/m.K$ |

Table-4.1: Parameters used in the simulation study

*If the injection rate is 0.06 l/m/s and the perforated section is 1 km long, then the injection rate is 60 l/s

4.3.2 Verification of Model

4.3.2.1 Pressure Diffusion in the Layer

Pressure diffusion in the layer is solved analytically. **Figure-4.5** shows the match between the analytic solution and model results for the pressure distribution in the reservoir after 8 hours of injection.

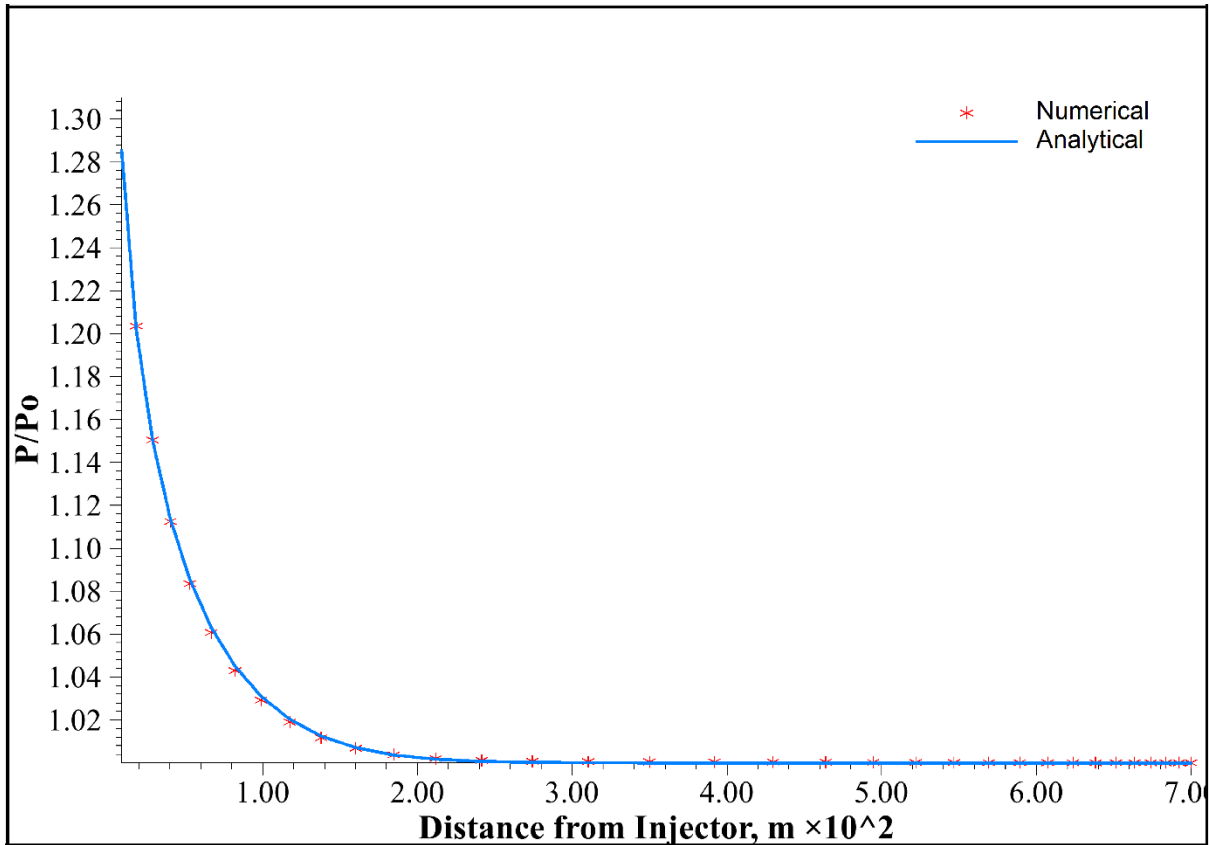


Figure-4.5: Pressure profile in the reservoir. Data shows exact match between analytic solution and numerical results (Parameters in table-3.1 are used in this simulation with injection rate of 0.16 l/m/s).

4.3.2.2 Vertical Displacement

Figure-4.6 shows the analytical solution of the vertical displacement and the numerical results of the model after 8 hours of injection.

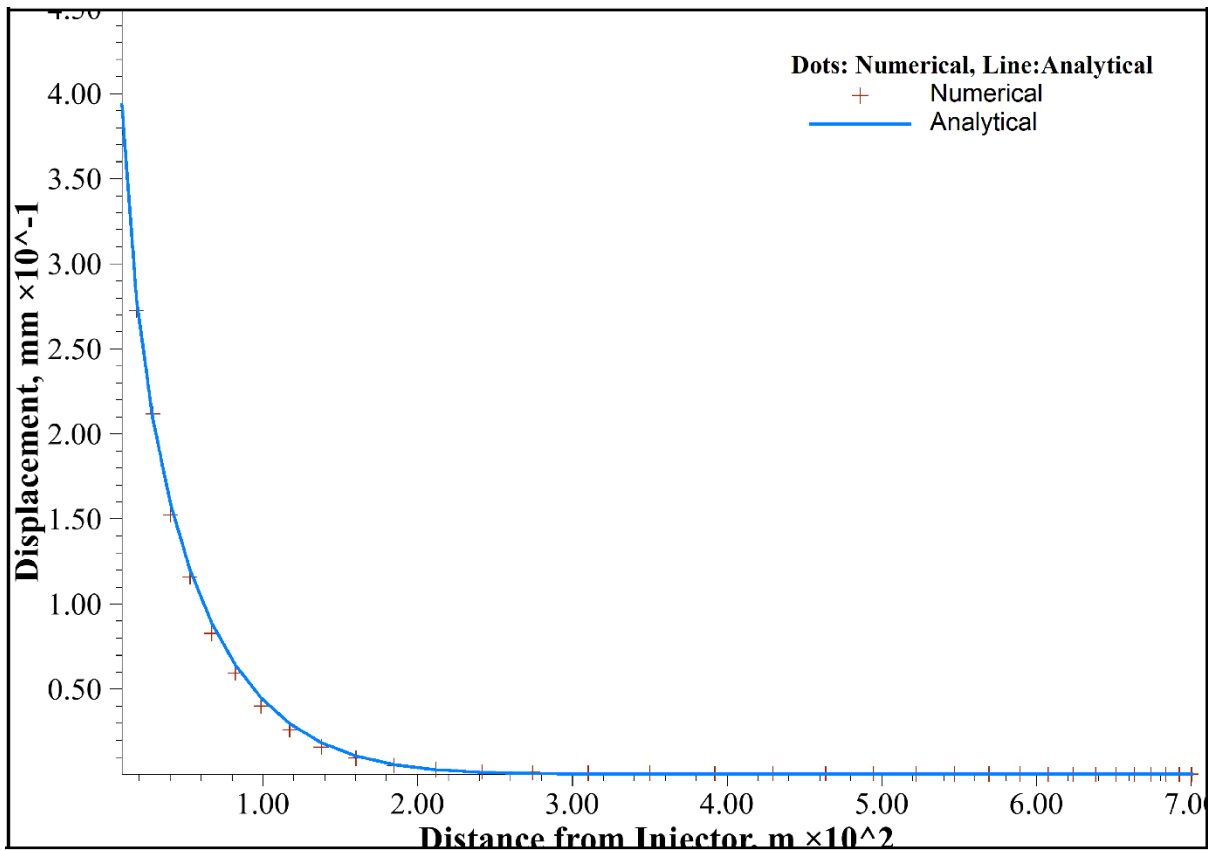


Figure-4.6: Analytical and numerical results of the vertical displacement (Parameters in table-3.1 are used in this simulation with injection rate of 0.16 l/m/s).

4.3.2.3 Fault Reactivation Conditions

Fractures reactivation conditions were reproduced in MohrPlotter software developed by Richard Allmendinger (2014) in Cornell University. The initial state of stress along the fracture plane were set, and, for the given fracture orientation, reactivation pore pressure and friction angle shows exact match between FLAC3D and MohrPlotter.

For example, reactivation conditions for the 45° joint dipping toward positive-x direction (colored dot in **Figure-4.7**) (data in MPa) shows that pore pressure rise from 0.21 to 1.45 MPa reactivates the joint, or decreasing friction angle from 30 to 23.3 reactivates the fault. These conditions are matching with reactivation conditions produced by the proposed FLAC model.

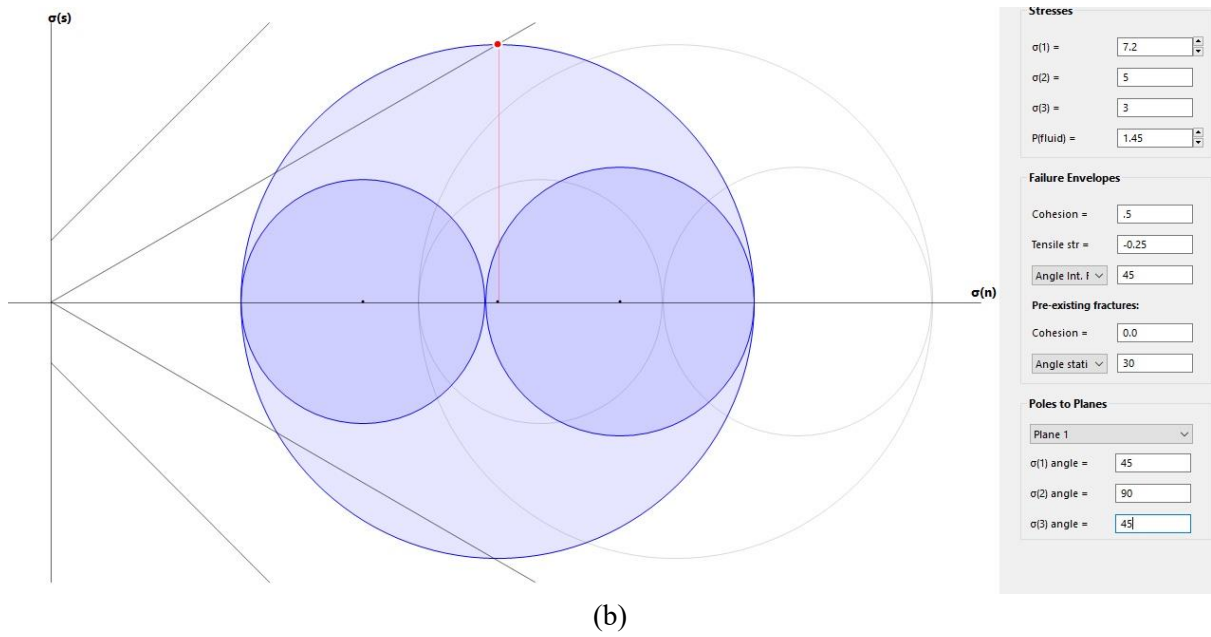


Figure-4.7: 45° joint reactivation conditions from MohrPlotter (software by Allmendinger 2014).

CHAPTER 5: Results

5.1 Introduction

In the absence of hydraulic fracturing propagation where the injection pressure is kept lower than the minimum horizontal stress, the spatial and temporal evolution of induced seismicity is controlled by pore pressure perturbation and the consequent stress relaxation where the increase in pore pressure decreases the effective normal stress acting on the pre-existing favorably oriented fractures and cracks (Shapiro et al. 2007). However, if the injection pressure is higher than the minimum horizontal stress, seismicity is controlled by the parameters of fracture propagation (Shapiro et al., 2006b). In this thesis, slip and shear stimulation along preexisting fractures and cracks are studied, without the intent to induce hydraulic fractures in the reservoir.

Worst case scenario is modelled by assuming favorably oriented set of fractures. For the sake of simplicity, the fractures don't mutually interact. The orientations of the fractures are independent of the spatial locations (i.e., statistical homogeneous random distribution). If at a given distance from the injection point pressure increases and causes slip along the existing fracture, this distance is considered as the hypocenter of the seismic event at that time. Once a fracture slips at a given time step, it is not allowed to heal and keeps slipping during the subsequent time steps. This results in large number of events in the cloud, this assumption may seem unrealistic in the real underground environment. Similar treatment found in Izadi & Elsworth 2012, Wassing et al. 2014.

This part of the study aims to simulate a reservoir with pervasive fractures without a reservoir-scale faults. The seismic events potential appears to resemble a cloud in the spatial-temporal domain. No intention in this stage to study the seismic attributes of the induced events where the statistically distributed event magnitudes only used to calculate the slip magnitude along the fractures used in calculating shear stimulation of the fractures aperture, however, events magnitudes distribution can be tuned to match specific reservoir cases. This chapter present the results of parametric analysis performed on the model. All simulations show a delay of the onset of the first seismic event, because time is required to build up enough to cause poroelastic stress perturbation that results in slip along the fractures. However, once the first seismic event appear, seismicity continues to appear until the end of the simulations.

5.2 Fractures Orientation:

Different sets of randomly distributed 7700 fractures orientations are proposed to study the effect of fracture orientations on the evolution of the injection-induced seismicity.

The initial state of stress in our model corresponds to the stress field acting on a layer at depth of 4 km with the following gradients:

$$\sigma_z = 25.75 \frac{MPa}{km} * 4 km = 103 MPa \quad (5.1a)$$

$$\sigma_y = 21.25 \frac{MPa}{km} * 4 km = 85 MPa \quad (5.1b)$$

$$\sigma_x = 16.25 \frac{MPa}{km} * 4 km = 65 MPa \quad (5.1c)$$

$$P_0 = 10.25 \frac{MPa}{km} * 4 km = 41 MPa \quad (5.1d)$$

The analysis is performed using the following parameters:

| Parameter | Value | Unit |
|------------------------|-------|-----------------|
| $C_{fracture}$ | 0 | MPa |
| $\emptyset_{fracture}$ | 30 | ° |
| Q_{inj} | 0.04 | l/s/m thickness |
| P_{prod} | 38 | MPa |

Table-5.1: Parameters used in simulation runs in Figure-5.1.

Effective normal and shear stresses are calculated for each fracture plane, and slip tendency is evaluated using Mohr-Coulomb criterion every time step. After 60 hours of injection with injection rate of 0.04 l/m/s, it is noticed that favorable oriented fractures undergo slip faster and the seismic cloud becomes denser (**Figure-5.1**).

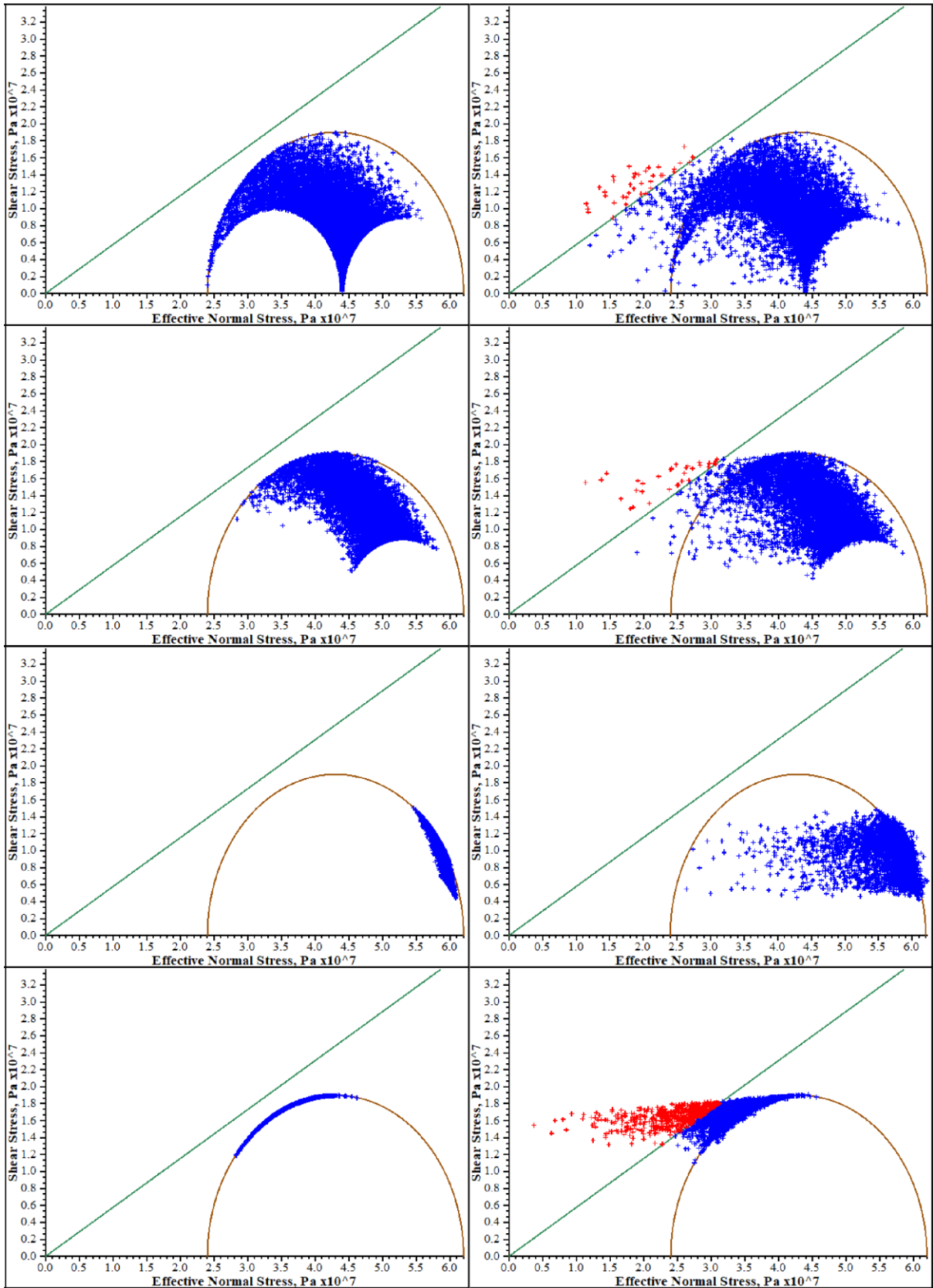


Figure-5. 1: Different initial orientations of fractures (left), and their stress status after 60 hours of injection with injection rate 0.04 l/m/ (right).

5.3 Thermal Stresses

Simulations in **Figure-5.2** show the advance of the thermal front after two, four, six, and eight months from the start of injecting 60 °C cold water. Given the low thermal diffusivity, and permeability of most geothermal reservoir rocks (Popov et al. 2012,) thermal stresses appear to have effect in the long run of operation (months to years). Simulations show that cold water injection induces contractile stresses in the rock which is translated into a decrease in the effective normal stresses acting on fracture planes. Results also show that shear stresses increased in case of non-isothermal modelling, similar findings are observed in Safari & Ghassemi 2016. **Figure-5.3** shows a comparison of the stresses evolution between isothermal (only HM), and non-isothermal (THM) modeling. Pressure-controlled injection with constant injection pressure of 50 MPa is used in these simulation runs.

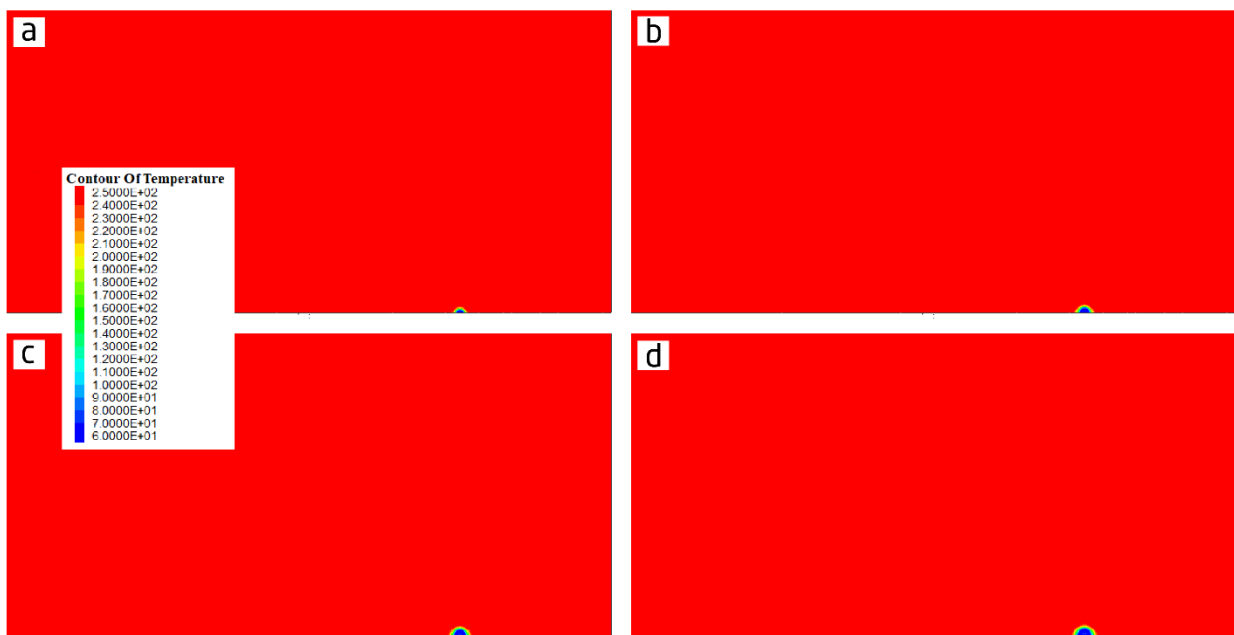


Figure-5.2: Temperature distribution in the reservoir after (a) one month, (b) two months, and (c) three months

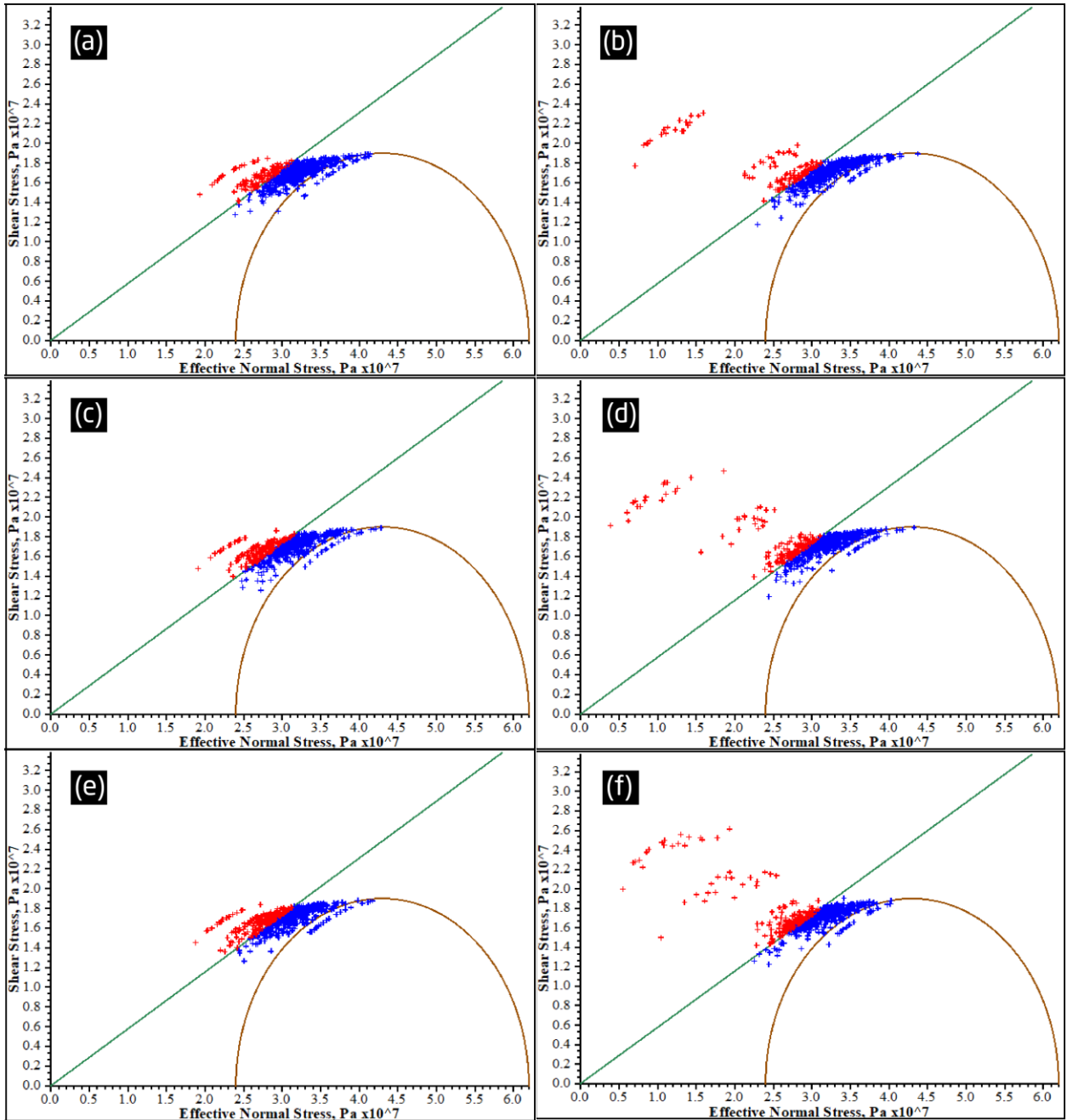


Figure-5.3: (a), (c), & (e): isothermal (HM) evolution of the fractures status after 1, 2 & 3 months, respectively, (b), (d), & (f): non-isothermal (THM) evolution of the fractures status after 1, 2 & 3 months, respectively.

Pressure distribution in the reservoir is simulated for a year for constant injection pressure. It is noticed that after a period of time a steady state flow is established and the pressure does not change with time at any given location in the reservoir (**Figure-5.4**). With such unchanging pore pressure, decreasing effective normal stress and increasing shear stress are attributed to the effect of thermal stresses induced around the injection well due to cold water injection. This can be easily noticed from the closest fractures to the injection well, which undergo the highest effect of thermal stresses. These observations suggest that the evolution of induced seismicity may be driven by the thermoelastic behavior of the rock in the long term. Izadi & Elsworth (2012) found in their thermo-hydro-mechanical-chemical THMC model that at early time (days to months), high injection pressure and rate lead to larger events. While, for long-term

(years) heat extraction and possible chemical reactions mainly induce the seismicity but with a decaying number and magnitude.

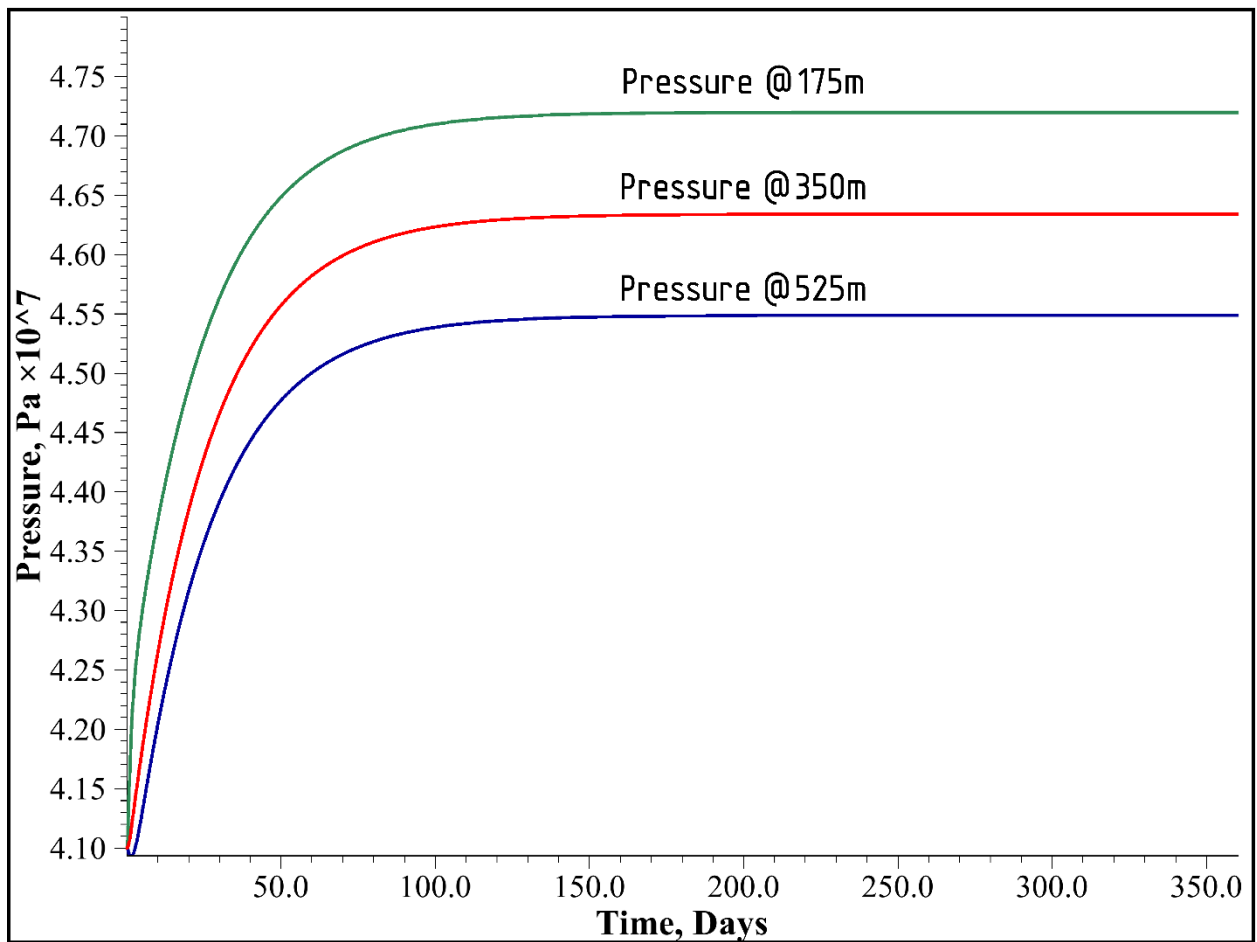


Figure-5. 4:: Pressure vs. time at three different locations in the reservoir.

5.4 Permeability Evolution

Permeability evolution due to normal aperture change and shear stimulation is modelled by considering initial equivalent continuum permeability of $5 * 10^{-15}$. Equations 4.11 & 4.12 are used to calculate tensile and shear change of the fracture aperture, and equation-4.10 is used to calculate the equivalent continuum permeability of the reservoir using the built-in programming language FISH in FLAC3D, and isotropic permeability is assumed in the reservoir. **Figure-5.5, 5.6 & 5.7** show the tensile change, shear change in aperture and permeability, respectively, after 10, 20, 30, and 40 hours of injection with constant injection rate of 0.06 l/m/s.

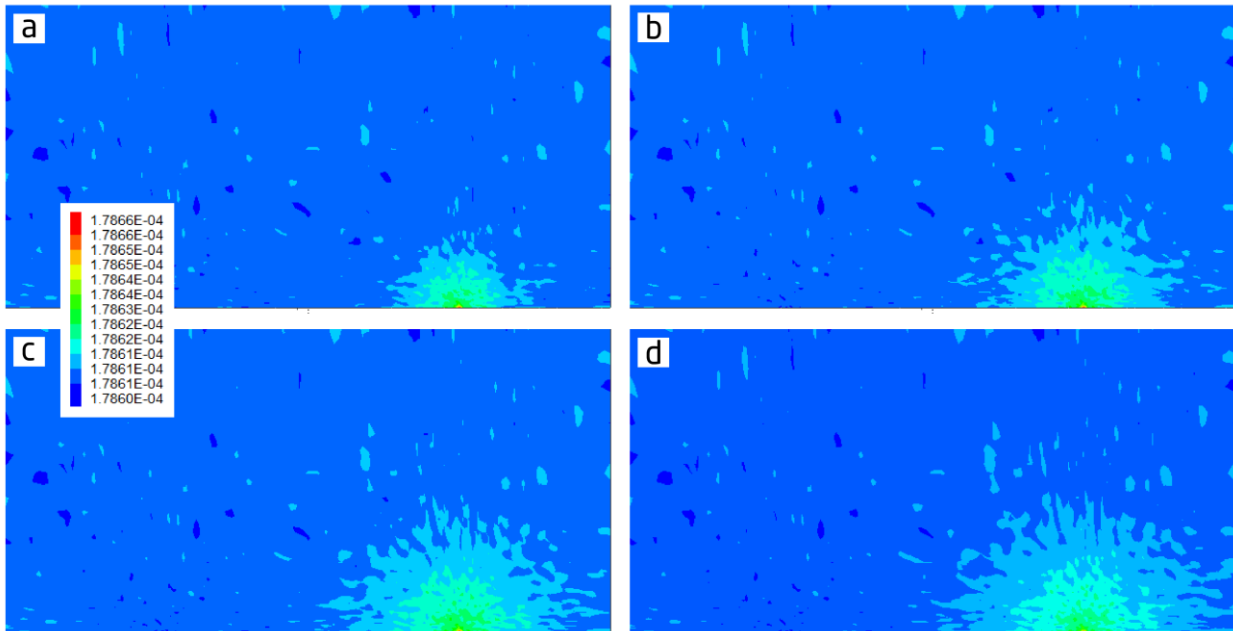


Figure-5.5: Tensile change of fracture aperture after (a) 10 hour, (b) 20 hours, (c) 30 hours & (d) 40 hours

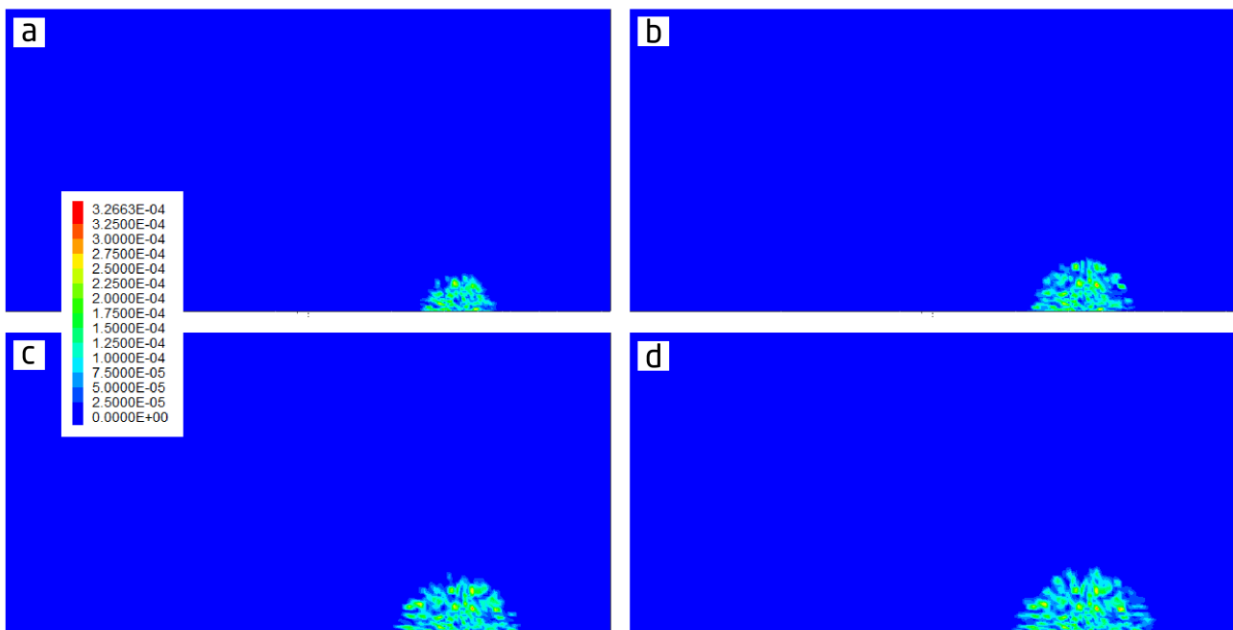


Figure-5.6: Shear stimulation of fracture aperture after (a) 10 hour, (b) 20 hours, (c) 30 hours & (d) 40 hours

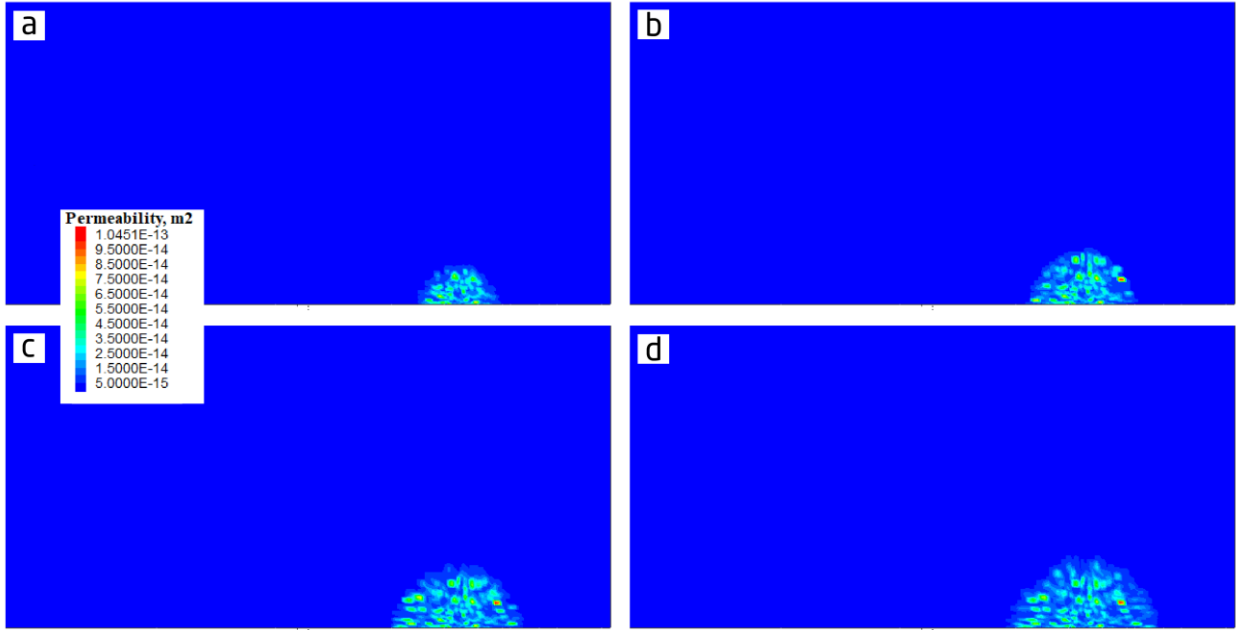


Figure-5. 7: Permeability evolution after (a) 10 hour, (b) 20 hours, (c) 30 hours & (d) 40 hours.

5.5 Elastic Moduli

Poroelastic effect results in change of vertical normal stress associated with the change in pore pressure. This change is described by the relation:

$$\Delta\sigma'_v = -\alpha\Delta P \quad (5.2)$$

where α is Biot's coefficient and its value ranges between 0 to 1. For laterally constrained reservoir, i.e., uniaxial strain conditions, pore pressure change results in horizontal stress perturbation described by the following relation (Mulders et al. 2003):

$$\Delta\sigma'_h = -(\alpha - \gamma_h)\Delta P \quad (5.3)$$

where $\gamma_h = \alpha\left(\frac{1-2\nu}{1-\nu}\right)$ is the horizontal stress path coefficient, and ν is Poisson's ratio. By using the relation between elastic moduli we can express Poisson's ratio in terms of the bulk and shear moduli which are used in initializing our model:

$$\nu = \frac{3-2\frac{G}{K}}{2(3-\frac{G}{K})}. \quad (5.4)$$

The change in effective normal stress is higher than the change in horizontal stress. Furthermore, the stress path coefficient controls whether slip along faults initiates. For example, it is noticed that in normal faulting regimes, with large stress path coefficient, pore pressure increase by injection can be stabilizing, while pore pressure decrease (i.e., production) may result in fault reactivation through enlarging Mohr circle of stresses (Mulders et al. 2003).

Number of simulations using different bulk and shear moduli shows how the poroelastic stress changes with change of pore pressure. High values of shear modulus and low values of bulk modulus make the fractures stabilize during injection. **Figure-5.8** shows results for different K and G moduli values after 40 hours of injection with injection rate of 0.025 l/s/m.

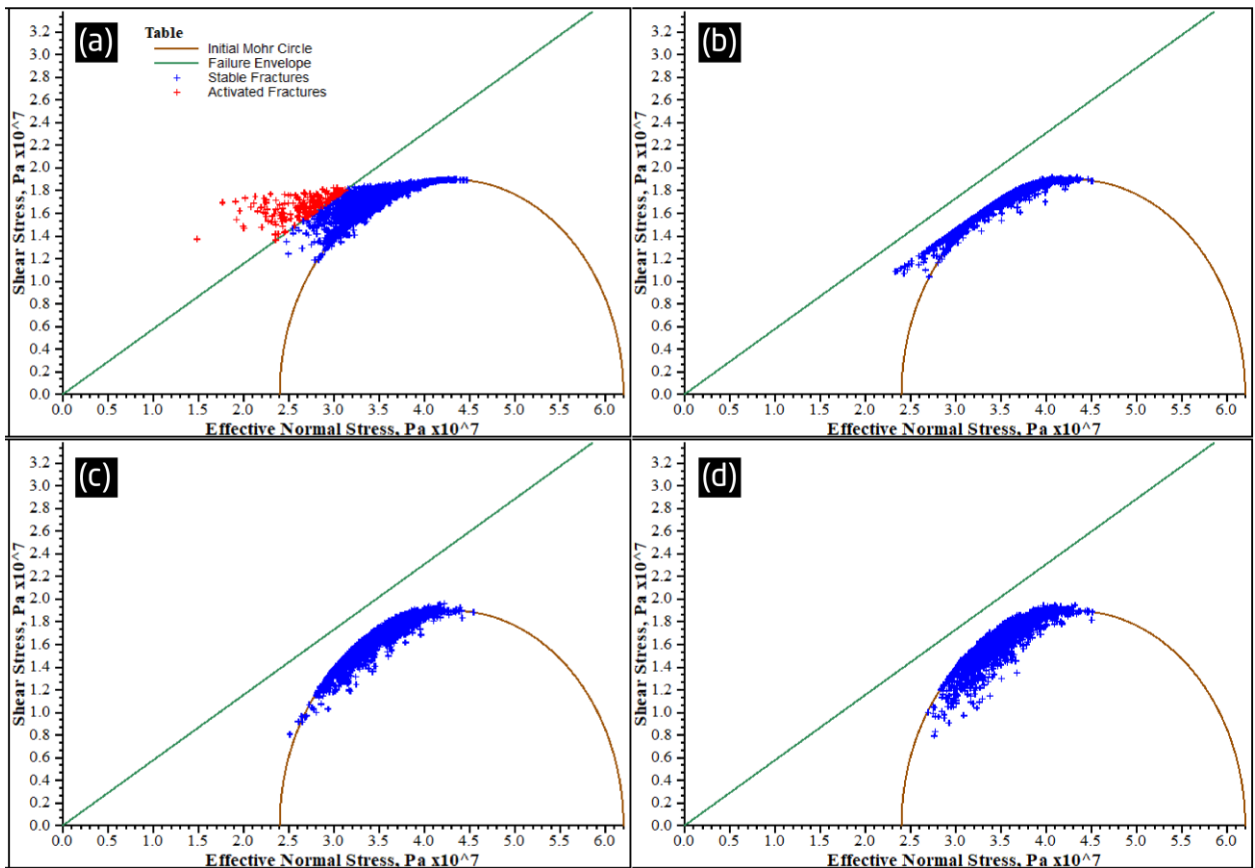


Figure-5.8: Poroelastic stress path for different Poisson's ratio ν after 40 hours of injection with injection rate of 0.025 l/s/m: (a) $\nu=0.49$ (b) $\nu=0.38$ (c) $\nu=0.25$ & (d) $\nu=0.115$ (Equation-5.4 used to calculate ν in terms of K & G)

Furthermore, a simulation run is carried out to model constant production rate from the reservoir using moduli values for case (d) in **Figure-5.8**, and found that production and pressure depletion will initiate slip along fractures (**Figure-5.9**). This behavior is similar to the case of the Dutch gas fields where pressure depletion due to production result in activating the existing faults and inducing seismic events (Van Wees et al. 2017).

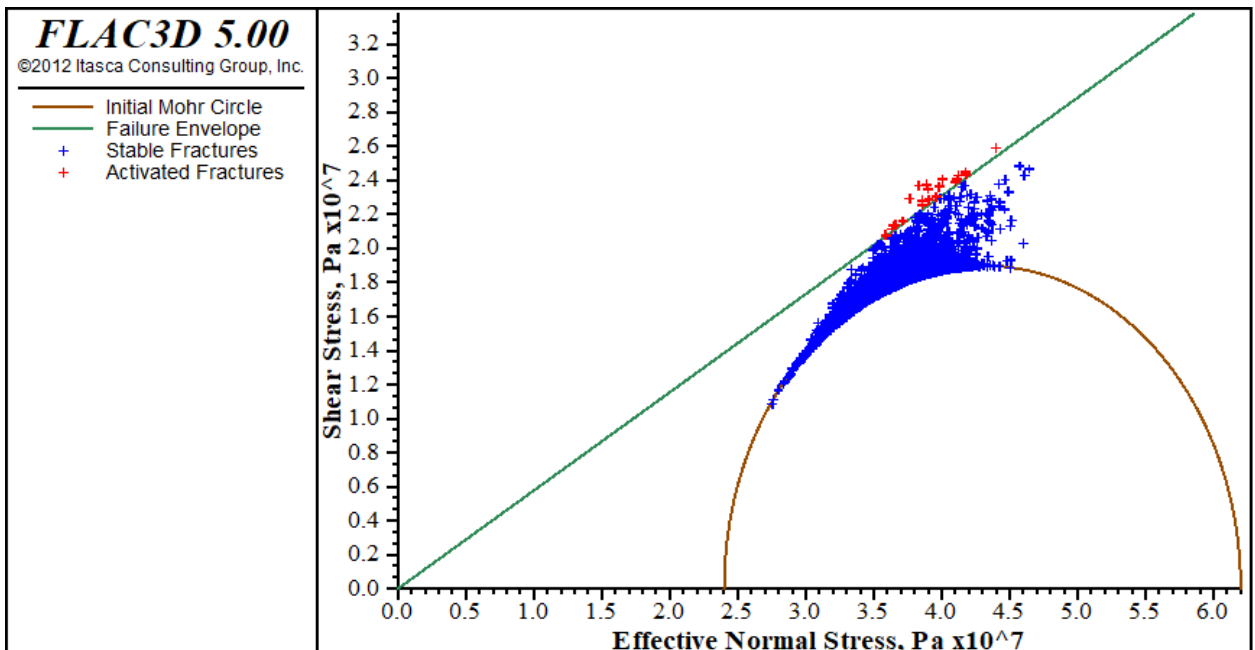


Figure-5.9: Poroelastic stress path for $\nu=0.115$ after 40 hours of production with production rate of 0.025 l/m/s.

Poisson's ratio affects the poroelastic stress path taken by the least horizontal stress. The simulated cases showed that injection may result in stabilizing or destabilizing the fractures depending on the Poisson's ratio, and hence, the poroelastic stress coefficient value. **Figure-5.10** is an illustration of how the stress path coefficient could change faults and fractures behavior in response to pore pressure change.

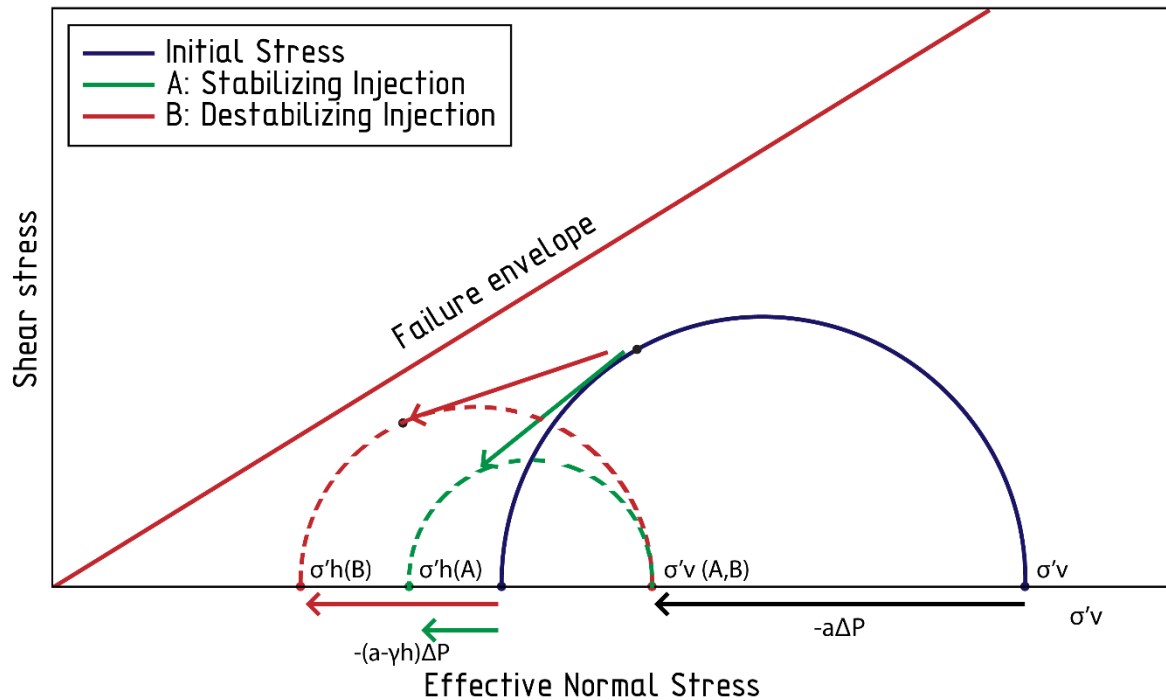


Figure-5. 10: Poroelastic stress path during injection in permeable reservoir (A) stress path diverges from failure envelope: Stabilizing during injection and (B) stress path converges onto failure envelope: Destabilizing during injection.

5.6 Effect of Injection Rate, Cyclic & Continuous Injection

Pore pressure build-up, and hence stress state perturbation, increases with increasing injection rate. Different injection rates are simulated to study the time at which events first occur, and the density of events in the seismic cloud. With low injection rates (0.001-0.007 l/s/m), no seismic events occurred, and as the injection rate increases, events start to occur earlier in time with increasing number of events with the continuation of the injection operation. **Figure-5.11** shows that earthquakes occurred after 9 hours from the start of injecting 0.01 l/s/m within 26 meters from the injection well. While it took only 30 minutes for earthquakes to occur with 0.03 l/s/m, and events occurred at distances up to 100 meters from the injection point. These results are in agreement with field observations, e.g., the Geysers geothermal field in California (Majer et al. 2007)

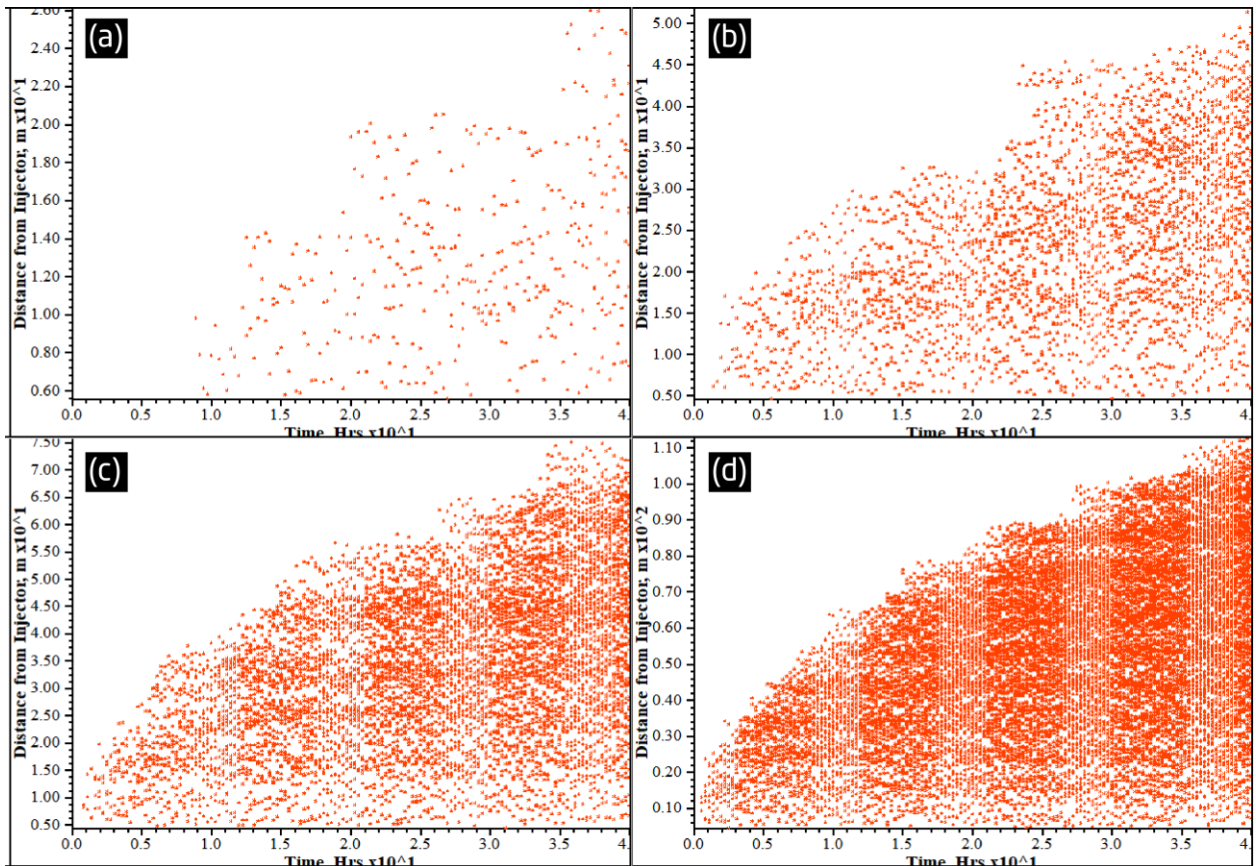


Figure-5. 11: Effect of injection rate on the induced seismic cloud: (a) 0.01 l/s/m, (b) 0.015 l/s/m, (c) 0.02 l/s/m, & (d) 0.03 l/m/s

Furthermore, different scenarios of continuous and cyclic injection are simulated to examine various operating procedures to control and mitigate seismic events. Both rate- and pressure-controlled injection scenarios are used. Scenarios required to inject a given volume of fluid into the reservoir are compared.

Rate-controlled injection is simulated to inject total volume of 1125 l/m in 90 hours where both continuous and cyclic injection scenarios are modelled. First scenario is a continuous injection of 0.0125 l/m/s and second scenario is cyclic injection with 0.025 l/m/s and injection/shut-in step of 10 hours. Down hole injection pressure in continuous-injection scenario rises to a maximum value of 52.79 MPa, while it rises to 60.65 MPa in cyclic-injection scenario.

Results show that high injection rate during cyclic injection produces seismic events at larger distances from the injection point. Also, seismic events occur after shut-in while their number decreases and eventually disappear after few hours. Continuous injection produces seismic events within smaller radius from the injection point, but the fractures are prone to continuous slip (could be seismic slip or aseismic creep). I did not find clear evidence that cyclic injection mitigates induced seismicity compared to continuous injection into naturally fractured reservoirs. These results are in agreement with results found by Yoon et al. (2014). Simulations results are in **Figure-5.12 & 13**

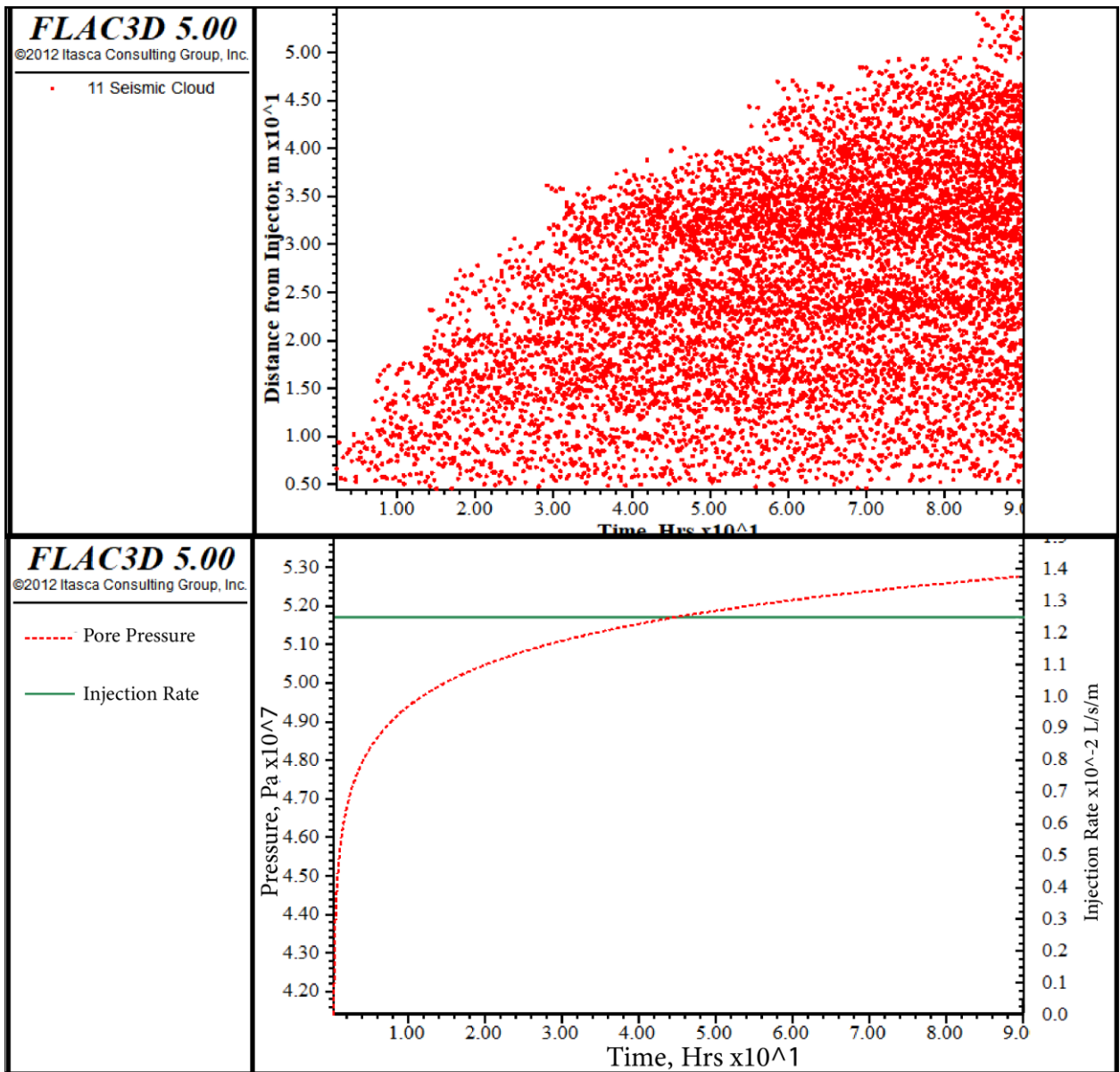


Figure-5.12: Continuous injection with 0.02 l/m/s.: (Top) Seismic events evolution, (Bottom) Injection rate and pressure.

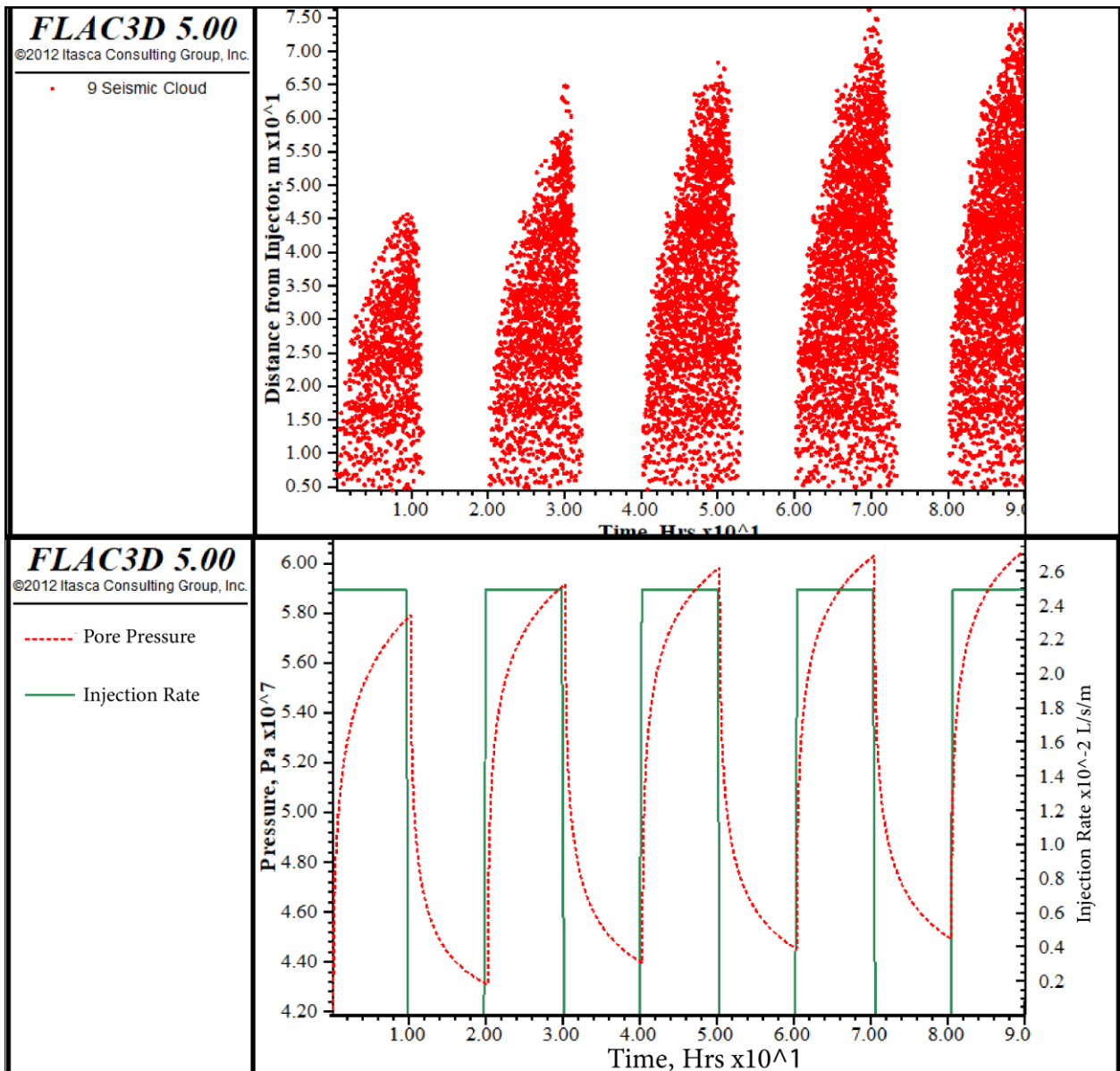


Figure-5.13: Cyclic injection with 0.04 l/m/s; (Top) Seismic events evolution, (Bottom) Injection rate and pressure.

Furthermore, step rate scenario and the equivalent continuous rate are simulated to inject a total volume of 3240 l/m (Figure-5.14 & 15). Similar observations as in cyclic injection were *also* noticed in the step rate scenario. Higher rates in step rate scenario produced seismic events at larger distances from the injection point. Also, seismic events occurred after shut-in while their number decreases and eventually disappear after few hours.

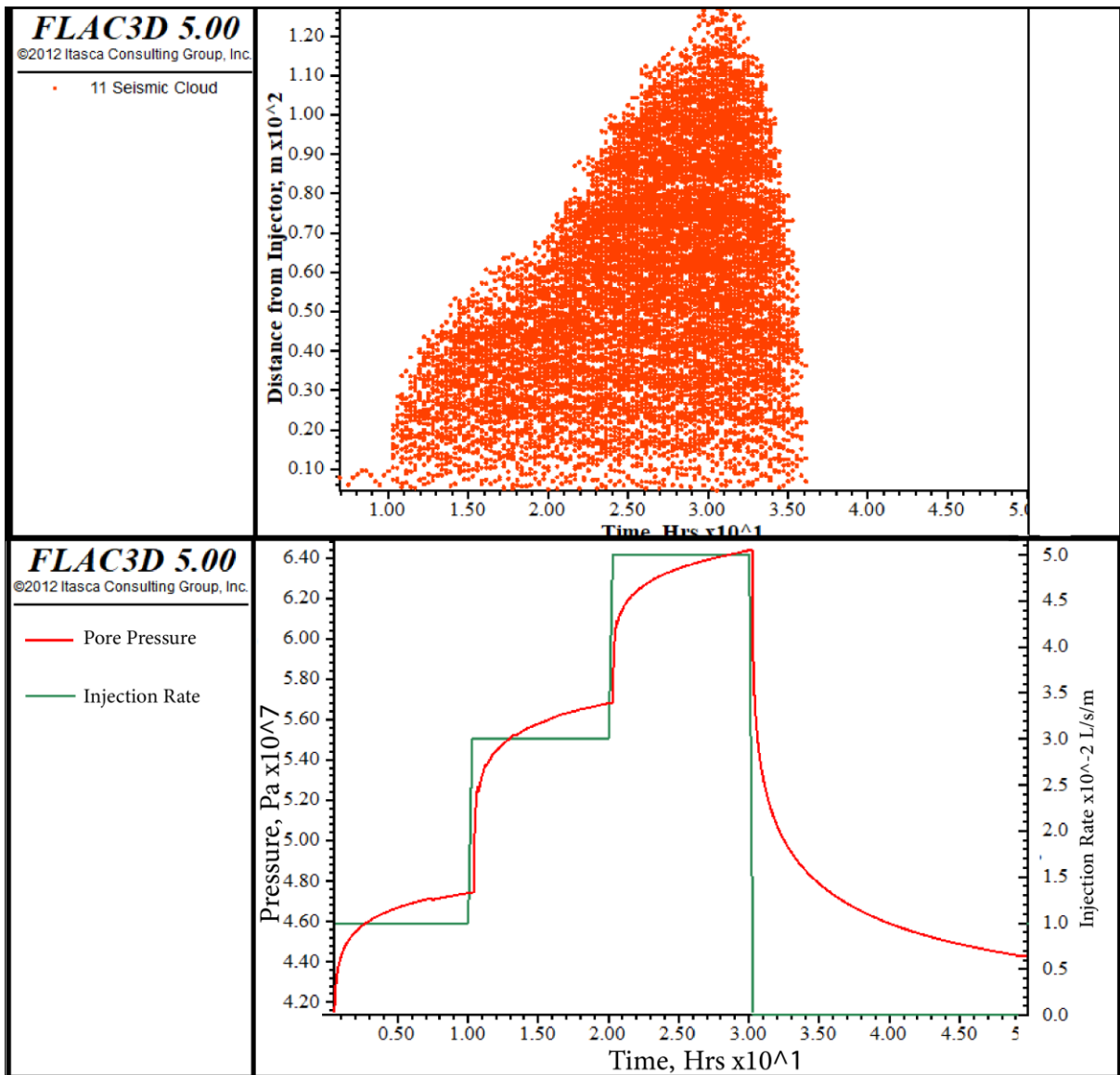


Figure-5. 14: Step rate scenario: (Top) Seismic events evolution, (Bottom) Injection rate and pressure.

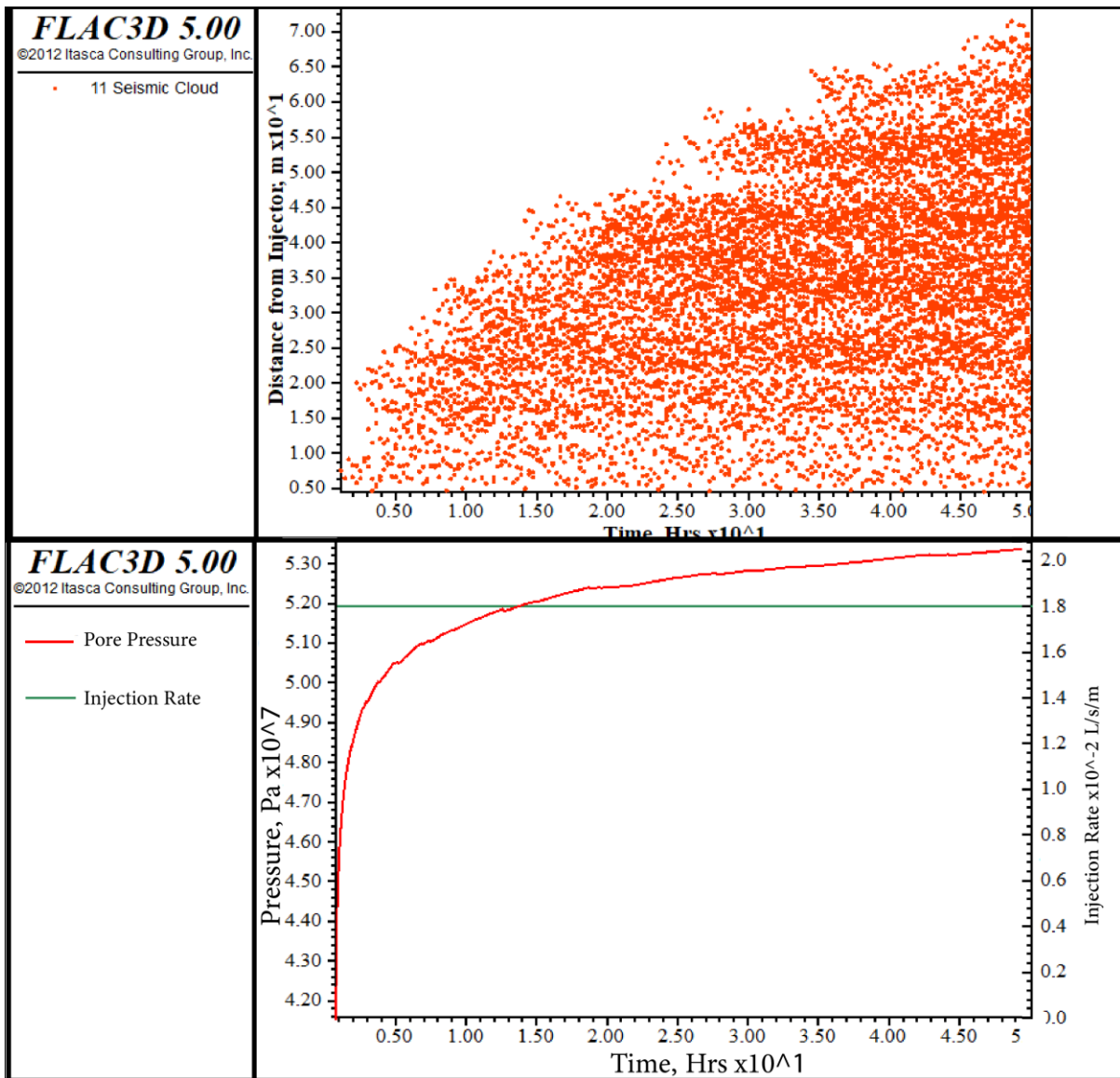


Figure-5. 15: Continuous rate equivalent to the simulated step-rate scenario (0.018 l/s/m): (Top) Seismic events evolution, (Bottom) Injection rate and pressure.

Pressure-controlled injection using down-hole injection pressure below seismicity onset results in no seismic events, however, this usually implies low injection rates especially in case of low permeability. **Figure-5.16** shows results for two different injection pressures.

Putting restrictions on the down hole injection pressure to keep the pore pressure below seismicity onset is a key factor to prevent or mitigate seismic events. For example, keeping the pressure below the critical pressure for fracture activation (around 47.5 MPa) prevents seismicity occurrence in **Figure-5.16** (bottom).

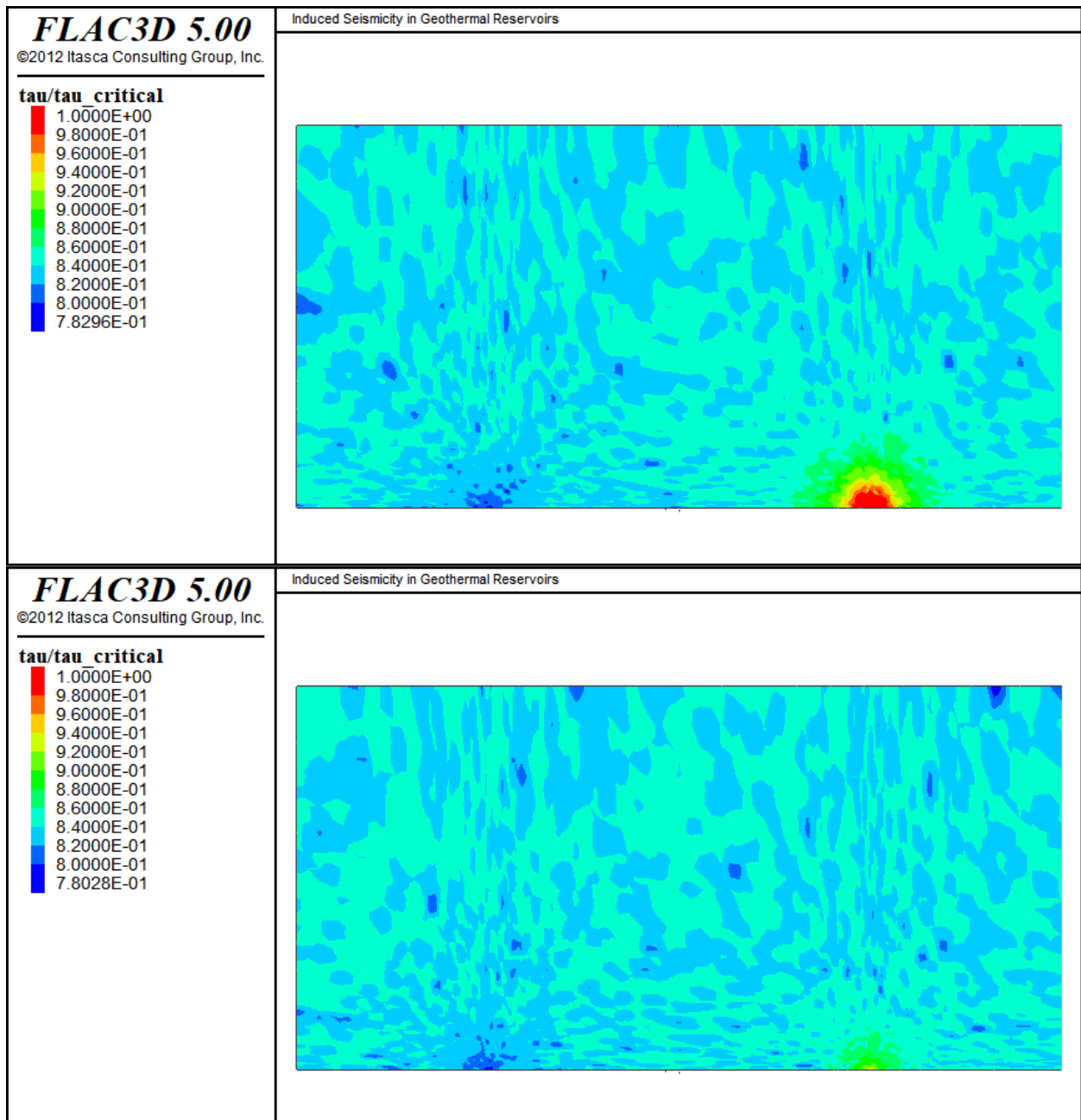


Figure-5.16: Evolution of slip and seismic events during 60 MPa injection pressure-higher than the seismicity onset (top), and 46 MPa injection pressure-lower than seismicity onset (bottom).

5.6 Role of Intermediate Stress

A number of simulations were carried out to investigate the role of intermediate stress on the slip of the pre-existing fractures by setting $\sigma_y = \sigma_x$ and $\sigma_y = \sigma_z$. From **Figure-5.17** it is noticed that there is no significant difference in the evolution of seismic events between the two intermediate-stress values. Intermediate stress has been long accepted not to affect the slip along existing fractures and faults planes, however, it may affect the failure of intact rock (Hackston 2013).

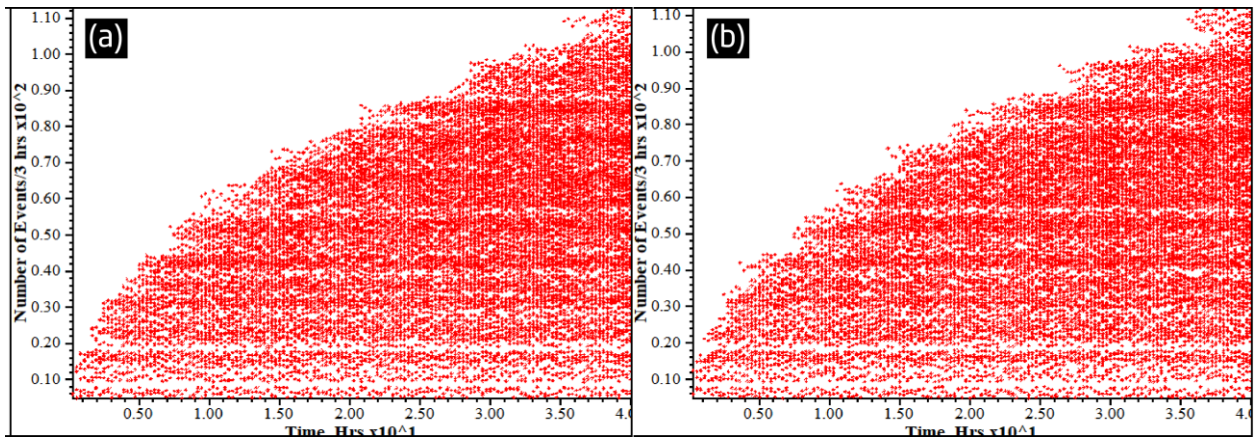


Figure-5.17:: Seismic events evolution when (a) $\sigma_y=\sigma_x$ (b) $\sigma_y=\sigma_z$ (injection rate is 0.03 l/m/s)

5.7 Differential Stress

Simulations using two different differential stress values ($\sigma_{max}-\sigma_{min}$) were conducted using the same injection rate. I found that the differential stress has a critical role in initiating slip and triggering seismic events (**Figure-5.18**). As the differential stress increases, it brings fractures closer to the critical state and facilitates failure, so fractures under large differential stress need smaller pore pressure perturbation to slip compared to fractures under lower differential stress.

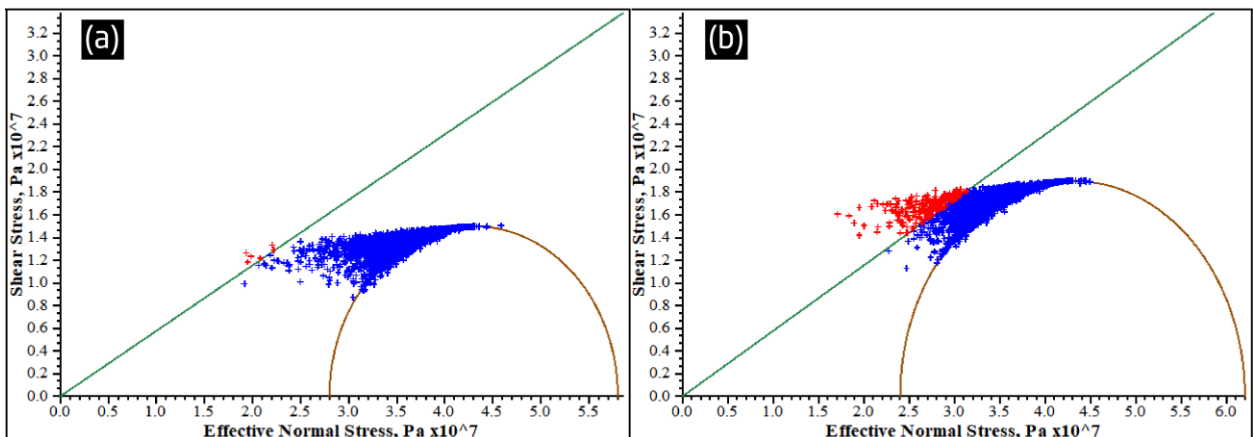


Figure-5.18: Effect of differential stress on fractures status after 40 hours of continuous injection: (A) 30 MPa differential stress (B) 38 MPa differential stress. (Constant injection rate of 0.03 l/m/s is used in producing these results).

CHAPTER 6: Fault Frictional Behavior

6.1 Introduction

Faults and joints stability is a critical aspect of many underground engineering projects from the safety of underground mines to the integrity of underground gas storages and controlling induced seismicity. In this chapter, the stability of a decametric-scale fault is studied using rate-and-state frictional theory to investigate the effect of injection rate and the different parameters affecting the frictional resistance along the fault. This chapter starts with a description of the model dimensions, and the initial and boundary conditions. Then, a brief description of the slip-dependent, and rate-dependent relations to account for friction evolution along the fault.

In the previous model (Chapter-4 & 5), seismicity cloud is studied on a large scale imitating large portion of a reservoir. However, rupture attributes (e.g., slip, slip-rate, seismic magnitude) are not studied as the fractures are simulated as "seed points" representing potential earthquakes hypocenters, and their triggering is studied in temporal and spatial domain in response to pressure diffusion and the associated stress-field perturbation. In this chapter, rupture attributes are studied in a detailed manner by adopting a decametric-scale single fault model.

FLAC 3D is used here to solve for the co-seismic slip and rupture propagation. Evaluating the co-seismic solution is a difficult process as there is no available analytical solution to examine the numerical results. In the last few years, efforts have been made to compare numerical codes related to earthquake modelling and a number of benchmark tests have been set by the South California Earthquake Center (SCEC) consortium. FLAC has been one of the verified codes against benchmark tests. The results show good agreement of FLAC with other codes to reproduce the dynamic fault rupture with slip-weakening friction behavior (Harris et al. 2009).

Simulations in this chapter consist of: first, sensitivity analyses of different injection rates using slip weakening and velocity-neutral behavior to study the effect of the rate on the fault parameters including rupture, slip, slip-rate. Second, by applying constant injection rate, different scenarios of slip- & rate-dependent relations are examined. Finally, using constant injection rate, characteristic slip distance value is studied through different values to investigate its role in fault behavior.

6.2 Model Description:

The fault has dipping length of 80 m and width of 70 m imbedded in an elastic medium (70 m \times 70 m \times 70 m) (**Figure-6.1**). In FLAC3D, fault is represented by an "interface" object which consists of a number of triangular elements defined by three nodes each (a node at each vertex). Input parameters are assigned, and outputs are calculated at these nodes (**Figure-6.2**).

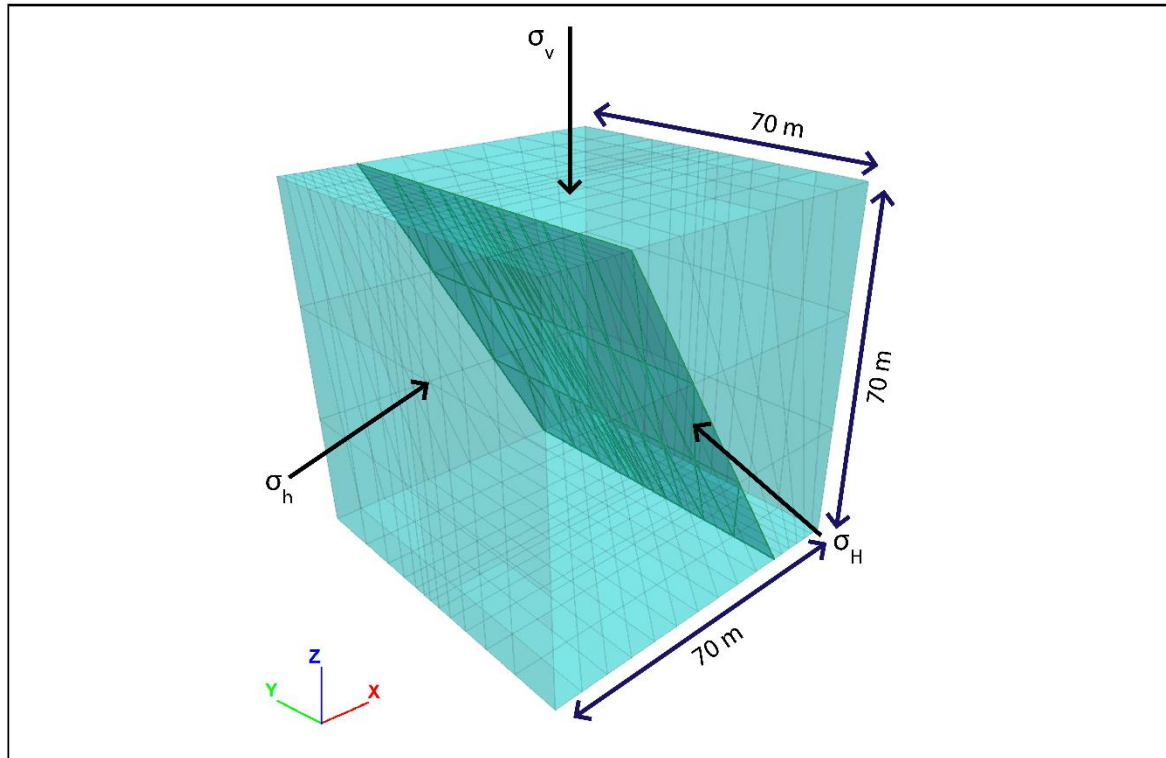


Figure-6. 1: Fault model used in the simulations.

For simplicity, fault initial hydraulic, thermal and mechanical properties are considered homogeneous. Normal stress regime is applied where the vertical overburden is the maximum principal stress, and equals to the overburden stress at 4 km depth. The minimum and maximum horizontal stresses are chosen to be ≈ 0.61 and 0.83 of the vertical stress, respectively. Initial fluid pressure equals to the hydrostatic pressure at 4 km depth. Displacement perpendicular to the side and bottom boundaries is constrained, and it is allowed only at the upper boundary. This resembles a uniaxial strain conditions (Engelder and Fischer 1994). **Table-6.1** summarizes the parameters used in the simulations.

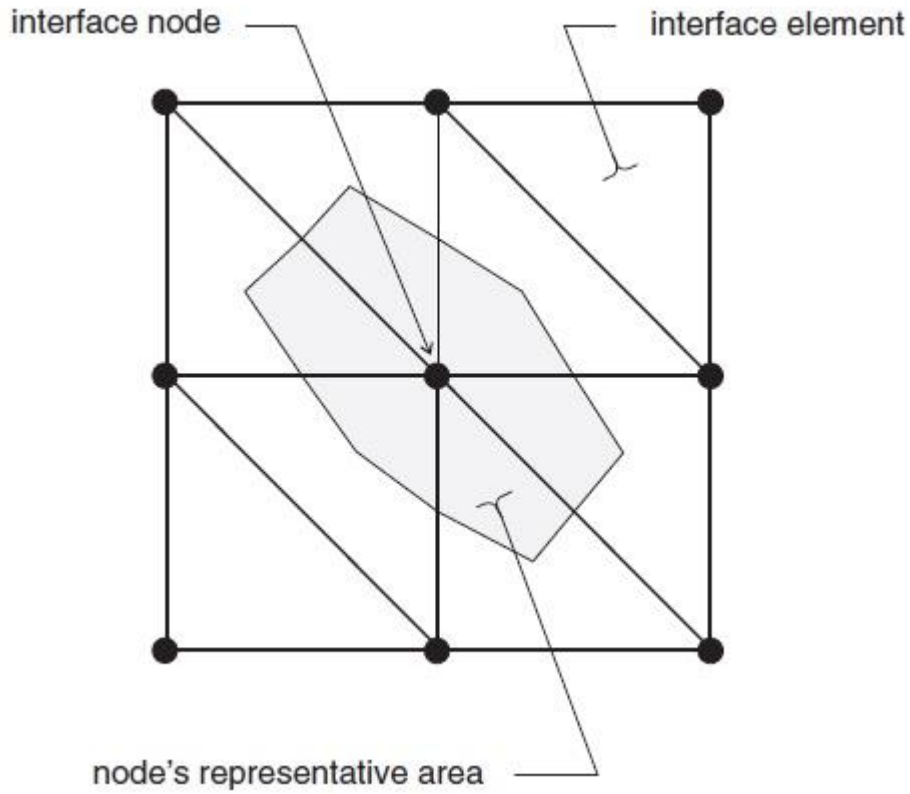


Figure-6. 2: Interface structure in FLAC3D (Itasca FLAC3D Documentations).

| Parameter | Value | Unit |
|-----------------------------------|---|-------------------|
| Stress in z-direction, σ_z | 103 | MPa |
| Stress in y-direction, σ_y | 85 | MPa |
| Stress in x-direction, σ_x | 63 | MPa |
| Bulk Modulus, K | 35 | GPa |
| Shear Modulus, G | 2 | GPa |
| Biot's Coefficient, α | 1 | |
| Water Bulk Modulus, K_w | 2 | GPa |
| Rock Density, ρ_m | 2700 | kg/m ³ |
| Water Density, ρ_w | 1000 | kg/m ³ |
| Permeability, k | 1e-15 | m ² |
| Water Viscosity μ | 0.1 | c.p |
| Initial Pore Pressure, p_0 | 42.5 | MPa |
| Well Radius, r_w | 0.3 | m |
| Porosity, ϕ | 0.07 | |
| Injection Rate, q | 0.06 (0.03 & 0.09 for sensitivity analyses) | l/m/s* |
| Joint Cohesion, C_f | 0 (Cohesionless) | MPa |

Table-6. 1: Parameters used in simulations.

Shear and effective normal stress evolve as a function of the shear displacement along the fault. Effective normal stress decrease is controlled by fluid pressure increase along the fault. Normal and shear stresses at each node of the interface is calculated where force magnitudes are calculated from the stress acting on each element of the fault interface. Mohr-Coulomb criterion calculates a maximum admissible value for shear force F_{Smax} :

$$F_{Smax} = C * A + \mu(F_n - pA)$$

where C is the cohesion of the interface, A is the area of the contact of the node, μ is the friction coefficient (it varies with shear displacement and slipping velocity), F_n is the normal force. p is the pore pressure. Before failure, there is continuity in both shear and normal displacement, while during shearing only normal displacement will be continuous (non-penetrating surface).

Rate-and-state theory is employed to simulate the frictional strength evolution during slip, a slip-weakening and velocity-weakening/strengthening laws are applied. Frictional resistance decreases over a critical slip distance $2.0e-5$ m until it reaches the steady-state slipping with dynamic friction coefficient of 0.404 (corresponding to a friction angle of 22).

Friction drops since the start of the rupture process according to slip-weakening relation from the static value of 0.577 linearly with the slip to dynamic friction of 0.404 at the characteristic slip distance (Urpi et al. 2016):

$$\mu = \mu_D + \left(1 + \frac{L}{L_C}\right)(\mu_S - \mu_D) \quad L \leq L_C$$

Once the characteristic slip is reached, friction coefficient evolves depending on the slipping velocity with (a-b) parameter controlling whether the slip is velocity-weakening or – strengthening (Urpi et al. 2016):

$$\mu = \mu_D + (a - b) \ln \frac{V}{V_0} \quad L > L_C \text{ \& } V > V_0$$

Positive values of (a-b) represents velocity-strengthening regime while negative values represent velocity-weakening regime. V_0 is a reference velocity (taken here to be $7 * 10^{-9} m/s$). If $V \leq V_0$ the friction coefficient is set to the dynamic friction value μ_D . Velocity-neutral behavior is defined when a-b=0. In the latter case, friction remains constant at the dynamic value after rupture. **Figure-6.5** is an illustration of how the friction coefficient evolves with slip in a slip-weakening relation.

In the simulations, water is injected in the upper 20 m perforated interval of the modelled medium. Fault is initially critically stressed, so it is expected to rupture within few minutes from the start of injection with the proposed injection rates. Different parameters, including slip velocities and magnitudes and shear stress are monitored at different positions along the fault plane.

6.3 Results

Parametric analyses for three different injection rates are performed using slip-weakening approach (a-b=0). The failure onset differs for each rate and the resulting displacement and event magnitude also changes with injection rate.

For the analysis of frictional evolution scenarios, constant injection rate of 0.06 l/s/m is assumed. With continuous injection of such rate into the fault zone under the conditions described by the parameters in **Table-6.1**, stress field perturbations cause spontaneous rupture of the fault after 82 seconds, for an overpressure at the injection well of about 4.7 MPa. By measuring the pressure at the top of fault (closest point to the injection well), it is found that

failure occurs at overpressure of about 0.15 MPa, and this is in agreement with the analytical solution of the Mohr-Coulomb criterion (**Figure-6.3**).

Nucleation zone or the start of an earthquake is defined as the area where the shear stress exceeds the maximum allowable shear given by the Mohr-Coulomb criterion (Urpi et al. 2016). Although, final rupture area can be higher than the actual nucleation area due to stress transfer effect. Slip occurs repeatedly along the fault during injection, with a decreasing incremental slip magnitude because of the relieved shear stresses during rupture.

Parametric analyses have been performed to study the seismic events, slip, and slip rate along the fault plane for different (a-b) values ranging from -0.01 to +0.01 to study the velocity-weakening and velocity-strengthening slip, also velocity-neutral slipping is studied by setting the value of parameter (a-b) to zero. Furthermore, different values of the characteristic slip distance are used to study its effect on the evolution of rupture along the fault.

The seismic moments M_0 and the moment magnitudes M_w were calculated from the shear displacement in every failing node on the fault interface (Hanks & Kanamori 1979). They are given by: $M_0 = G \cdot A \cdot L$, and $M_w = \frac{2}{3} \log M_0 - 6.07$ (Kanamori & Anderson 1975) in which G is the shear modulus, A the joint area that is failing, , and L the shear displacement. The seismicity of all failing node areas along the fault interface at a given moment are summed to get meaningful events data.

Maximum slip distance, the magnitude of the resulting event, and minimum shear stress for the first rupture event will be compared for different regimes to study the effect of each parameter affecting the frictional strength of the fault. For a $M=3.0$ event, which can be felt at the surface, an area of 6700 m^2 must slip a distance of 30 cm. Only microseismic events are expected from the model discussed here due to its limited size. Last parametric analysis is simulation runs of different characteristic slip distance values, which shows important role of this parameter in controlling the behavior of the fault during injection operation.

6.3.1 Flow Rate

Slip-weakening regime (velocity-neutral) is used to study the effect of injection rate on the timing of slip and slip magnitude. Friction decreases linearly with shear displacement from the static value of 0.577 to its dynamic value of 0.404 when the characteristic slip distance of $2 * 10^{-5} \text{ m}$ is reached. Run time is set to 600 seconds and slip magnitude and events magnitudes are monitored. Results show earlier failure and higher slip rate in case of higher injection rates. Furthermore, slip magnitudes increased with injection rate and hence, the resulted event magnitudes. Results are summarized in **Table-6.2**.

| Rate, l/s/m | Max. Slip, mm | Max. Mw | Time of first rupture, s | Slip Rate, m/s |
|-------------|---------------|---------|--------------------------|----------------|
| 0.03 | 0.494 | -0.66 | 173 | 2.59e-6 |
| 0.06 | 0.496 | -0.63 | 82 | 5.98e-6 |
| 0.09 | 0.505 | -0.60 | 58 | 8.60e-6 |

Table-6. 2: Simulation results for different injection rates using slip-weakening scenario for frictional strength.

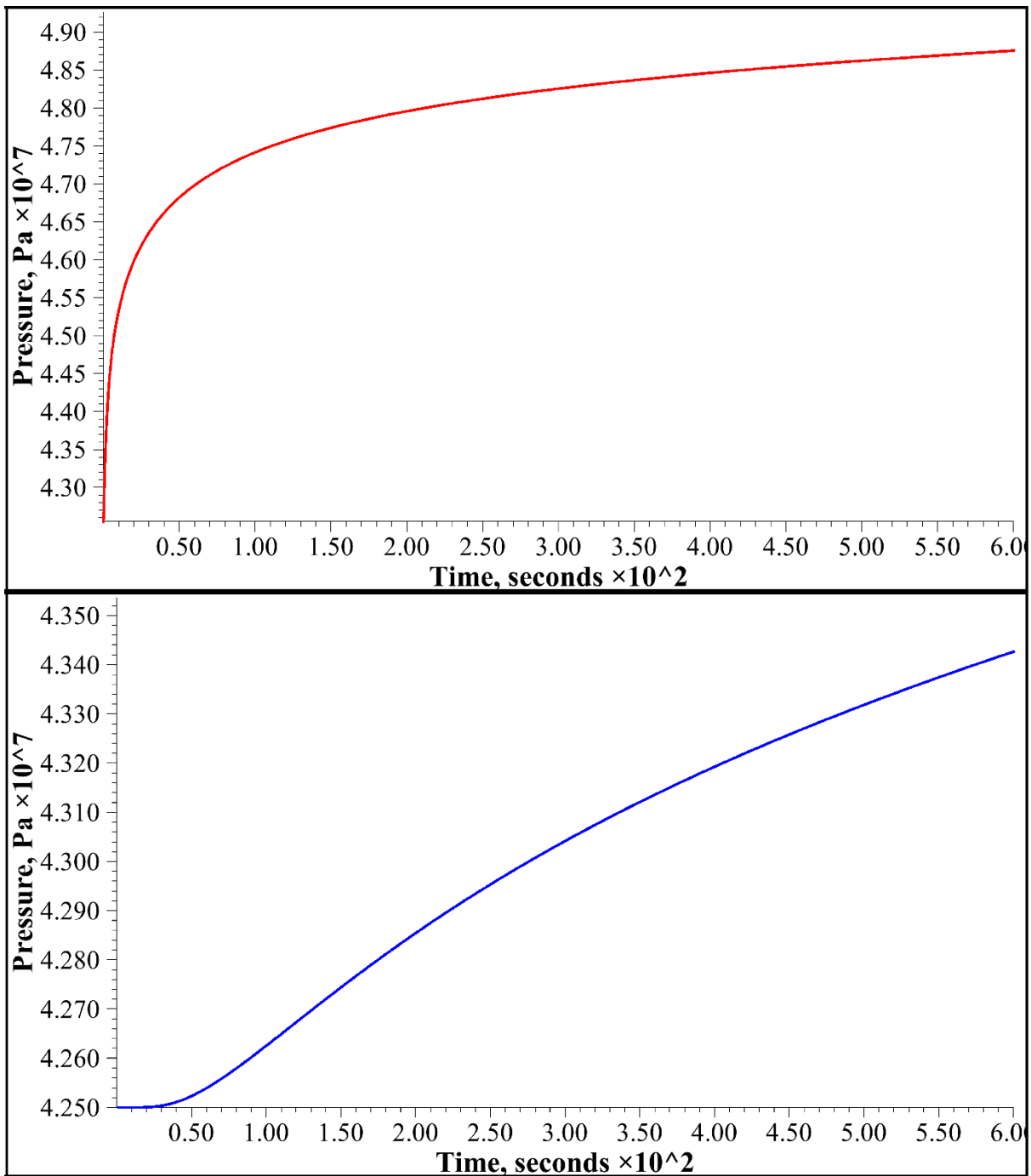


Figure-6. 3: (Top) Pore pressure at the injection point (bottom) pore pressure at the top of the fault.

Figure-6.4 shows pressure contours in the model after at the end of the simulation run, injection is applied at the upper 20 meters of the model.

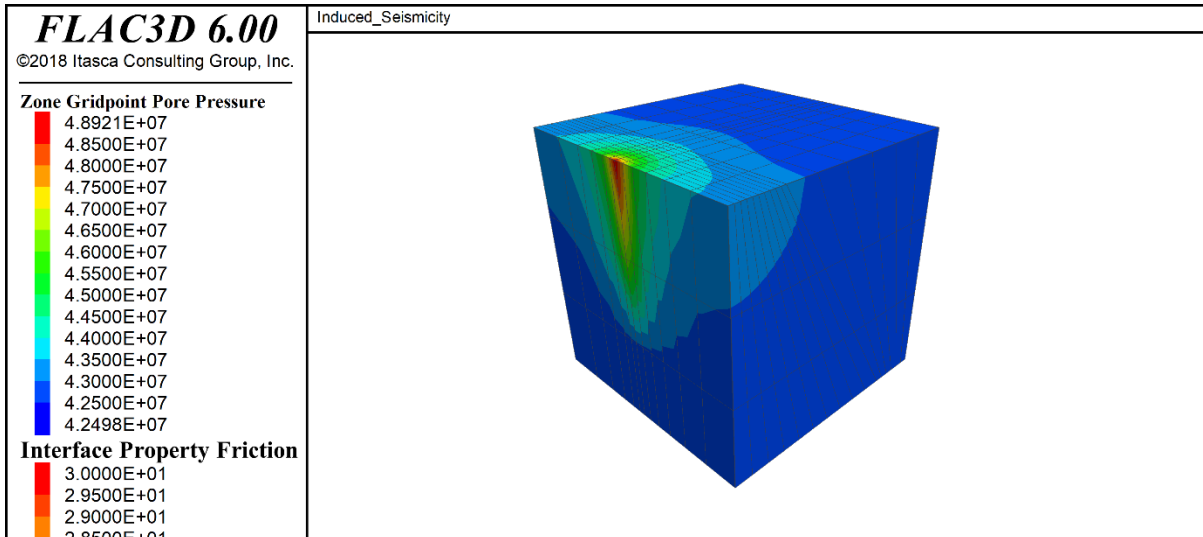


Figure-6. 4: Pore pressure contours at the end of the run with injection rate of 0.06 l/m/s (Other parameters found in Table-6.1)

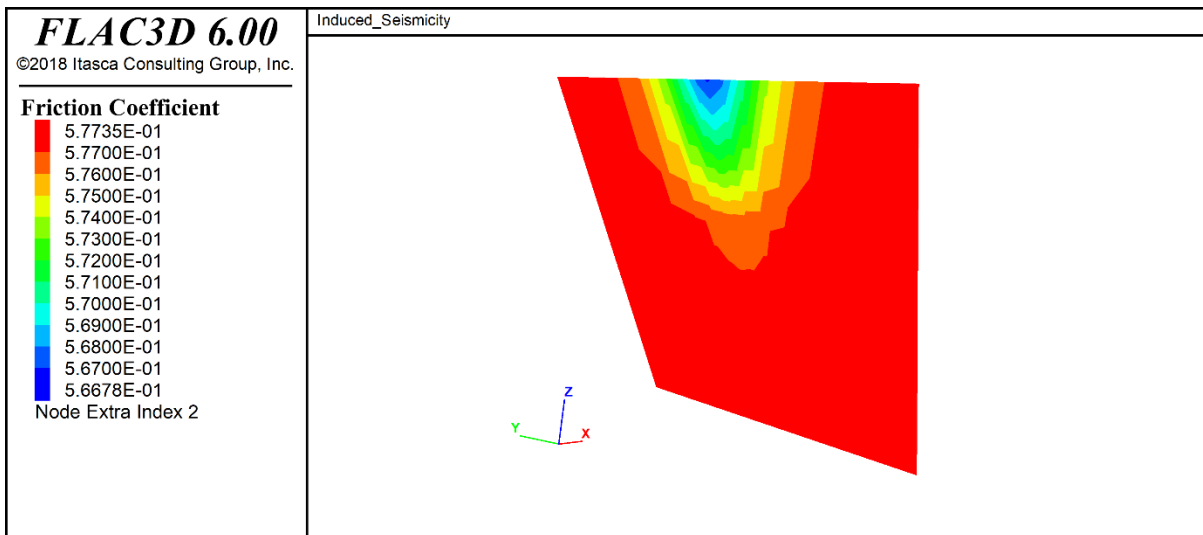


Figure-6. 5: Illustration of how the friction coefficient evolves with slip in a slip-weakening relation.

6.3.2 Velocity-neutral simulations

Simulation results for $a-b=0$ (velocity-neutral) show that shear stress increases slowly with the continuation of injection process until it reaches a peak value around 17.35 MPa at the moment of rupture then drops to a minimum value of 13.89 MPa before it starts to build up again with the continuation of injection. Shear stress outside the nucleation zone increases by a small increment at the moment of rupture due to stress transfer between the slipping part and the rest of the fault, the magnitude of this increase depends on the distance from the ruptured zone.

Friction coefficient evolves through time from its static value of 0.577 at the start of injection and decreases linearly with the increase of displacement until the critical slip distance is reached, then drops to 0.404 at rupture. Friction coefficient outside the nucleation zone also undergoes a small drop due to stress transfer which results in larger displacement at different locations along the fault which differs depending on its distance from the first nucleation zone. In velocity-neutral slipping regime, friction coefficient drops to a constant dynamic value after the rupture. Slip velocity jumped to 5.98×10^{-6} m/s at the moment of rupture. Values of slip velocities are of the same order of magnitude as noticed from field observations at different earthquake locations (Anderson et al. 1996).

6.3.3 Velocity-strengthening simulations

By setting the parameter (a-b) to +0.005 and +0.01 to study velocity-strengthening behavior, it is noticed that slip magnitude dropped compared with velocity-neutral, while the rupture area almost remained the same. Shear stress dropped from a maximum of 17.35 MPa before the rupture moment to minimum values of 14.31 and 14.35 MPa and, friction coefficient dropped to 0.414 & 0.4235, for the two (a-b) values, respectively. Furthermore, event magnitude decreased with increasing (a-b) parameter.

6.3.4 Velocity-weakening simulations

Velocity-weakening shows the largest slip and event magnitudes, while the rupture area almost remained the same. Shear stress dropped from a maximum of 17.35 MPa at the rupture moment to minimum values of 13.645 and 13.34 MPa and friction coefficient dropped to 0.389 & 0.374, for a-b=-0.005 & -0.01 respectively.

Table-6.3 shows the results for the different constitutive relation for frictional strength at the moment of rupture (time-step of one microsecond is used to calculate these parameters):

| | a-b | Max. slip, mm | Max. slip rate, m/s | Min. shear stress, MPa | Max. shear stress, MPa | Friction coefficient at rupture moment | First event magnitude Mw |
|------------------------|--------|---------------|---------------------|------------------------|------------------------|--|--------------------------|
| Velocity-neutral | 0 | 0.491 | 5.45e-6 | 13.89 | 17.35 | 0.404 | -0.68 |
| Velocity-strengthening | +0.005 | 0.455 | 5.10e-6 | 14.31 | 17.35 | 0.414 | -0.78 |
| | +0.01 | 0.425 | 4.95e-6 | 14.35 | 17.35 | 0.424 | -0.79 |
| Velocity-weakening | -0.005 | 0.527 | 6.40e-6 | 13.65 | 17.35 | 0.389 | -0.675 |
| | -0.01 | 0.562 | 6.85e-6 | 13.34 | 17.35 | 0.374 | -0.66 |

Table-6. 3: Results for different (a-b) values for different frictional evolution scenarios.

It can be also noticed from the simulation runs that under the same injection rate and with constant characteristic slip distance, the first nucleation zone ruptures at the same time for the different (a-b) values. However, this is not the case for the successive rupture events. This behavior is due to stress transfer and the associated slip at different parts of the fault outside first nucleation zone. Time between rupture at the top (first nucleation zone) and middle of fault ranges from 22 seconds with a-b=-0.01, to around 90 seconds with a-b=+0.01. **Figure-6.6** through **6.9** show friction evolution, slip, slip rate, and shear stress, respectively, for the different (a-b) values at two different locations along the fault.

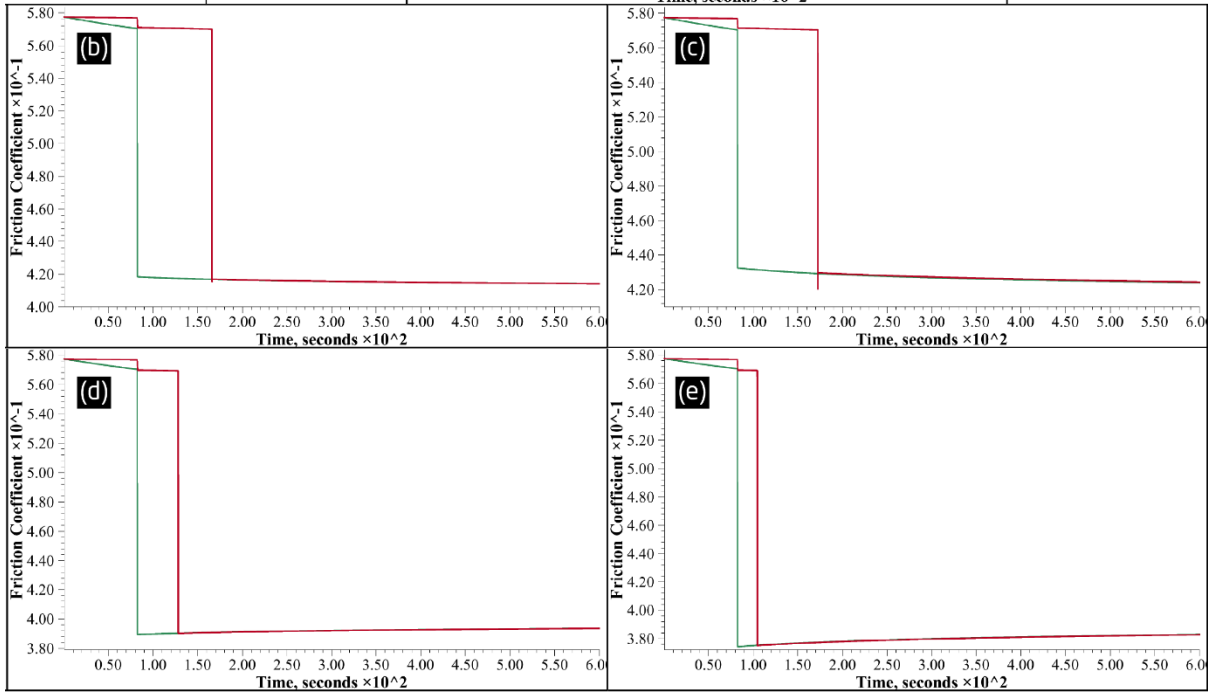
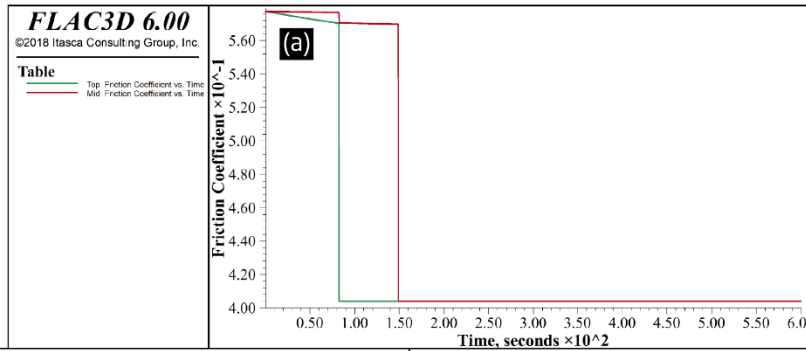


Figure-6. 6: Friction coefficient vs. time at two points along the fault (top and middle) for different $(a-b)$ values (a) $a-b=0$, (b) $a-b=+0.005$, (c) $a-b=+0.01$, (d) $a-b=-0.005$, & (e) $a-b=-0.01$.

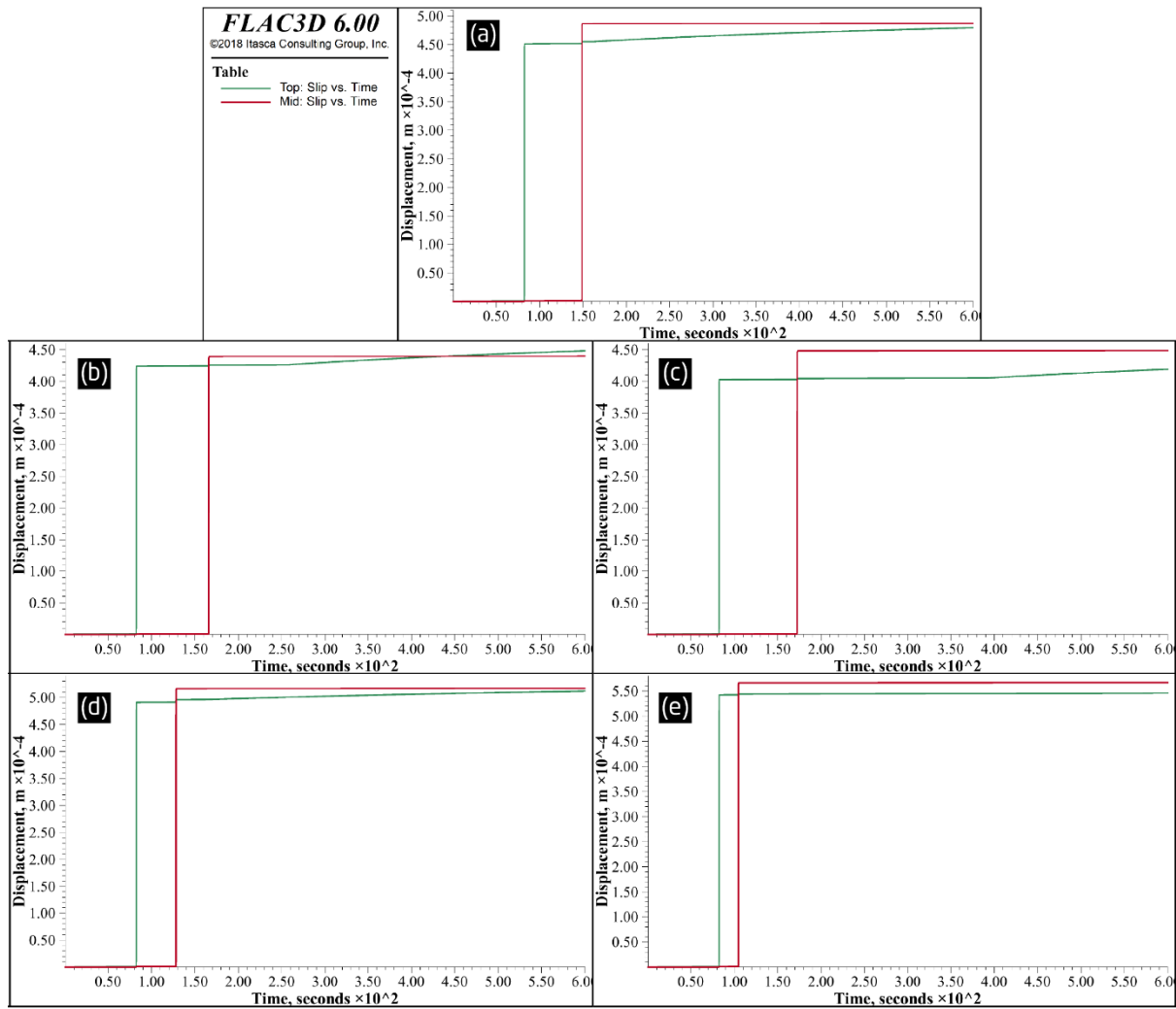


Figure-6. 7: Slip magnitude vs. time at two points along the fault (top and middle) for different $(a-b)$ values (a) $a-b=0$, (b) $a-b=+0.005$, (c) $a-b=+0.01$, (d) $a-b=-0.005$, & (e) $a-b=-0.01$.

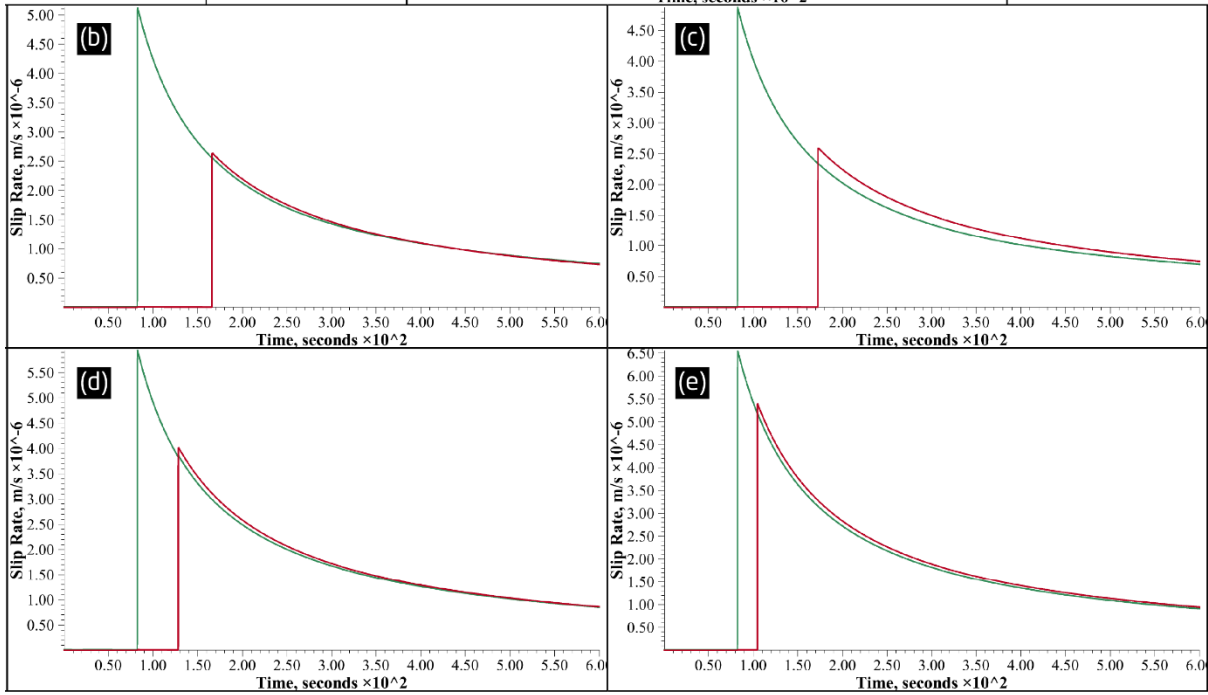
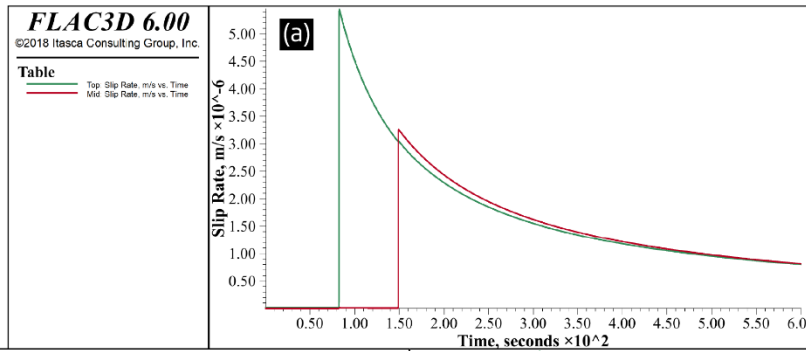


Figure-6. 8: Slip rate vs. time at two points along the fault (top and middle) for different $(a-b)$ values (a) $a-b=0$, (b) $a-b=+0.005$, (c) $a-b=+0.01$, (d) $a-b=-0.005$, & (e) $a-b=-0.01$.

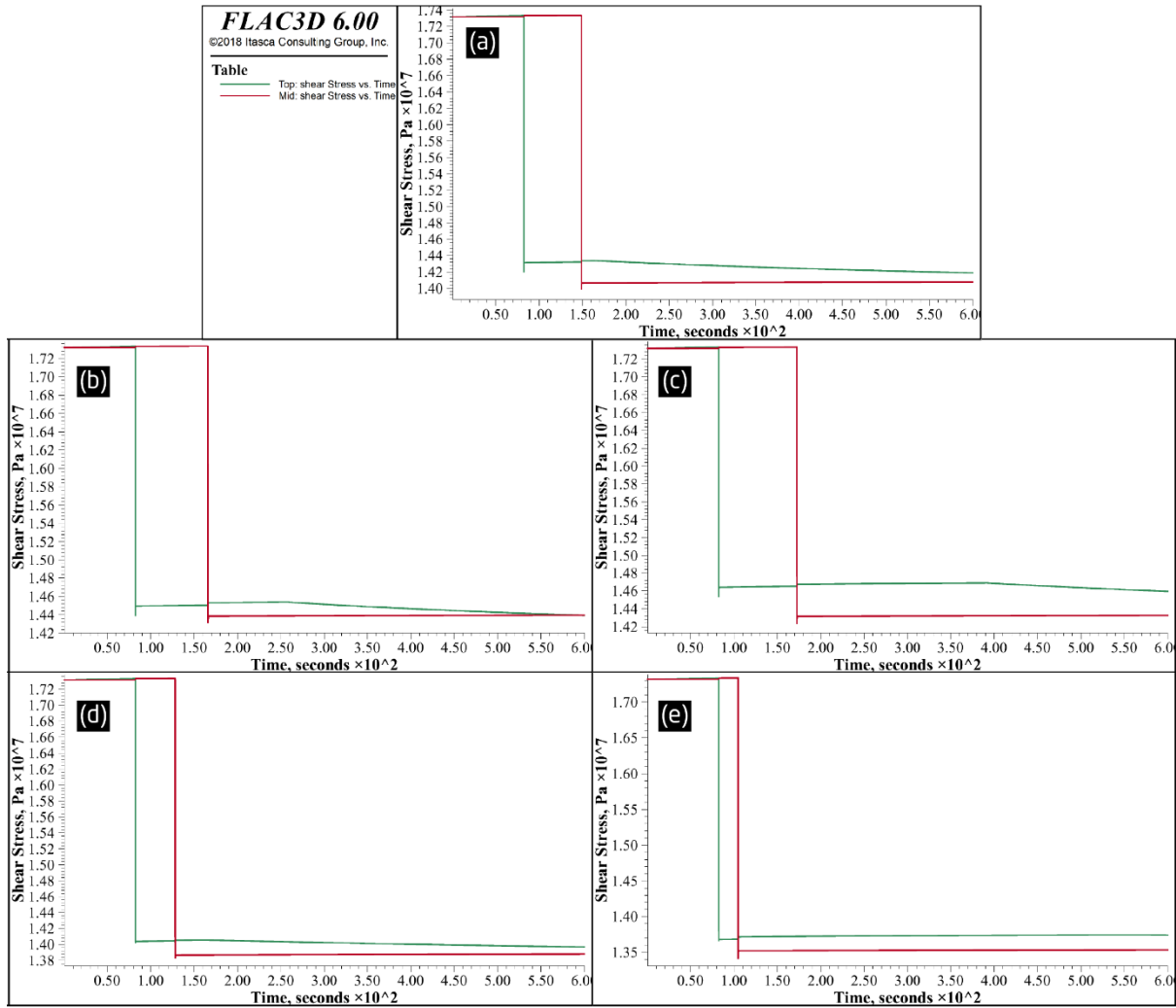


Figure-6. 9: Shear stress vs. time at two points along the fault (top and middle) for different $(a-b)$ values (a) $a-b=0$, (b) $a-b=+0.005$, (c) $a-b=+0.01$, (d) $a-b=-0.005$, & (e) $a-b=-0.01$.

6.3.5 Characteristic Slip Distance

In the previous set of simulations, characteristic slip distance was assumed constant and equals to $2e-5$ m. The first nucleation zone ruptures due to overpressure of 0.15 MPa at the fault trace. Changing this value changes how friction coefficient drops with shear displacement from the start of injection, therefore, characteristic slip distance has a crucial effect in determining the onset of failure. Under the same injection parameters and by implementing velocity neutral regime, friction coefficient drops faster to its dynamic value over smaller characteristic slip distance, and hence, co-seismic slip can occur earlier with smaller overpressure. For instance, for $L_C = 6 * 10^{-6}m$, first nucleation zone ruptures after only 28 seconds. Table-6.4 shows the simulation results for six different values of L_C .

| Characteristic slip distance L_C | Max. slip magnitude, mm | Slip rate, m/s | Time of rupture | Overpressure at injector, MPa |
|------------------------------------|-------------------------|----------------|-----------------|-------------------------------|
| 4e-7 | 0.5 | 2.15e-4 | 2 | 1.30 |
| 6e-6 | 0.5 | 1.72e-5 | 28 | 3.75 |
| 2e-5 | 0.49 | 5.45e-6 | 82 | 4.70 |
| 2e-4 | 0.48 | 2.12e-6 | 220 | 5.50 |
| 1e-3 | 0.037 | 6.27e-8 | 250 | 5.60 |
| 1e-2 | 0.024 | 3.90e-8 | 260 | 5.58 |

Table-6. 4: Sensitivity analysis of different characteristic slip distances L_C

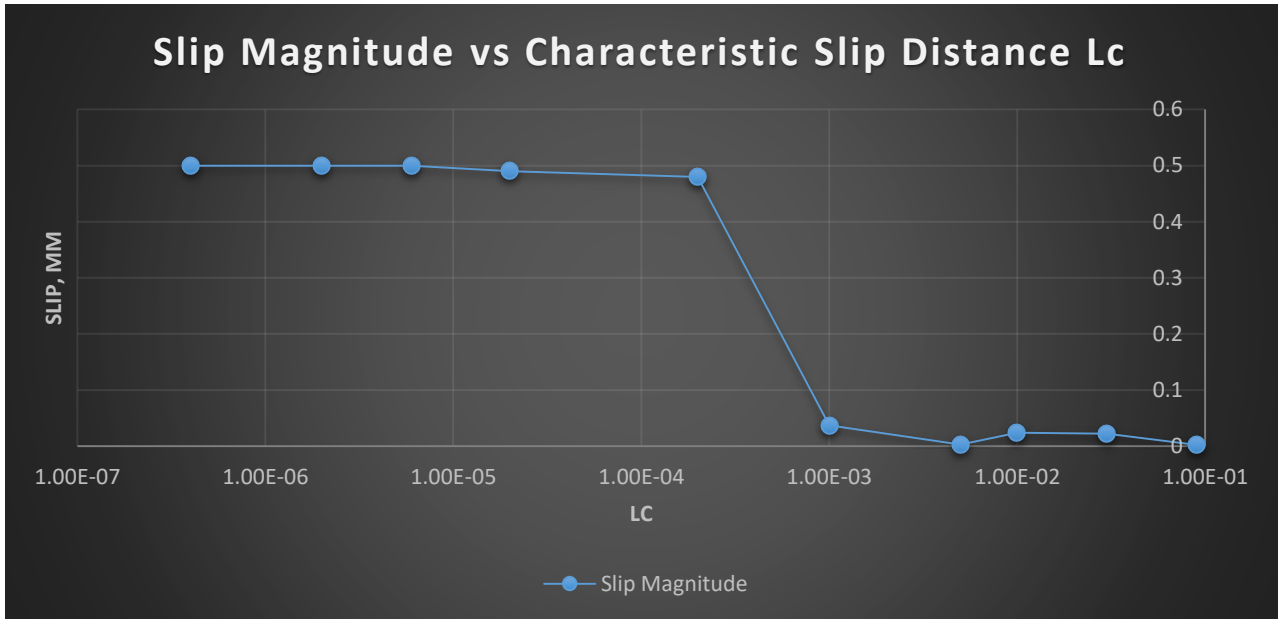


Figure-6. 10: Shear slip magnitudes vs different values of Lc (Each dot represents a simulation run).

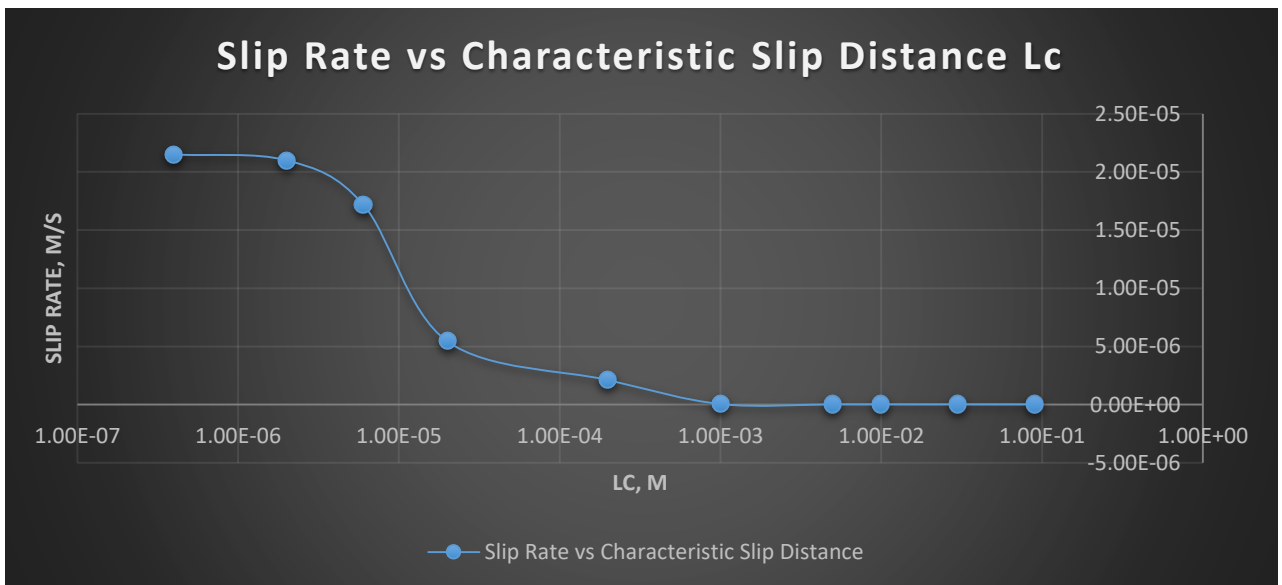


Figure-6. 11: Slip rate magnitudes vs different values of Lc (Each dot represents a simulation run).

From **Figure-6.10**, shear slip magnitudes are found to drop dramatically as the characteristic slip distance increased from tens of micrometers to millimeters. This observation agrees with recent numerical analysis of this parameter by Urpi et al. (2016). Slip rate is found to drop in less steep way with characteristic slip distance value in **Figure-6.11**.

CHAPTER 7: Conclusions and Discussion

During the last decade, number of injection-induced earthquakes has increased dramatically, leading to social unrest in the populated areas near the injection activities. Many efforts have been made to understand underground processes leading to induced seismicity in order to control and mitigate it during thermal energy extraction. Two models were proposed in this thesis to study the seismicity induced by fluid injection at both scales, scale of a reservoir and scale of a decametric single fault. Sensitivities and parametric analyses on various parameters related to operating and geologic conditions were performed and the following conclusions are drawn:

- Fractures orientation and density plays a critical role in determination of the very onset of seismicity and the evolution of the seismic cloud. Favorable oriented fractures result in dense seismic cloud and earlier occurrence of the seismic events.
- Permeability enhancement is modelled through equivalent continuum permeability value for both fractures and matrix. Both reversible (tensile aperture change) and irreversible (shear dilation of the fractures) are modelled.
- Increasing injection rate increases pore pressure along fractures and faults, hence results in earlier failure along the existing favorably oriented faults and fractures, and larger number of slipping fractures and faults. These results are consistent with field observations from a number of geothermal fields. Furthermore, shear displacement magnitude and, in turn, the resulting earthquake magnitudes are found to increase with injection rate.
- Given the low permeability of most geothermal reservoirs and the low thermal diffusivity of rocks, thermal stresses might contribute to seismic events only in the long-term operation, months to years, where the thermal front lags behind the hydraulic one. I also found that the hydraulic front is the major player that controls the location and number the triggered seismic events in both short- and long-term. These results agree with previous models in the technical literature.
- In accordance with numerical studies and field observations documented in the literature, differential stress acting on the fault and fractures in the reservoir determine the initial criticality status of these fractures. Increasing differential stress brings the favorably oriented fractures closer to failure envelope and facilitate failure by smaller pore pressure perturbation.
- Intermediate principal stress is found to have little or no significant effect on the fractures behavior during injection operation. This observation is also noticed in some lab experiments on pre-existing fractures in technical publications.
- Cyclic injection using high injection rates can result in higher number of events at further distances from the injection point compared to continuous injection for the same injected volume. This observation is in agreement with other proposed models to study

injection-induced seismicity in naturally fractured reservoirs. However, through prior knowledge of seismicity onset, injection-induced seismicity can be prevented by setting constraints on the injection pressure.

- Precise characterization of reservoir rocks is crucial for accurate modelling of fractures behavior in response to pore-pressure increase and stress field perturbation. Lower values of rock Poisson's ratio lead to a poroelastic stress path resulting in fractures stabilization during injection while initiates failure during production. In contrast to higher values of Poisson's ratio which result in an opposite behavior. Moreover, frictional parameters of the existing faults and fractures (e.g., static and dynamic frictional coefficient, characteristic slip distance) determine how frictional resistance of the fault evolves and help in deeper understanding of their response to pore pressure increase.
- By implementing the theory of rate-and-state to account for the frictional behavior of the fault in response to pore pressure increase, parametric analyses were performed to study velocity-neutral, velocity-strengthening and velocity-weakening scenarios. Velocity-weakening scenario is found to produce the largest drop in shear stress at the moment of rupture and highest slip-rate, shear slip, and event magnitudes. While velocity-strengthening scenario result in the lowest shear stress drop and lowest slip-rate, slip magnitudes and hence lowest seismic event magnitudes. The slipping area in the three scenarios almost remained the same.
- Slip rate is found to increase along the rupture-neighboring zones at the moment of rupture. This can be explained as the result of shear stress transfer to these zones after rupture. This observation is also found in laboratory experiments and numerical studies in the literature.
- Under the same loading conditions (same injection rate), it is noticed that the time at which the first nucleation zone (at the top of the fault) ruptures is the same for different frictional scenarios examined, and depends on: (1) the evolution to the pore pressure perturbation magnitude defined by Mohr-Coulomb criterion (2) cohesion and static frictional coefficient of the fault, and (3) the characteristic slip distance. However, by monitoring different location along the fault (top and middle of the fault), timing of the successive ruptures differs with different frictional scenarios. Successive ruptures along the fault plane occur faster in case of velocity-weakening than velocity-neutral or velocity-strengthening. This behavior is due to larger stress transfer to the neighboring zones, and larger drop in friction coefficient in velocity-weakening scenario.
- Characteristic slip distance L_C plays a critical role in determining the moment of rupture along the fault as the friction coefficient drops from its static to dynamic value linearly with characteristic slip value. Higher values of this parameter result in delayed rupture with limited slip rates & slip magnitudes compared to smaller L_C values, for the same injection rate and loading conditions.

As noticed in my simulations on the fault scale, slip rate increases with injection rate and fluid pressure increase along the fault zone. However, the nucleation area within the pressurized zone may be smaller than the critical nucleation zone for an earthquake, so aseismic creep is expected. This creep may result in shear stress transfer and earthquake nucleation in the neighboring zones along the fault. In this case, an earthquake can be expected beyond the pressure transient front made by fluid injection and/or production. Deeper understanding of the relation of pore pressure change with seismic slip vs aseismic creep is crucial to control seismicity during fluid injection and/or production operations, and slip rate changes along faults and joints in the reservoir can be used as indicator of potential future seismic events.

Future development of my work includes calibrating my first model with field data from Basel geothermal field (Switzerland) to reproduce the past seismicity and to explore the forecasting capability of the model to investigate different scenarios aiming to control the induced seismicity during operating geothermal reservoir.

References

- 1) Alejano L. and Bobet A. "Drucker–Prager criterion". *Rock Mechanics Rock Engineering* (2012): 1–5.
- 2) Allmann B. P. and Shearer P. M. "Spatial and temporal stress drop variations in small earthquakes near Parkfield, California". *Journal Geophysical Research* (2007); 112:B04305.
- 3) Anderson J., Wesnousky S., Stirling M. "Earthquake Size as a Function of Fault Slip Rate". *Seismological Society of America*. Vol. 86 No.3 pp 684-690 June 1996
- 4) Bachmann C. E., Wiemer S., Woessner J., and Hainzl S., Statistical analysis of the induced Basel 2006 earthquake sequence: introducing a probability-based monitoring approach for Enhanced Geothermal Systems, *Geophysical Journal International*, 186 (2) - (2011)
- 5) Bagheri M. and Settari A. "Modeling of geomechanics in naturally fractured reservoirs". *SPE Reservoir Evaluation Engineering* 2008; 11:108–18.
- 6) Baisch S., R. Voros, E. Rothert, H. Stang, R. Jung, and R. Schellschmidt. "A numerical model for fluid injection induced seismicity at Soultz-sous-Forets". *International Journal of Rock Mechanics and Mining Sciences*, 47 (3), 405 (2010).
- 7) Bandis S.C., Lumsden A.C., Barton N.R. "Fundamentals of rock joint deformation". *Int. J. Rock Mechanics and Mining Science* 20, 249 (1983).
- 8) Barton N., Bandis S. and Bakhtar K. "Strength, deformation and conductivity coupling of rock joints". *International Journal of Rock Mechanics and Mining Science* (1985) ;22:121–40.
- 9) BC Oil and Gas Commission ,“Investigation of observed seismicity in the Horn River Basin” (BC Oil and Gas Commission, Victoria, British Columbia, Canada, 2012); www.bcogc.ca/node/8046/download?documentID=1270.
- 10) Bear, J., Tsang, C.F., Marsily, G.D. "Flow and Contaminant Transport in Fractured Rock". Academic Press Inc., San Diego, CA, USA (1993).
- 11) Benz T. and Schwab R. "A quantitative comparison of six rock failure criteria". *International Journal of Rock Mechanics and Mining Sciences* (2008); 45:1176–86.
- 12) Bodvarsson G, Lowell RP. "Ocean floor heat flow and the circulation of interstitial waters". *Journal of Geophysical Research* 1972; 77:4472.5.
- 13) Bodvarsson G. "Thermoelastic phenomena in geothermal systems". *Proceedings of the second UN symposium on the development and use of geothermal resources*, San Francisco, CA; 1976. p. 903.7.
- 14) Bommer JJ, Oates S, Cepeda JM, Lindholm C, Bird J, Torres R, et al. "Control of hazard due to seismicity induced by a hot fractured rock geothermal project". *Engineering Geology* (2006); 83:287–306.
- 15) Brodsky E. and Lajoie L. "Anthropogenic seismicity rates and operational parameters at the Salton Sea Geothermal Field". *Science* (2013).
- 16) Bruel D. "Impact of induced thermal stresses during circulation tests in an engineered fractured geothermal reservoir; example of the Soultz-sous-Forets European Hot Fractured rock Geothermal Project, Rhine Graben, France". *Oil and Gas Science and Technology Revue IFP* 2002; 57:459.70.

- 17) Bruhn D., Huenniges E., Agustsson K., Zang A., Rachez X., Wiemer S., van Wees J. D. and Calcagno P., "Summary of the European GEISER Project (Geothermal Engineering Integrating Mitigation of Induced Seismicity in Reservoirs)". Proceedings World Geothermal Congress (2015) Melbourne, Australia, 19-25 April.
- 18) Bulletin of the seismological society of America, 65(5), 1073-1095, 1975.
- 19) Byerlee J. "Friction of rocks". Pure and Applied Geophysics (1978); 116:615–26.
- 20) Charléty J., Cuenot N., Dorbath L., Dorbath C., Haessler H. and Frogneux M. "Large earthquakes during hydraulic stimulations at the geothermal site of Soultz-sous-Forêts". International Journal of Rock Mechanics Mining Sciences (2007); 44:1091–105.
- 21) Chun K. Fracture Propagation Under Poro-Thermally Induced Stress Using The Displacement Discontinuity Method. Proceedings Of Thirty-Eighth Workshop On Geothermal Reservoir Engineering Stanford University, Stanford, California, February 11-13, 2013
- 22) Clarke H., Eisner L., Styles P. and Turner P. "Felt seismicity associated with shale gas hydraulic fracturing: the first documented example in Europe". Geophysical. Research Letters (2014); 41:8308–14
- 23) Cloetingh S., van Wees J., Ziegler P., Lenkey L., Beekman F., Tesauro M. et al. "Lithosphere tectonics and thermo-mechanical properties: an integrated modelling approach for Enhanced Geothermal Systems exploration in Europe". Earth-Sciences Reviews (2010); 102:159–206.
- 24) Clotworthy A. "Response of Wairakei geothermal reservoir to 40 years of production". Proceedings World Geothermal Congress Kyushu-Tohoku, Japan, May 28 - June 10, 2000
- 25) Cooper H. and Simmons G. "The effect of cracks on the thermal expansion of rocks," Earth and Planetary Science Letters, vol. 360, no. 3, pp. 404–412, 1977.
- 26) Da Fontoura S. "Lade and modified Lade 3D rock strength criteria". Rock Mechanics and Rock Engineering (2012): 1–6.
- 27) Davies R., Foulger G., Bindley A. and Styles P. "Induced seismicity and hydraulic fracturing for the recovery of hydrocarbons". Marine and Petroleum Geology 45 (2013) 171e185.
- 28) Davis S. D. and Pennington W. D. "Induced seismic deformation in the Cogdell oil field of west Texas". Bulletin of the Seismological Society of America (1989). 79:1477–95
- 29) Dershowitz W. S. and Einstein H. H. "Characterizing rock joint geometry with joint system models". Rock Mechanics and Rock Engineering (1988); 21:21–51.
- 30) Dieterich J. "A constitutive law for rate of earthquake production and its application to earthquake clustering". Journal Geophysical Research (1994); 99:2601–18.
- 31) Dieterich J. "Modeling of rock friction 1. Experimental results and constitutive equations". Journal Geophysical Research (1979); 84:2161–8.
- 32) Dieterich J., Richards-Dinger K., and Kroll K. "Modeling Injection-Induced Seismicity with the Physics-Based Earthquake Simulator RSQSim". Seismological Research Letters (2015).
- 33) Dinske C. and Shapiro S. "Seismotectonic state of reservoirs inferred from magnitude distributions of fluid-induced seismicity". Journal of Seismology (2013); 17:13–25.
- 34) Douglas J. and Jousset P. "Modeling the difference in ground-motion magnitude-scaling in small land large earthquakes". Seismological Research Letters (2011); 82:504–8.
- 35) Eberhardt E. "The Hoek–Brown failure criterion". Rock Mechanics and Rock Engineering (2012): 1–8.
- 36) Ellsworth W. "Injection-induced earthquakes". Science (2013); 341:1225942

- 37) Elsworth D. "Thermal permeability enhancement of blocky rocks: one-dimensional flows". *International Journal of Rock Mechanics and Mining Science* 1989; 26(3/4):329-39.
- 38) Enayatpour S. & Patzek T. Thermal Shock in Reservoir Rock Enhances the Hydraulic Fracturing of Gas Shales. Unconventional Resources Technology Conference held in Denver, Colorado, USA, 12-14 August 2013.
- 39) Engelder, J. T., & Fischer, M. P. "Influence of poroelastic behaviour on the magnitude of minimum horizontal stress, S_h , in overpressured parts of sedimentary basins". *Geology*, 22(10), 949-952. (1994).
- 40) Eppelbaum L. Kutasov I. & Pilchin V. Lecture Notes in Earth System Sciences, Applied Geothermics. Springer-Verlag Berlin Heidelberg 2014
- 41) Evans K., Zappone A., Kraft T., Deichmann N. and Moia F. "A survey of the induced seismic responses to fluid injection in geothermal and CO₂ reservoirs in Europe". *Geothermics* (2012); 41:30–54.
- 42) Fredrich J. and Wong T. "Mechanics of thermally induced cracking in three crustal rocks". *Journal of Geophysical Research* 1986; 91(B12):12743-54.
- 43) Frohlich C, Walter J. and Gale J. "Analysis of transportable array (USArray) data shows earthquakes are scarce near injection wells in the Williston Basin, 2008–2011". *Seismological Research Letters* (2015); 86:492–99.
- 44) Frohlich C. "Two-year survey comparing earthquake activity and injection-well locations in the Barnett Shale, Texas". *Proceedings of National Academy of Science U.S.A.*(2012); 109 13934–13938.
- 45) Gaite B., Ugalde A. and Villaseñor A., Blanch E. "Improving the location of induced earthquakes associated with an underground gas storage in the Gulf of Valencia (Spain)". *Physics of the Earth and Planetary Interiors* (2016) 254:46–59
- 46) Gaucher E., Schoenball M., Heidbach O., Zang A., Fokker P., Van Wees J. and Kohl T. "Induced Seismicity in Geothermal Reservoirs: Physical Processes and Key Parameters". (2015)
- 47) GEA Geothermal Energy Association, '2016 Annual U.S. & Global Geothermal Power Production Report', March 2016.
- 48) Gens A., Vaunat J., Garitte B. and Willeveau Y. "In situ behavior of a stiff layered clay subject to thermal loading: observations and interpretation". *Geotechnique* (2007); 57:207–28.
- 49) Germanovich LN, Chanpura RA, Ring LM, Filippov AG. "Poroelastic mechanism of fault reactivation as a result of reservoir depletion". In: *Proceedings of the Biot conference on poromechanics*, 1998. p. 415-20.
- 50) Ghassemi A, Tarasovs S, Cheng A. "An integral equation method for modeling three-dimensional heat extraction from a fracture in hot dry rock". *International Journal of Numerical and Analytical Methods in Geomechanics* 2003; 27:989-1004.
- 51) Ghassemi A., Tarasovs S., Cheng A., "A 3-D study of the effects of thermomechanical loads on fracture slip in enhanced geothermal reservoirs". *International Journal of Rock Mechanics and Mining Sciences*, Vol. 44(8), 2007, pp. 1132-1148.
- 52) Gobel T. "A comparison of seismicity rates and fluid-injection operations in Oklahoma and California: implications for crustal stresses". *Lead. Edge* (2015) 34:640–48
- 53) Goertz-Allmann B., Goertz A. and Wiemer S. "Stress drop variations of induced earthquakes at the Basel geothermal site". *Geophysical Research Letters* (2011): 38.
- 54) Gor G. and Prévost J. Effect of CO₂ injection temperature on caprock stability. *Energy Procedia* 37 (2013) 3727 – 3732
- 55) Grasso J. Mechanics of seismic instabilities induced by the recovery of hydrocarbons. *Pure and applied geophysics*. September 1992, Volume 139, Issue 3–4, pp 507–534

- 56) Gutenberg B. and Richter C. "Earthquake magnitude, intensity, energy, and acceleration: (Second paper)". *Bulletin of Seismological Society of America* (1956); 46:105–45.
- 57) Hackston A. J. "Activation of Faulting Under Controlled Stress Conditions". PhD Thesis (2013)
- 58) Hagoort J, Weatherill BD, Settari A. "Modeling the propagation of water flood-induced hydraulic fractures". *SPE J* 1980; 8:293.303.
- 59) Haimson B. and Bobet A. "Introduction to suggested methods for failure criteria". *Rock Mechanics and Rock Engineering* (2012): 1–2.
- 60) Hainzl S., and Ogata Y. "Detecting uid signals in seismicity data through statistical earthquake modeling". *Journal of Geophysical Research*, 110 (2005).
- 61) Häring, M., Schanz, U., Ladner, F. and Dyer, B. "Characterization of the Basel 1 enhanced geothermal system". *Geothermics* (2008) 37, 469e495
- 62) Harris R. A., Barall M., Archuleta R., Dunham E., Aagaard B., Ampuero J. P., Bhat H., Cruz-Atienza V., Dalguer L., Dawson P., Day S., Duan B., Ely G., Kaneko Y., Kase Y., Lapusta N., Liu Y., Ma S., Oglesby D., Olsen K., Pitarka A., Song S., Templeton E. "The SCEC/USGS Dynamic Earthquake Rupture Code Verification Exercise". *Seismological Research Letters* 80(1), 119–26 (2009).
- 63) Healy J., Rubey W., Griggs D. and Raleigh C. "The Denver earthquakes". *Science* (1968) 161:1301–10
- 64) Hirschberg S., Wiemer S., Burgherr P. (eds.) 'Energy from the Earth Deep Geothermal as a Resource for the Future?' 2015, P.14
- 65) Holland A. "Earthquakes triggered by hydraulic fracturing in south-central Oklahoma". *Bulletin Seismological Society America* (2013a) 103:1784–92
- 66) Hornbach M., Jones M., Scales M., DeShon H., Magnani M., et al. "Ellenburger wastewater injection and seismicity in North Texas". *Physics of Earth Planet and Interior* (2016) 261:54–68
- 67) Itasca. FLAC3D, Fast Lagrangian Analysis of Continua in 3 Dimensions Documentations. Minneapolis, Minnesota: Itasca Consulting Group.
- 68) Izadi G. "Evolution of Permeability and Induced Seismicity within Fractured Reservoirs". PhD Dissertation. Energy and Mineral Engineering. The Pennsylvania State University (2012).
- 69) Izadi, G., & Elsworth, D. "Evolution of induced seismicity due to interactions between thermal, hydraulic, mechanical and chemical processes in EGS reservoirs". In 46th US Rock Mechanics / Geomechanics Symposium (2012) (Vol. 3, pp. 2107-2113)
- 70) Jaeger J., Cook N. and Zimmermann R. "Fundamentals of rock mechanics. 4th edition". Oxford: Black well publishing (2007).
- 71) Jeanne, P., Rutqvist, J., Rinaldi, A. P., Hutchings, L., Singh, A., & Dobson, P. F. "Mechanisms of EGS Creation at The Geysers (California) revealed by Seismic Tomography, Spatiotemporal Evolution of the Microseismic Events and Geomechanical Simulations". American Rock Mechanics Association. (2015).
- 72) Jing L., "A review of techniques, advances and outstanding issues in numerical modelling for rock mechanics and rock engineering". *International Journal of Rock Mechanics and Mining Sciences*. (2003)
- 73) Jones L. and Helmberger D. "Seismicity and stress-drop in the Eastern Transverse Ranges, southern California". *Geophysical Research Letters* (1996); 23:233–6.
- 74) Kanamori, H. and Anderson, D., Theoretical basis of some empirical relations in seismology"
- 75) Keranen K. and Weingarten M." Induced Seismicity". *Annual Review of Earth and Planetary Sciences* (2018). 46:149–74.

- 76) Keranen K., Savage H., Abers G. and Cochran E. "Potentially induced earthquakes in Oklahoma, USA: links between wastewater injection and the 2011 Mw 5.7 earthquake sequence". *Geology* (2013); 41:699–702
- 77) Keranen, K., Weingarten M., Abers G., Bekins B., and Ge S. "Sharp increase in central Oklahoma seismicity since 2008 induced by massive wastewater injection", *Science* (2014) 345, no. 6195, 448–451,
- 78) Kim W. "Induced seismicity associated with fluid injection into a deep well in Youngstown, Ohio". *Journal of Geophysical Research* (2013) 10.1002/jgrb.50247.
- 79) Kohl T, Evans KF, Hopkirk RJ, Ryback L. "Coupled hydraulic, thermal, and mechanical considerations for the simulation of hot dry rock reservoirs". *Geothermics* 1995; 24:345.59.
- 80) Kohl, T. & Megel, T. "Predictive modeling of reservoir response to hydraulic stimulation at the European EGS site Soultz-sous-Forêts," *International Journal of Rock Mechanics & Mining Science* (2007), 44, 118–131.
- 81) Kämpel, H. "Poroelasticity: Parameters Reviewed", *Geophys. Journal* 1991; In.105, 783–799.
- 82) Kurashige M. "A thermoelastic theory of fluid-filled porous materials". *International Journal of Solids and Structures* (1989); 25:1039–52.
- 83) Kwiatek G., Bohnhoff, M., Dresen, G., Schulze, A., Schulte, T., Zimmermann, G., and Huenges, E. "Microseismicity Induced During Fluid-Injection: A Case Study from the Geothermal Site at Groß Schönebeck, North German Basin" *Acta Geophysica*, 58, (2010), 995-1020
- 84) Lambert C. "Structural controls on fluid migration and seismic variability in northern Oklahoma". Master's Thesis, Dep. Earth Atmospheric Science (2017), Cornell Univ., Ithaca, NY
- 85) Leonard M. "Earthquake fault scaling: self-consistent relating of rupture length, width, average displacement, and moment release". *Bulletin of Seismological Society of America* (2010); 100:1971–88.
- 86) Lister DRB. On the thermal balance of a mid-ocean ridge. *Royal Society Geophysics Journal* 1972; 26:515.35.
- 87) Lowell RP. Thermoelasticity and the formation of black smokers. *Geophysical Research Letters* 1990; 17:709.12.
- 88) Maillot B., Nielsen S., and Main I. Numerical simulation of seismicity due to fluid injection in a brittle poroelastic medium. *Geophysical Journal International*, Volume 139, Issue 2, 1 November 1999, Pages 263–272.
- 89) Majer E., Baria R., Stark M., Oates S., Bommer J., Smith B., and Asanuma H. "Induced Seismicity Associated with Enhanced Geothermal Systems" *Geothermics*, 185-222.
- 90) Manga M., Wang C. and Shirzaei M. "Increased stream discharge after the 3 September 2016 Mw 5.8 Pawnee, Oklahoma earthquake". *Geophysical Research Letters* (2016); 43:11588–94
- 91) Maxwell S. "Unintentional Seismicity Induced by Hydraulic Fracturing". Article. *CSEG RECORDER* OCTOBER (2013).
- 92) McClure, M., and Horne R. "Investigation of injection-induced seismicity using a coupled fluid flow and rate / state friction model" *Geophysics*, 76 (6), (2012).
- 93) McGarr A. "Maximum magnitude earthquakes induced by fluid injection". *Journal of Geophysical Research* (2013). 119, no. 2, 1008–1019.
- 94) McGarr A., Simpson D. and Seeber L., "Case histories of induced and triggered seismicity," *International Handbook of Earthquake and Engineering Seismology* (2002); (Academic Press, Waltham, MA), vol. 8, chap. 40.

- 95) Megel T, Kohl T, Rose P. "Reservoir modeling for stimulation planning at the Coso EGS project". Geothermal Research Council Trans (2005) ;29:173.6.
- 96) Monterrosa M. and Axelsson G. RESERVOIR RESPONSE MONITORING DURING PRODUCTION Presented at "Short Course V on Conceptual Modelling of Geothermal Systems", organized by UNU-GTP and LaGeo, in Santa Tecla, El Salvador, February 24 - March 2, 2013.
- 97) Mossop, A., Segall, P., "Subsidence at The Geysers geothermal field, N., 1997. California from a comparison of GPS and leveling surveys". Geophys. Res. Lett. 24, 1839–1842.
- 98) Nersesian, Roy L. "Energy for the 21st Century: A Comprehensive Guide to Conventional and Alternative Sources". 2nd ed. M.E. Sharpe, Inc., 2010.
- 99) Nicholson C. and Wesson R. "Earthquake hazard associated with deep well injection: A report to the U.S. Environmental Protection Agency" U.S. Geological Survey Bulletin (1951); <http://pubs.usgs.gov/bul/1951/report.pdf>.
- 100) Norbeck J. and Horne R. "Maximum magnitude of injection-induced earthquakes: A criterion to assess the influence of pressure migration along faults". Tectonophysics (2018).
- 101) Nowacki W. "Thermoelasticity". New York: Pergamon Press; 1973.
- 102) Nowacki W. "Thermoelasticity". Second edition Oxford (1986).
- 103) Nygren A, Ghassemi A, Cheng A. "Effects of cold-water injection on fracture aperture and injection pressure". Geothermal Resources Council Trans 2005; 29:183.7.
- 104) Nygren A, Ghassemi A. "Coupled poroelastic and thermoelastic effects of injection into a geothermal reservoir". In: Proceedings of the 40th US rock mechanics symposium, Golden, CO, 2006. 30
- 105) Nygren A, Ghassemi A. "Influence of cold water injection on critically stressed fractures in Coso geothermal field, CA". In: Proceedings of the 39th US rock mechanics symposium, Anchorage, Alaska, 2005.
- 106) Ogata Y. "Seismicity analysis through point-process modeling: a review". Pure and Applied Geophysics (1999); 155:471–507.
- 107) Orzol, J., Jung, R., Jatho, R., Tischner, T., and Kehrer, P. "The Genesys-Project: Extraction of Geothermal Heat from Tight Sediments". World Geothermal Congress (2005).
- 108) Óskarsson F., Fridriksson T. and Thorbjörnsson D. Geochemical Monitoring of the Reykjanes Geothermal Reservoir 2003 to 2013. Proceedings World Geothermal Congress 2015 Melbourne, Australia, 19-25 April 2015
- 109) Perkins T. and Gonzalez J. "The Effect of Thermoelastic Stresses on Injection Well Fracturing". Society of Petroleum Engineers (1985)
- 110) Popov Y., Bayuk I., Parshin A., Miklashevskiy D., Novikov S., and Chekhonin E. NEW METHODS AND INSTRUMENTS FOR DETERMINATION OF RESERVOIR THERMAL PROPERTIES. Proceedings, 37th Workshop on Geothermal Reservoir Engineering Stanford University, Stanford, California, January 30 - February 1, 2012.
- 111) Pratt W. and Johnson D. "Local subsidence of the Goose Creek oil field". Journal of Geology (1926). 34:577–90
- 112) Priest S. "Three-dimensional failure criteria based on the Hoek–Brown criterion". Rock Mechanics and Rock Engineering (2012): 1–5
- 113) Raleigh C. B., Healy J. and Bredehoeft J. "An experiment in earthquake control at Rangely, Colorado". Science (1976); 191, 1230–1237.
- 114) Rothert E. and Shapiro S. "Microseismic monitoring of borehole fluid injections: data modeling and inversion for hydraulic properties of rocks". Geophysics (2003); 68:685–9.

- 115) Rubinstein J. and Mahani A. "Myths and Facts on Waste Water Injection, Hydraulic Fracturing, Enhanced Oil Recovery, and Induced Seismicity". *Seismological Research Letters* (2015).
- 116) Rubinstein, J., Ellsworth W. McGarr A. and Benz H. "The 2001-present induced earthquake sequence in the Raton Basin of northern New Mexico and southern Colorado" *Bulletin of Seismological Society of America* (2014) 104, no.5, 2162–2181.
- 117) Ruina A. "Slip instability and state variable friction laws". *Journal of Geophysical Research* (1983); 88:10359–70.
- 118) Rutqvist J. "Status of the TOUGH-FLAC simulator and recent applications related to coupled fluid flow and crustal deformations". *Computational Geosciences* (2011); 37:739–50.
- 119) Rutqvist J. and Stephansson O. "The role of hydromechanical coupling in fractured rock engineering". *Hydrogeological Journal* (2003); 11:7–40.
- 120) Rutqvist, J., & Oldenburg, C. M. "Analysis of Injection-Induced Micro-Earthquakes in a Geothermal Steam Reservoir, The Geysers Geothermal Field, California". *American Rock Mechanics Association*. (2008).
- 121) Safari R. & Ghassemi A. "Three-dimensional poroelastic modeling of injection induced permeability enhancement and microseismicity". *United Kingdom* (2016).
- 122) Safari, R., & Ghassemi, A. "3D Analysis of Thermo-poroelastic Processes on Fracture Network Deformation and Induced Micro-Seismicity Potential in EGS". *American Rock Mechanics Association*. June 26 (2016)
- 123) Scholz C. "Earthquakes and friction laws". *Nature* (1998); 391:37–42.
- 124) Schultz R, Corlett H, Haug K, Kocon K, MacCormack K, et al. "Linking fossil reefs with earthquakes: geologic insight to where induced seismicity occurs in Alberta". *Geophysical Research Letters* (2016); 43:2534–42.
- 125) Seeber L. Armbruster J. and Kim W. "A fluid-injection-triggered earthquake sequence in Ashtabula, Ohio: implications for seismogenesis in stable continental regions". *Bulletin of Seismological Society of America* (2004) 94:76–87
- 126) Segall P and Fitzgerald S. "A note on induced stress changes in hydrocarbon and geothermal reservoirs" *Tectonophysics* 289 (1998) 117–128
- 127) Segall P. "Earthquakes Triggered by Fluid extraction". *Geology* 1989; 17:942.6.
- 128) Segall P., Grasso J., and Mossop A. "Poroelastic stressing and induced seismicity near the Lacq gas field, southwestern France". 10 August 1994
- 129) Shapiro S., Dinske C., Kummerow J. "Probability of a given-magnitude earthquake induced by a fluid injection". *Geophysical Research Letters* (2007)
- 130) Shapiro, S. A., C. Dinske, and E. Rothert. Hydraulic-fracturing controlled dynamics of microseismic clouds, *Geophys. Res. Lett.*, 33, L14312, doi:10.1029/2006GL026365. (2006b).
- 131) Sherburn S., Bromley C., Bannister S., Sewell S., Bourguignon S. "New Zealand Geothermal Induced Seismicity: an overview" *Proceedings World Geothermal Congress*. Melbourne, Australia, 19-25 April 2015
- 132) Stark M. "Imaging injected water in the Geysers reservoir using microearthquakes data". *Geothermal Resources Council Trans* 1990; 1697.704.
- 133) Stephens G, Voight B. Hydraulic fracturing theory for conditions of thermal stress". *International Journal of Rock Mechanics and Mining Science* 1982; 19:279.84.
- 134) Stewart F. and Ingelson A. "Regulating energy innovation: US responses to hydraulic fracturing, wastewater injection and induced seismicity". *Journal of Energy and Natural Resources Law* (2017); 35:109–46

- 135) Taron J., and Elsworth D. Coupled Mechanical and Chemical Processes in Engineered Geothermal Reservoirs with Dynamic Permeability. *International Journal of Rock Mechanics & Mining Sciences* 47 (2010) 1339–1348
- 136) The Australian Geothermal Reporting Code Committee. *The Geothermal Reporting Code, Second Edition*. 2010.
- 137) Theis, C. V. "The Relation between the Lowering of the Piezometric Surface and the Rate and Duration of Discharge of a Well Using Groundwater Storage," *Trans. Am. Geophys. Union*, 10, 519-524 (1935).
- 138) Tsang C. "Coupled hydromechanical-thermochemical processes in rock fractures". *Reviews of Geophysics* (1991); 29:537–51.
- 139) Urpi, L., Rinaldi AP., Rutqvist J., Cappa F., Spiers CJ. "Dynamic simulation of CO₂-injection-induced fault rupture with slip-rate dependent friction coefficient". (2016)
- 140) US Department of Energy, Office of Oil and Natural Gas. "Induced Seismicity". (2016)
- 141) USGS Earthquake glossary website <https://earthquake.usgs.gov/learn/glossary/?term=magnitude> (Last access on April 8th 2019)
- 142) Utsu T. "A statistical study on the occurrence of aftershocks". *Geophysics Magazine* ;30:521–605. (1961)
- 143) Valoroso L., Improta L., Chiaraluce L., Di Stefano R., Ferranti L., et al. "Active faults and induced seismicity in the Val d'Agri area (Southern Apennines, Italy)". *Geophysical Journal International* (2009) 178:488–502
- 144) Van Wees JD., Fokker P., Thienen-Visser K., Wassing B., Osinga S., Orlic B., Ghouri S., Buijze L.. & Pluymaekers M.; "Geomechanical models for induced seismicity in the Netherlands: inferences from simplified analytical, finite element and rupture model approaches"; *Netherlands Journal of Geosciences* (2017)
- 145) Vernik L. and Zobak M. "Estimation of maximum horizontal principal stress magnitude from stress-induced well bore breakouts in the Cajon Pass Scientific Research borehole". *Journal of Geophysical Research* (1992).
- 146) Wang H. "Quasi-static poroelastic parameters in rock and their geophysical applications". *Pure and applied geophysics*, June 1993, Volume 141, Issue 2–4, pp 269–286.
- 147) Wassing B., van Wees J. and Fokker P. "Coupled continuum modeling of fracture reactivation and induced seismicity during enhanced geothermal operations". *Geothermics* (2014); 52:153–64.
- 148) Wiemer S., Giardini D, Fäh D, Deichmann N, Sellami S. "Probabilistic seismic hazard assessment of Switzerland: best estimates and uncertainties" .*Journal of Seismology*;13:449–78 (2009).
- 149) Willis-Richards J, Watanabe K, Takahashi H. "Progress toward a stochastic rock mechanics model of engineered geothermal systems". *Journal of Geophysical Research* (1996); 101:17481–96.
- 150) Witherspoon P., Wang J., Iwai K., Gale J. "Validity of Cubic Law for fluid flow in a deformable rock fracture". *Water Resources Research* (1980); 16:1016–24.
- 151) Wong T. and Brace W. "Thermal expansion of rocks: some measurements at high pressure," *Tectonophysics*, vol. 570, no. 2, pp. 95–117, 1979.
- 152) Yoon, J.-S., Zang, A., Stephansson, O.: Numerical investigation on optimized stimulation of intact and naturally fractured deep geothermal reservoirs using hydro-mechanical coupled discrete particles joints model. - *Geothermics*, 52, p. 165-184.(2014)
- 153) Zielke O. and Arrowsmith J. "Depth variation of coseismic stress drop explains bimodal earthquake magnitude–frequency distribution". *Geophysical Research Letters* (2008); 35: L24301.

- 154) Zoet A., Bowyer J., Bratkovich S., Frank M. and Fernholz K.: Geothermal 101: The Basics And Applications Of Geothermal Energy, 12 SEPTEMBER 2011.